REMARKS/ARGUMENTS

Reconsideration of this application is requested. Claims 167, 168 and 170-176 are active in the application subsequent to entry of this Amendment.

Discussion of Amendments to the Claims

In order to advance examination and address issues of claim clarity as raised in items 2 and 3 of the Official Action, the claims have been amended and recast directed to a silicon implant comprising a drug and a hydrophobic resorbable mesoporous silicon having the requisite pore size. The drug is located at least partially in the pores of the porous silicon. Claim 169 has been deleted in order to reduce issues and a consequential change with respect to change in claim type has been made in claim 173.

Response to Lack of Written Description and Claim Clarity Rejections

In item 2 of the Official Action the examiner questions basis in the original description for the term "hydrophobic" as it modifies "resorbable mesoporous silicon". Basis for this term may be found at page 23, lines 13-14 of the description. The examiner will note that this is the same information that was provided in the Amendment of August 4, 2005, page 4, fourth paragraph. Contrary to item 2 of the Official Action, basis does exist in the original description of the invention and therefore this rejection should be withdrawn.

Further responding, fabrication of hydrophobic porous silicon, by anodization of the silicon in 40% aqueous HF diluted with ethanol, is also described at page 28 lines 16 to 22 of the present application.

Hydrophobic porous silicon is not explicitly mentioned in this section of the application, however it can be seen from page 6 (second paragraph) and page 12 (fourth item in list) of the attached review article by Vinegoni et al, published in October 2000, that anodization in 40% aqueous HF, diluted with ethanol, results in the formation of hydrophobic porous silicon. The article can be found at: http://www.quantacomm.com/members/vinegoni/bookspage/review.pdf.

Therefore the specification shows how to make resorbable hydrophobic porous silicon, and how to combine it with a drug. It follows that the inventors had possession of the invention at the time of the priority date.

1030797

Response to Prior Art-Based Rejection

Previous claims 167-176 are rejected as being unpatentable over WO 97/06101 taken by itself or in combination with additional references (as discussed below). To the extent that the examiner's concerns extend to the amended claims presented above, the rejection is traversed.

In the Action, the Examiner highlights claim 173 of the present application, which specifies that the silicon erodes over an interval of between one month and two years. However, the skilled person would not have known this at the time of the priority date. It follows that wetting of the WO '101 porous silicon (page 13, lines 2 to 4) would have lead the skilled person away from the use of hydrophobic porous silicon for the delivery of a drug by erosion.

The Examiner highlights the absence of explicit reference in WO '101 to oxidation. However, the skilled person would know that storage of porous silicon in air generally results in oxidation. For example, US 5,561,304 (copy attached) describes ageing in air, which results in an oxidized silicon surface (column 4, lines 45 to 51).

The skilled person would know, from WO '101 page 4 lines 25 to 28, that oxidation is associated with hydrophilicity. This, in combination with account of air ageing (page 9, lines 13 to 17), would lead the skilled person away from the use of hydrophobic porous silicon.

The Examiner has cited as optional secondary references US 6,696,258 (US '258) and US 5,922,299 (US '299). US '258 mentions a hydrophobic alkyl chain (column 1, lines 66 to 67) and a hydrophobic amine (column 2, lines 18 to 19), both these extracts occurring in the background section of the patent. US '299 mentions a hydrophobic sol-gel film in the background section of the patent (column 2, lines 50 to 54).

It would not be obvious for the skilled person to combine WO '101 with US '258 or to combine WO '101 with US '299. This is because the WO '101 emphasis on air ageing and wetting would lead the skilled person away from the use of a hydrophobic material.

With regard to the secondary references, the Bruinsma et al patent is cited as prior art under 35 USC §102(e) as of its actual U.S. filing date of August 26, 1997.

The Wei et al patent is citable as prior art only as of the filing date of provisional application 60/071,987 of January 20, 1998. On the basis of the information at hand, it is unclear whether the provisional application has the same or similar content to the content of the '258 patent as issued or is significantly different. This response is provided on the basis of the content
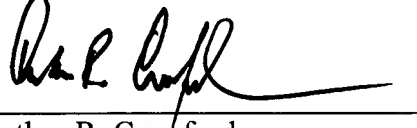
of the '258 patent as issued and without prejudice to applicants' consulting and assessing the actual text of the January 20, 1998 provisional application. This response is not an acknowledgement that the entire content of the '258 patent is available as prior art for these reasons.

For the above reasons it is respectfully submitted that the claims of this application as above amended define inventive subject matter. Reconsideration and allowance are solicited.

Respectfully submitted,

NIXON & VANDERHYE P.C.

By: _____

Arthur R. Crawford
Reg. No. 25,327

ARC:eaw
901 North Glebe Road, 11th Floor
Arlington, VA 22203-1808
Telephone: (703) 816-4000
Facsimile: (703) 816-4100

1030797

Porous silicon microcavities.

Claudio Vinegoni[†]

Department of Physics and Astronomy, University of Pittsburgh, Pittsburgh PA, USA

Massimo Cazzanelli

Department of Physics, Trinity College, Dublin 2, Ireland

L Pavesi

INFM and Dipartimento di Fisica, Università di Trento, Trento, Italy

(October, 2000)

Contents

3

I. INTRODUCTION

The end of this century has seen a progressive move down in dimensionality of the semiconductor systems. Quantum wells, quantum wires and quantum dots were exotic terms a decade ago, while now they are at the very basis of many devices, e.g. single electron memories or transistors. At the same time, new applications for silicon has been found either in the form of an alloy with germanium for high frequency applications, or as materials for photonics applications. This last aspect is the focus of this review paper.

The promotion of silicon from the key materials for micro-electronics to an interesting and competitive material for photonics' applications is based on the fact that the spontaneous emission of a material depends on the coupling between the initial and final state of the optical emission process, i.e. on the coupling between the electronic systems and the photons. This is stated by the Fermi golden rule which says that the spontaneous emission rate $R_{sp}(\hbar\omega)$ of a material is given by

$$R_{sp}(\hbar\omega) \propto \Gamma(\hbar\omega) \times M_{eh}(\hbar\omega) \,, \tag{1}$$

where $\Gamma(\hbar\omega)$ is the photon mode density and $M_{eh}(\hbar\omega)$ is the element of the dipole matrix between the initial and the final state of the optical transition. By reducing the dimensionality of both the electronic and the optical system it is possible to dramatically change the spontaneous emission of silicon.

The first exploitation of this fact was in reducing the dimensionality of the electronic system in silicon by using a cheap and easy technique. In fact, the first success in the improvement of the silicon emission properties was the discovery of efficient light emission in porous silicon (PS) where nanocrystalline Si is formed and quantum confinement of photoexcited carriers yields to a band-gap widening and an increased transition rate [1]. These observations have promoted a wide interest worldwide with the development of many other low-dimensional silicon based system: nanocrystals, quantum wells, superlattices, nanometric multilayers of amorphous material, etc.

4

The second accomplishment was made by Prof. Pavesi's group in 1995 with the development of all porous silicon microcavities (PSM) in which the active PS is placed in an optical resonator formed by two PS mirrors (dielectric Bragg reflectors, DBR) [2,3]. In this system not only the electronic system of silicon is changed through the use of porous silicon, but also the photonic system is promoted to lower dimensionality within a Fabry-Perot structure. Only those photons with the same wavelength as the Fabry-Perot resonance can propagate through the structure and couple with the electronic transitions. A one dimensional confinement of the photons is indeed reached.

The use of all porous silicon microcavities thus put to full exploitation the possibility to change with Eq. 1, the spontaneous emission properties of silicon. The aim of this review is to show how this is feasible and which interesting and new properties these systems show.

The article is organized as follows:

- in Section II the structure and optical properties of PS are presented;

- Section III reports a general introduction to dielectric multilayers;

- in Section IV semiconductor microcavities are introduced;

- PS multilayers are discussed in Section V;

- Section VI deals with PS microcavities;

- in Section VII some applications of PS microcavities are presented;

- conclusions are drawn in Section VIII.

II. POROUS SILICON

A. The fabrication of porous silicon

Porous silicon (PS) was discovered in 1956 by Uhlir [4] while performing electropolishing experiments on Silicon wafers using an HF-containing electrolyte. He found that increasing the current over a certain threshold, a partial dissolution of the silicon wafer started to occur. PS formation is then obtained by electrochemical dissolution of Si wafers in aqueous or ethanoic HF solutions.

1. How to produce porous silicon

A quite simple apparatus can be used to produce PS and the typical setup is shown in Fig. 1 [5]. The anode is the silicon wafer itself; the cathode can be a platinum spiral or a circular grid; the electrolyte is composed of high purity HF in 40% aqueous solution diluted in ethanol (C_2H_5OH) at different concentrations. The dilution is necessary due to the hydrophobic character of the clean Si surface: in this way it is possible to increase the wettability of the PS surface. In fact, ethanoic solutions infiltrate the pores; on the contrary purely aqueous HF solutions do not. This is very important for the lateral homogeneity and the uniformity of the PS layer in depth. In addition, during the reaction there is a hydrogen release. Bubbles form and stick on the Si surface in pure aqueous solutions; they can be removed if ethanol (or some other surfactant) is present. For the same reason, a careful design of the anodization cell is necessary, in order to promote hydrogen-bubbles removal. Moreover, it has been observed that the lateral homogeneity and the surface roughness can be reduced increasing the electrolyte viscosity as well as by diminishing the temperature or by introducing glycerol in the HF solution [6].

The process of growth is obtained either by controlling the anodic current or the potential. It is widely diffused the practice of working with constant current, because it allows a better control of the porosity, thickness and reproducibility of the PS layer. Different kinds of cells

can be used for the production of PS.

The first kind of cell is presented in Fig. 2 [7]. The Si wafer acts as the anode; the cathode is generally made of platinum, or other HF-resistant and conducting material. The cell body is usually made of highly acid-resistant polymer such as teflon. In this cell PS is formed all over the wafer surface exposed to HF. The advantage of this cell geometry is the simplicity of equipment. On the opposite the main drawback is the inhomogeneity in the porosity and the thickness of the PS layers. The presence of a difference in the potential between the top (point A in Fig. 2) and the bottom (point B in Fig. 2) of such a cell, leads to different values of the local current density.

The second type of cell is the single cell approach that uses a back-side contact and has been already shown in Fig. 1. In this cell, the Si wafer is placed on a copper disk and sealed through an O-ring, so that only the front side of the sample is exposed to the electrolyte. The copper disk has to be cleaned with a lapping machine in order to remove the oxide film that forms itself after many etching processes. When a Si wafer with high resistivity (that is more than few mΩ/cm) is used, a high dose implantation on the back surface of the wafer is required to improve the electrical contact between the wafer and the copper disk. This geometry is particularly indicated for an uniform illumination of the sample during the etching.

The third type of cell is a double tank geometry with an electrolytic back-side contact. This cell (Fig. 3 [7]) consists of two half-cells whose contain the platinum electrodes; the Si wafer is used to separate the two half-cells. HF solution is made flowing by HF resistant pumps. In this way it is possible to remove the gas bubbles and to avoid the decrease in the local concentration of HF. The current flows from one electrode to the other through the Si wafer. In this configuration the back-side of the Si wafer acts as a secondary cathode where proton reduction takes place leading to hydrogen evolution. The front side of the wafer acts as a secondary anode, where PS is formed. Since the back-side contact is made electrolytically, no metallization is required, but a high-dose implantation is still necessary for highly resistive wafers. If illumination is required, the material used in the cell should

be plexiglas, which is transparent and HF resistant (up to 15% HF). With this cell, both front and back side illumination is possible.

2. I-V Characteristics

It is known that applying a potential to silicon leads to an external current flowing through the system. In Fig. 4 it is shown the characteristic i-V curves for n- and p-type doped Si in aqueous HF [8]. Some similarities exist between the i-V curves shown in Fig. 4 and the ones of a semiconductor-electrolyte interface which behaves as a normal Schottky diode barrier. Some differences exist too: first of all, even though the type of majority carriers changes between n- and p-type, the chemical reactions at the interface remain the same. Second the reverse-bias dark currents have been reported at least three orders of magnitude higher than those normally expected for Schottky diodes.

Both n- and p-type silicon is stable under cathodic polarization. The only important cathodic reaction is the reduction of water at the Si/HF interface, with the contemporary formation of gaseous hydrogen. This reaction occurs only at high cathodic overpotentials or, using Schottky-diode terminology, at reverse biased breakdown.

Dissolution of silicon occurs only under anodic polarization. At high anodic overpotentials the Si surface goes under electropolishing. On the contrary at low anodic overpotentials, the surface morphology is dominated by a dense array of channels penetrating deeply into the bulk of the Si [9]. The pore formation occurs only during the initial rising part of the i-V curve, for a potential value below the potential of the small sharp peak (see Fig. 4 [8]). The current peak is named as the electropolishing peak.

The quantitative values of the i-V curves, as well as the values corresponding to the electropolishing peak, depend on the etching parameters and wafer doping. For n-type substrates, this typical i-V behaviour is observed only under illumination because hole supply is needed. We refer the reader interested to the details about these features to more specialistic papers [8,10,11].

Up to now several different mechanisms regarding the dissolution chemistry of silicon have been proposed but it is generally accepted that holes are required for both electropolishing and pores formation. During the process of pores formation two hydrogen atoms are released for every Si atom that reacted [12,13]. The hydrogen creation decreases approaching the electropolishing regime and stops during the electropolishing. Two electrons for each Si atom that reacted are consumed during the pore formation, and about four electrons are used under electropolishing regime [11,12,14]. The global anodic semi-reactions can be written during pore formation as

$$Si + 6HF \longrightarrow H_2SiF_6 + H_2 + 2H^+ + 2e^-, \qquad (2)$$
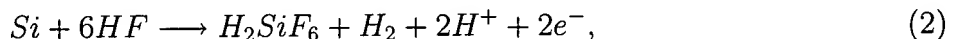
and during electropolishing as

$$Si + 6HF \longrightarrow H_2SiF_6 + 4H^+ + 4e^-. \qquad (3)$$

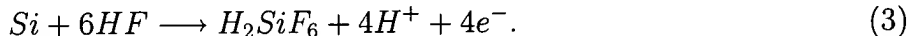In both cases, the final and stable product for Si in HF is H_2SiF_6, or some of its ionized forms; it follows that during the pore formation only two of the four available Si electrons participate in an interface charge transfer while the remaining two undergo a corrosive hydrogen formation. During the electropolishing instead all four Si electrons are electrochemically active.

Amongst the various models proposed for the Si dissolution reaction, the mechanism presented by Lehmann and Gösele [15] (shown in Fig. 5 [16]) is the most accepted in the PS community. The mechanism is based on a surface bound oxidation scheme, with hole capture, and subsequent electron injection, which leads to the divalent Si oxidation state. According to the model, the Si hydride bonds passivate the Si surface unless a hole is available. Once PS is formed, the interpore region is depleted of holes as evidenced by the high resistivity of PS ($\simeq 10^6$ Ωcm similar to intrinsic Si) [11]. Further dissolution occurs only at the pore tips, where enough holes are available (see Fig. 6 [17]). In this way the etching of

9

PS proceeds in depth with an overall directionality which follows the anodic current paths inside Si. Once a PS layer is formed no more electrochemical etching occurs but a slow chemical one starts, due to the permanence in HF.

4. Etching parameters

The main requirements for PS formation are:

1. The Si wafer must be anodically biased. This corresponds to forward biasing for p-type doped Si, reverse biasing for n-type doped Si.

2. For n-type doped and semi-insulating p-type doped Si, light must be supplied.

3. Current densities below the critical value, j_{PS}, must be used.

The first two conditions are due to the fact that holes are consumed during the Si etching. When the third condition is violated, the reaction is limited by mass transfer to the solution: holes pile up at the Si-HF interface and electropolishing occurs.

For all the three conditions mentioned above the holes play an important role: in fact, PS formation is a self-regulated mechanism, with hole depletion as the limiting agent. The dissolution reaction begins at defects on the Si wafer surface; the pores are formed and their walls are eroded until they are emptied of the holes. This formation process passivates them from further attack, and the reaction proceeds at the pore end (Fig. 6). Amongst the various models proposed until now in order to explain the hole depletion [8] two are worth to be mentioned. Beale et al. [11] attribute the absence of holes in PS to the overlap of the depletion regions formed on the pore walls in a Schottky diode picture of the Si/electrolyte interface. Lehmann and Gösele [15] proposed the quantum model, by observing that the photoluminescence data are blue-shifted with respect to the Si gap due to exciton confinement similar to the "particle-in-a-box" quantum problem. In fact the difference between the energies of the crystalline silicon and the PS acts as a barrier for the hole diffusion from the crystalline silicon to the pores.

10

In accordance with the previous mechanisms, Lehmann [18] proposed that the depletion width at the silicon/electrolyte interface depends on the doping. The depletion width is quite large for n-type doped Si and this fact gives account for the formation of macropores; while it exhibits a smaller value in n^+-type and p^+-type doped Si, that leads to mesopores, and it is zero for p-type doped Si. On the other side, the depletion due to the quantum confinement is present independently of the substrate type, resulting in the formation of micropores. In this way the macropores or mesopores, typical of n^--type, n^+-type and p^+-type doped Si, are coated by micropores.

The overall etching process is self-adjusting and the average pore size is given by the electrochemical parameters only.

The quantum confinement effect yields to microporous Si, with pore diameters below 2 nm. For a thin depletion layer, holes tunnel from Si to the electrolyte; this leads to the formation of mesopores, whose diameter ranges from 2 to 50 nm.

With thicker depletion, pore sizes pass from 50 nm to several μm and are independent of the layer thickness. These structures are named macropores. As the light emission originates in microporous Si, samples made from lightly p-type doped Si wafers have the best luminescent properties.

PS is macroscopically and empirically characterized by its porosity, P, defined as the fraction of voids inside the porous layer vs. the starting silicon; it is usually measured through a gravimetric technique that implies the measurement of the starting weight of the sample and the subsequent weight of the sample after the etching:

$$P = \frac{W_1 - W_2}{W_1 - W_3} \, , \tag{4}$$

where W_1, W_2 and W_3 are respectively the weight of the wafer before the electrochemical etch, after the electrochemical etch and after the porous layer has been removed, respectively; the removal is made through a dip for some minutes in an aqueous solution of KOH (3% in volume), that leads to a selective removal of the PS layer without reacting with the bulk crystalline silicon.

11

Different techniques are employed to determine the porous layer thickness d. From the gravimetric measurements,

$$d = \frac{W_1 - W_3}{\rho S} \, ,$$ (5)

where ρ is the silicon density and S the etched surface, or measuring, with a profilometer, the depth of the hole left after dissolution of the PS layer. Optical and electrical microscope observations are also reported.

As a by-product of such measurements a profile of the hole is obtained; an example of this is shown in Fig. 7 [2].

The PS formation is influenced by the following parameters:

- The substrate doping.

- The current density (which determines the depletion width and the carrier injection rate).

- The HF concentration (the higher the concentration, the lower the pore sizes and the porosity). HF concentration determines j_{PS}, that is the upper limit to current density values. With a fixed and low HF concentration the range over which the current density can be varied is short, and it becomes wider by increasing the HF concentration.

- The solvent where the HF is diluted: since PS is organophilic and hydrophobic, the use of ethanol guarantees a higher homogeneity, due to a better wettability of the surface than deionized water.

- The etching time: longer etching times lead to thicker layers, but for long times an anisotropy in depth in the layer due to the chemical action of the electrolyte is introduced.

- The illumination during the etch.

The porosity, thickness, pore diameter and microstructure of PS, depend on the anodization conditions. These conditions include HF concentration, current density, wafer type and

resistivity, anodization duration, illumination (required for n-type silicon and semi-insulating p-type silicon), temperature, ambient humidity and drying conditions (see table I).

For p-type doped substrates, and for a given HF concentration the porosity increases with increasing current density. For fixed current density, the porosity decreases with HF concentration (see Fig. 8 [19,7]). Fixing the HF concentration and the current density, the porosity increases with the thickness. This happens because of the extra chemical dissolution of the PS layer in HF. In order to have a thicker layer, a longer anodization time is required. A longer permanence time of Si in HF solution results in a higher mass of chemically dissolved silicon. This effect is more important for lightly doped Si, while it is almost negligible for heavily doped Si. This is due to the lower specific surface area.

Samples of porosity between 20% and 75% can be fabricated with ease. Due to the fact that the fragile Si skeleton is unable to withstand the large capillary forces which are present within the pores during drying, higher porosities are difficult to achieve. What happens is that the samples crack and peel from the substrate. Sample cracking can be avoided via various drying techniques that have been proposed: supercritical drying [20], freeze drying [21], the use of benzene during sample rinsing [22] and a simple slow rate of evaporation.

5. Drying of the samples

An important step in the fabrication process of high quality PS layers is the drying recipe employed immediately after the etch of the wafer. It has been reported several times that the formation of PS, with high porosity (greater than 70%) and/or thickness (of the order of microns) leads to a systematical cracking of the layer during the evaporation of the solvent. A typical example of cracking pattern is reported in Fig. 9 [16]. The origin of the cracking is the large capillary stress associated with the evaporation from the pores. During the evaporation a gas/liquid interface forms inside the pores and a pressure drop Δp across the gas/liquid interface occurs. Δp is given by

$$\Delta p = \gamma \frac{S \cos \Theta}{P} , \tag{6}$$

13

where γ is the liquid surface tension, S the interface area, $\cos \Theta$ is the curvature of the gas/liquid interface, and P the porosity. Δp as high as some MPa are measured [23](see Fig. 10).

In paragraph II A 4 we anticipated the different methods reported in literature about the optimization of the drying procedures. Here we report about the two worth to be mentioned:

- pentane drying

- supercritical drying

The pentane drying is the easiest to implement. Pentane has a very low surface tension (i.e. low γ values in Eq. 6), and shows no chemical interaction with PS (unlike ethanol). Using pentane as rinser it is possible to reduce strongly the capillary tension; but since water and pentane are non-miscible liquids, ethanol or methanol have to be used as intermediate liquids. Using this drying technique PS layers with porosity values up to 90 % and thickness up to 5 μm exhibit no cracking pattern after drying.

Supercritical drying [20] is based on the exploitation of the fact that when the pressure is raised the interface between the liquid and the gas phase becomes unstable and when the pressure is larger than the critical pressure the interface gas/liquid disappears and a mixture of the two phases appears (supercritical fluid). This is the most efficient drying method. In such a technique, the HF solution is replaced by a suitable "liquid", usually carbon dioxide, under high pressure [20]. The phase is then moved above the critical point (31 °C) by raising the pressure and temperature, as schematically shown in Fig. 11 path a-b, b-c [16]. Then the gas is removed by the supercritical liquid (Fig. 11 path c-d). This drying procedure allows to produce layers with very high thickness and porosity values (up to 95 %) improving the optical flatness and the homogeneity as well [24].

However supercritical drying is expensive and complicate to implement so other drying methods are normally employed.

14

B. The structure of porous silicon

PS presents itself on a long length scale quite uniform; on a microscopically scale instead, its structure is formed by silicon nanocrystals or silicon filaments coated by an amorphous matrix. An ideal rapresentation of a porous silicon layer is shown in Fig. 12 [25]. The existence of both the crystalline and amorphous part is confirmed by various techniques as X-ray diffraction [26], Raman spectroscopy [27], Extended X-rays Absorption Fine Structure (EXAFS) [28], electron microscopy [29]. For what concerns the coating matrix it has been shown that it is disordered [30,31] and time dependent [32]. Moreover the coating matrix can be changed by post-etching treatments.

1. Internal surface

The large quantity of internal voids inside PS causes the presence of a very large inner surface (of the order of 500 m^2/cm^3) [32]. The large amount of surface defects is mostly due to dangling bonds and acts as an efficient luminescence quencher [33,34]. It follows that PS is a material which results from a "forest" of pores that extends from the outer surface in depth along the direction determined by the current flow. The region among the pores is formed by interconnected Si nano-crystals that are arranged in accordance to highly constrained and filamentary structures.

2. Pore and size shape

A direct image of PS layers is given by Transmission Electron Microscopy (TEM) [35]. Using this technique the main properties studied are the morphology of the pore network and the crystallite dimensions [11,20,21,36,37,29,38–58].

During the 80's , Beale et al. [11] studied PS layers formed using a wide range of anodization's conditions and starting from different substrates. This studies were continued in this decade focusing on the luminescent and (heavily) oxidized materials [1]. It is important

to note that the preparation techniques of TEM samples have an impact on the final results. The chemical thinning transforms the porous material in a microcrystalline one, whereas ion milling originates an amorphisation of the material, even if morphological informations are still obtainable. Cleavage or scraping of fragments from the substrate appears to be the less destructive preparation procedure and it is particularly suitable for highly porous materials.

The difference in morphology are evident for p-type and n-type material as shown in Fig. 13 [8]. For p-type doped Si both pore size and inter-pore spacing are very small, typically between 1 and 5 nm, and the pore network looks very homogeneous and interconnected. With the increasing of the concentration, the pore sizes and the inter-pore spacing increase, while the specific surface area decreases. The result is that the structure becomes anisotropic, with long voids running perpendicular to the surface; this fact is less evident for p^- than for p^+ material. In the latter case the anisotropy of the microstructure is very evident, as shown in Fig. 13 (c) for highly doped material. For n-type doped Si the situation is more complicate. Generally, pores in n-type doped Si are much larger than in p-type doped Si, and pore size and inter-pore spacing decrease increasing the dopant concentrations. Lightly doped n-type substrates anodized in the dark lead to low porosity, (1-10 %), with pores in the micrometer range. Under illumination instead, higher values of porosity can be achieved, and mesopores are formed together with macropores. The final structure depends strongly on the anodization conditions. While highly n- and p-type doped Si show similar structures, (compare Fig. 13 (c) and (d)), in n-type doped Si the pores tend to form a randomly directed filaments and to "pipe", forming large straight channels as approaching the electropolishing regime (see Fig. 13 (b)). Both the filaments and the channels propagate only in the $\langle 100 \rangle$ directions, probably because the (100) planes present the most sterically favoured geometry for the chemical etch [8]. TEM specimens with porosities as high as 80%-85% have been prepared by direct cleavage [29,1] or by scraping [51]. The TEM images [1] present narrow ondulating Si columns with diameters less than 3 nm, nevertheless the crystalline nature of the Si nanostructures is well assessed.

Transmission Electron Diffraction (TED) studies confirm the results collected above.

16

The TED patterns confirm both the crystalline character of PS and the difference in the structure between the p-type and the n-type layers and the dependence from the level of doping and porosity. Beside, in the case of luminescent materials, the TED studies [29,50] demonstrated the presence of silicon nanocrystallites. This was also found for highly luminescent, 95 % porosity supercritically dried p^+ material, where the TED pattern shows that the "concentration of randomly aligned crystallites has been dramatically reduced in contrast to silicon layer dried conventionally" [20].

3. Scanning tunneling microscopy, atomic force microscope

In addition to electron microscopy studies, a variety of scanning probe microscopy investigations can be found in the literature [59–73]. Atomic Force Microscopy (AFM) studies focus entirely on the nanoscale characterization of porous silicon films, thus in most studies, AFM is applied together with other optical or morphological characterization techniques [62–69,74]. AFM can prove the presence of silicon features with diameters of about 10 nm. The presence of ¡5 nm large topography features in the images of porous silicon has been also claimed [61,68,73]. Due to the geometry of tips commonly used, AFM does not allow the imaging of deep pores. It is, in fact, not possible to image nanometer-wide pores into depth that are comparable to their widths. As a result, AFM allows only the imaging of the top end of the pores, which is a disadvantage of this technique compared with electron microscopy.

In the case of Scanning Tunneling Microscopy (STM), observations are limited from the high resistivity of the material. To circumvent this problem one can use three different method [72]; a thin film of the material can be prepared, it can then be deposited onto conductive surfaces or even the surface of PS can be illuminated. This last technique (photoassisted STM) seems to be the most favourable. The PS surface consists of small ($\sim$ 2 nm) pillar-like structures closely interconnected. There are also holes, 3-5 nm in size. Smaller structures can be seen on the walls of some holes. The use of STM in the spectroscopic

mode has also permitted to reveal the signature of the widening of the band gap due to the quantum confinement [72,75]. Moreover it has been demonstrated that it is also possible to use the tunneling tip to stimulate local photon emission by electron injection [76–78]

4. Crystalline nature of PS skeleton

X-ray diffraction is the experimental method normally used to evaluate the degree of crystallinity. The X-ray diffraction setup allows a direct determination of the lattice parameter a of the PS layer. The value of a can be determined from differential measurements of the diffraction Bragg angle. Determination of the lattice parameter variation with respect to crystalline silicon is quite complicated [79,80], probably as a consequence of the large pores that are present. p^- samples reveal a greater lattice expansion. Bomchil et al. [42] reported $\frac{\Delta a}{a} = 4 \times 10^{-3}$ and 10^{-3} for p^- and p^+ samples of 56% and 72% porosities respectively. Barla et al. [81,82] found a linear growth of the lattice parameter expansion for p^+-PS going from 3 to 8×10^{-4}, increasing the porosity from 30 to 80%. The same behaviour has been reported by Bellet and Dolino [83] even if the measured values were larger. The origin of this expansion is related to the hydrogen-silicon bonds at the inner surface of the PS layer. In fact, a correlation has been found between hydrogen desorption and strain during thermal annealing [84–86]. When hydrogen desorption takes place, a sharp contraction in the lattice parameter occurs. On the contrary the formation of oxide layer due to the aging or thermal or anodic oxidation originates a further increase of $\frac{\Delta a}{a}$ [54,85,87–89]. In the last case a saturation value of the expansion coefficient at a constant value is reached. Whereas X-ray diffraction at wide angle gives important informations on the lattice parameter and the stress, small-angle X-ray diffraction (SAXS) elucidates the size and the morphology of the sample. With this method the anisotropic character of the p^+ microstructure has been reassessed [90]. Moreover SAXS studies have confirmed that for luminescent PS the morphology is that of an interconnected network of Si quantum wires, whose dimensions are of the order of 3-4 nm [46,91].

EXAFS (extended x-ray absorption fine structure) is essentially a bulk technique [92]. However techniques more appropriate to the study of surfaces have been developed, like SEXAFS (surface-EXAFS) [93] that probes individual site and reflected EXFAS (REFLEX-AFS) which uses the possibility of varying the angle of incidence of the X-rays. Of particular importance, in the case of samples that show photoluminescence, is also XEOL (X-ray excitations of optical luminescence, also called photoluminescence yield (PLY)): a technique that combines an EXAFS measurement with the excitation of the PL [94].

In the case of porous silicon the EXAFS technique has been applied in several detection modes: transmission [95], total electron yield (TEY) [96–102], and photoluminescence yield (XEOL/PLY) [103–107]. In particular TEY measurements have been used as a direct measurement of the quantum confinement effect on the nanostructure of PS. Moreover TEY and PLY, recorded at the same time for both porous silicon and siloxene [103], have demonstrated that the origin of PL in PS is different from that of siloxene. It is worthwhile to note that whereas TEY measures secondary electrons escaping from the first few hundreds of Å beneath the surface, PLY(XEOL) measures the emission of visible radiation.

Very recently a careful study on the sensitivity of the x-ray excited optical luminescence to the local structure of the luminescent Si sites has been performed by Dalba and coworkers [106–108]. X-ray absorption near edge structure (XANES) were recorded in TEY and PLY(XEOL) mode at the Si K-edge of porous Si before and after washing it with HF for removing oxygen. EXAFS spectra were recorded in TEY and PLY (XEOL) modes of two different samples obtained from a 3 Ωcm resistivity c-Si wafer with current densities of 60 and 10 mA/cm^2. From these spectra the following conclusions can be reached [106,107]: the photoluminescence yield induced by X-rays in PS strongly depends on the sample preparation parameters, TEY and PLY XANES give different informations; TEY-XANES is sensitive both to silicon-oxygen and silicon-silicon bonds, whereas PLY-XANES originates only from Si-Si bonds, finally a well-defined crystalline order is clearly present in PS. Concerning the

EXAFS results, the TEY data confirm the presence of crystalline structures on a scale of few nanometers, however while TEY-EXAFS gives an average structural information on all Si sites, luminescent and non- luminescent sites, PLY-EXAFS selects the light-emitting Si sites.

The influence of the PS preparation parameters is pointed out also from the different conclusion about the structural nature of PS (dots or wires?) reached in two EXAFS studies by Schuppler at al. [96] and Zhang and Bayliss [101]. The first group, starting from the fits to their EXAFS data, rules out nanowires as the origin of PL for PS and suggests confined nanodots of particularly small dimensions in the order of $\sim$ 0.7 - 2.5 nm ; instead Zhang and Bayliss studying freshly etched PS emitting in the red, yellow and orange (PL peaks at 690, 580, and 520 nm respectively) conclude that the structure of PS is formed by a network of wires , with average diameters of 2.2, 1.9 and 1.3 nm. These dimensions agree with the results from XAFS studies [95], TEM, and X-ray measurements. The difference in the two experiments can be traced out to the very different resistance of the Si wafers used for PS preparation (>50 Ωcm for the Schuppler samples, 3 Ωcm in the Zhang and Bayliss case).

6. Thermal effects

The thermal conductivity is an important physical parameter in PS. Due to its porous structure, PS shows a low thermal conductivity and microporous Si can be considered as a good thermal insulator. For electroluminescent devices based on PS it can be a serious limitation; this because the quantum efficiency is still low and a sensible amount of heat has to be dissipated in the porous layer. On the other hand, this property can be used to form thermally isolated layers on Si.

Recent measurements of thermal properties [109] are strongly in disagreement, probably because of the different morphologies of the investigated samples (see Fig. 14 [110]).

The conductivity can be calculated by the analysis of thermal waves travelling through the sample. For PS formed on lightly p-type doped Si, the thermal conductivity is very low,

even lower than the value for SiO_2 ($\simeq 1.4$ W m^{-1} K^{-1}). This is caused both by the granular structure that does not transport heat easily and by the presence of the pores whose prevents the heat transfer among crystallites. When the material is partially oxidized, the thermal conductivity increases, because oxygen is incorporated in the film; therefore, the porosity decreases and the transport increases.

PS formed on p^+-type doped Si shows a higher thermal conductivity, about one half the bulk value (150 W m^{-1} K^{-1}). In this case, PS is known to be mesoporous. It can be considered a sponge of Si with pores about 10 nm wide, so that continuous pathways of solid Si are present. The thermal conductivity for PS formed on p^+-type doped Si can be evaluated from the thermal conductivity of bulk Si trough the porosity, while for the PS formed on lightly doped Si the data are critically dependent on the preparation conditions.

7. Elastic effects

The elastic properties of PS, which are drastically different from those of bulk Si, are responsible for the peculiar characteristics of PS layers: its fragility or mechanical instability. In a solid material like PS, the elastic modulus has to be considered at two different levels. At the crystallite level, the elastic modulus is determined by the stiffness of the atomic bonds, which does not differ from that of bulk Si. At the macroscopic level the Young modulus is related to the porous structure of the solid. This macroscopic modulus is expected to be smaller than that of bulk material and to decrease with increasing porosity. Young modulus of PS can be determined by means of four different techniques: Brillouin scattering, X-ray diffraction, acoustic wave propagation, and nanoindentation [111]. The values obtained by the different methods do not differ so much, as reported in Fig. 15.

PS formed on p^+-type doped Si has open pores and for such open-cell structures the Young modulus Y_p is expected to vary according to the following equation [112]

$$Y_p = C Y_B \rho_r^2 \tag{7}$$

where Y_p is the Young modulus of the sample, Y_B is the elastic modulus for the bulk Si, ρ

is the relative density and C is a phenomenological constant of the order of unity. Fig. 15 shows that the experimental determination [111,110] is in good agreement with the parabolic function (nanoindentation data), giving $CY_B = 120$ GPa, not too different from the Young's modulus of bulk Si (162 GPa).

For PS formed on p-type doped Si, the very complicated pore morphology does not fulfill the model assumptions whose lead to Eq. 7. However, PS formed on p-type doped Si material appears to be less stiff than PS formed on p^+-type doped Si with the same porosity level.

Using a high resolution X-ray double diffractometer it has been found [113] that the diffraction peak of a PS layer is almost as narrow as the peak of the Si substrate, but slightly shifted to a smaller diffraction angle [114], as observed in Fig. 16. The angular distance between the two peaks is directly related to the lattice mismatch parameter. The related strain is strongly dependent on the porosity (Fig. 17), on the doping, and on the type of substrate and oxidation [115]. The strain increases with oxidation, which corresponds to the growth of a thin oxide layer on the internal surface of PS. For this reason the strain in PS increases with time [116], with heating in air [117] or anodic oxidation [118]. While heating in air produces a large oxidation strain, annealing performed in an inert environment or under vacuum produces a contraction due to H desorption [119].

The origin of strain is related to the large internal surface of PS. Probably the strain is due to the presence of SiH_x bonds on the crystallites surface, and the contraction under vacuum annealing during desorption of hydrogen supports this hypothesis. Another explanation could be that the oxide layer expands. However, there is little oxide in freshly etched PS, and it is hard to attribute the initial strain to oxide formation, while it is likely that the increase of strain with time is due to the growth of an oxide layer.

The hardness is defined as the resistance of a solid to plastic deformations [120], and can be measured with different techniques. The most widely used ones are static indentation tests whose give the hardness as the ratio of the applied force vs. the area of indentation.

Fig. 18 shows the variations of the hardness vs. the porosity for p^+ and p^-type PS

22

[120]. It results that the hardness of the samples with different substrates is comparable, which means that the morphology is not so important. For both types of PS the hardness decreases with the increasing of porosity. At low porosity the decrease in the hardness can be expressed as

$$H = H_o \times (1 - P)^m \qquad (8)$$

where $m = 2/3$ and H_o is the hardness of bulk Si (solid line in Fig. 18). At high porosities the hardness drops at values lower than the previous ones, indicating changes in the structure of the samples.

8. Raman Spectroscopy

Among the other optical investigation methods, Raman spectroscopy, and especially micro-Raman spectroscopy, can give indirect information on the microstructure of PS. While in bulk Si, the interaction of the optical phonons with incident photons is limited to the center of the Brillouin zone, the presence of nanocrystals in PS relaxes the k-selection rule, with a broadening of the associated Raman peak [121].

The Raman spectra are analyzed in term of specific contributions from amorphous and nanocrystalline Si. A gaussian line centered at 470 cm^{-1} with a width of 55 cm^{-1} is used as representative of the amorphous contribution. The Si nanocrystals contribution is described by using a phenomenological model based on the spatial confinement of phonons: [122,123]

$$I(\omega) = \int_0^\infty I_L(\omega) P(L) dL. \qquad (9)$$

$I(\omega)$ is the Raman spectrum, $I_L(\omega)$ is the first-order Raman scattering from phonons confined within nanocrystals with size L, as calculated by Campbell and Fauchet [123], and $P(L)$ is the crystallite size distribution, i.e. a Gaussian distribution with mean L_o and dispersion σ. The results of a fitting procedure are reported in Ref. [121]. The fitting parameters are $L_o = 6.5$ (4.5) nm, $\sigma = 2.2$ (1.6) nm and the relative weight of the amorphous to the crystalline part $\simeq 10$ % for the top (bottom) spectrum.

Sizes larger than those measured by EXAFS are reported by Raman analysis. A partial answer to this discrepancy is given by EXAFS measured in XEOL (X-rays excited optical luminescence) configurations where the energy resolved EXAFS signal is measured on the luminescence band [124]. The sizes of the Si nanocrystals whose emit in the visible, is significantly smaller than the average sizes of Si nanocrystals in PS as measured by standard EXAFS or Raman scattering.

9. BET measurements

Accurate determination of pore size distribution in mesoporous Si is usually performed by the analysis of the adsorption isotherms of gases at low temperature (BET technique) [125]. The physical adsorption by a porous surface is increased relative to a smooth one because of capillary condensation into pores. This increase in the adsorption starts when the gas pressure is high enough to fill the smallest pores.

Fig. 19 shows a typical adsorption isotherm for a heavily p-type doped PS layer [126]. The first part of the curve, at low relative pressures, corresponds to the adsorption from the porous surface and allows to determine the total surface area [127]. The sharp increase at higher relative pressures is related to capillary condensation of the gas into the pores. The final plateau indicates the complete filling of the pores, and the amount of liquid corresponding to the volume of the gas adsorbed allows the determination of porosity. The isotherm shows an hysteresis loop, because lowering the pressure, some evaporation of the liquid from the pores occurs. There are different methods to obtain pore size distribution from adsorption isotherms, but the most employed is the BJH (Barrett-Joyner-Halenda) method [128] which is normally used for mesoporous Si: the shape of a typical adsorption isotherm is quite different from Fig. 19, because the rapid intake of gas happens at low relative pressures, with no hysteresis loop. Extracting accurate pore distribution from this type of adsorption isotherm is difficult, and becomes even more complicate when micro and mesopores coexist in the same sample.

C. Chemical properties of porous silicon

1. Chemical composition of porous silicon

As mentioned before the internal surface of PS is very large. Values as high as 1000 m^2/cm^3 can be measured [129](see Fig. 20). Such a large surface contains an enormous quantity of impurities, coming from the electrolyte used for electrochemical etching, from the ambient air and from the wafer itself. So it is important to know the chemical composition of PS because the optical and the electrical properties depend on the impurity content and the surface passivation.

The original impurity which is always found in PS layers is hydrogen. Infrared absorption (IR) experiments have shown the presence of Si-H_x groups (x = 1, 2, 3) on the internal PS surface during the etching process. [30,31,130]

In Fig. 21 a typical IR spectrum of a fresh PS sample is reported [131]. The IR frequencies commonly observed in PS and their attributions are reported in Tab. II. After the formation and the drying procedure, the Si-H_x groups are still present on the inner surface for weeks and even for months, as it has been demonstrated using IR absorption and nuclear magnetic resonance. H desorption occurs during the annealing, and it has been shown [132] that hydrogen desorbs from SiH_3 groups between 300 and 400 °C. Its desorption from SiH_2 instead occurs at 400 °C and from SiH at around 500 °C.

The atomic ratio H/Si in PS has been determined using secondary ion mass spectrometry [133] (SIMS) and elastic recoil detection analysis (ERDA), and in freshly anodized samples it is as high as 0.1 - 0.6, depending on the porosity and surface area of the samples. This result means that the surface of freshly etched PS is almost totally covered by SiH_x groups.

The second original impurity found in PS is fluorine. This was demonstrated using many experimental techniques (SIMS, ERDA, ENDOR). The form in which fluorine is present in PS is still under question. Desorption experiments [132] demonstrated that SiF_3 groups desorb at the same temperature as SiH_3, indicating that SiF_3 groups are present on the

pore walls. The presence of SiF and SiF$_2$ groups have been shown by IR spectroscopy [134]. The concentration seems to be higher in samples etched in aqueous HF solutions than in ethanoic HF solutions. The content in fluorine decreases with time, and it has been proposed that SiF bonds are progressively replaced by Si-OH bonds through hydrolysis reaction with water vapor in air. On the other hand, only HF and SiF$_6^{2-}$ were found using ^{19}F NMR [135]. According to these results, fluorine is thought to come only from residual electrolyte in the pores.

Other impurities are usually incorporated after the anodization process. Several techniques [30,31,133,136,137] have detected the presence of carbon. The carbon content can be as high as 10 % in the aged samples. It can be excluded that the source of carbon is ethanol, because carbon is present in similar amounts also in samples anodized in water-HF solutions [136]. The source of carbon is the atmosphere, but the adsorbed molecules are not CO or CO$_2$, because carbon and oxygen contents are not correlated. The carbon comes from hydrocarbon molecules present in the ambient air and often also in the residual gas in analysis vacuum chambers used for SIMS, IR, XPS, etc.

The most important non-original impurity is oxygen and is normally adsorbed in a few minutes after drying in ambient air. The amount of oxygen can be as high as 1 % after fifteen minutes of air exposure, as confirmed by Electron Paramagnetic Resonance (EPR) [131], and increases to very high percentage values with the aging. IR spectra performed a few hours after the anodization on a PS layer have also shown the presence of Si-O-Si group (mode at 1065 cm^{-1} in the inset of Fig. 21). The IR absorption due to the O$_x$-Si-H groups at 2200-2500 cm^{-1} is not present in this sample; it means that the oxidation is only partial. Few days after the anodization further oxidation takes place, both through the formation of Si-O-Si groups and O-Si-H and O$_3$-Si-H groups. The existence of such groups does not modify the hydrogen passivation, and the possible presence of water simply accelerates the oxidation process.

EPR measurements also emphasize the relevance of the Si/SiO$_x$ interface in PS. In Fig. 22 the EPR spectrum of a fresh n^+ PS layer is reported. This shows two absorption lines

[131]. The broad one is due to the conduction electron spin resonance (CERS). EPR studies [138] on n^+ free standing PS layers have shown that the CERS signal is present only in the substrate, demonstrating that free carriers are absent in PS. The signal due to the dangling bonds appears clearly after subtraction of the signal corresponding to the free carriers. As shown by Pivac et al. [139] the dangling bonds are the most important paramagnetic defect at the Si/SiO_2 interface (Pb centers), and have a $\cdot Si \equiv Si_3$ structure. The other relevant paramagnetic center is the $\cdot Si \equiv SO_3$ defects (E' center). This center is formed especially in hydrogen-depleted oxide layers, as shown in the EPR spectra of Fig. 23, recorded in different PS layers irradiated with γ-rays [139].

2. Degradation under analysis

It is important to note that for a material as fragile and chemically reactive as PS, the chemical alteration under analysis is a critical parameter. Potential problems with sample degradation arise in electron microscopy and photoluminescence (PL) spectroscopy, but they are also present in a wide series of other techniques that require optical or electrical excitation, or make use of ion [29], electron [137] and X-ray beams [140].

A list of all the degradation effects of these techniques are summarized in Tab. III; quite often the structure of the sample under investigation is annealed or damaged up to a point that the experimental data collected do not reflect the original nature and composition of the starting material. This aspect is especially important in the case of aged samples. In this regard effects due to analysis degradation can be interpreted as aging effects, and in some cases can explain why the composition values reported by different groups in nominally similar layers are remarkably different. It has been demonstrated [141], for instance, that PS can efficiently getter water vapor and hydrocarbon in vacuum, especially under ion beam irradiation. In this way the concentration of O, C, and H can be altered during ion beam analysis itself, limiting the reliability of this technique, as conventionally applied.

As stated previously, PS slowly reacts with the ambient air and consequently its chemical composition and its properties evolve continuously with the storage time. The ambient condition and the time elapsed determine the oxidation level. When transferred and stored under high vacuum (HV) and in the dark, PS layers present a very low content of oxygen, undetectable by techniques such as XPS, Auger and FTIR. On the other hand, when no particular care is taken, oxygen can reach very high levels. Both optical and gravimetric techniques permit to estimate the oxide fraction; an oxide content up to 50% has been observed [13].

A typical Auger spectrum of a freshly etched PS is reported in Fig. 24 [142]. In the range observed, the Si, Cl and C related transitions are observed. Instead the peak related to O, which should lie around 510 eV, is not detected, indicating that the amount of native oxide, if present, is below the detection limit. Moreover, the lineshape of the Si related transition is characteristic of the hydrogenated Si, demonstrating that the Si dangling bonds are passivated by hydrogen and, eventually, C. After a few weeks in ambient atmosphere, the Auger spectrum of the same sample presents itself quite different. The O related transition is present around 510 eV (not shown) and the Si related lineshape is characteristic of Si bonded in a SiO_x complex (inset of Fig. 24). A small fraction of the hydrogenated Si is still present (high energy peak in the Si related transition).

4. Intentional oxidation

A wide range of post-anodization treatments on PS have been developed, for different purposes. Complete conversion into silica was the first broad application of PS, for dielectric insulation or devices in microelectronics, but many oxidation treatments have been used recently as means to improve the photostability of luminescent films (see Sec. II C 3). Fig. 25 reports an idealized scheme of the oxidation process, starting from a freshly etched PS to

a wholly oxidized porous glass [143]. Although in most cases the degree of oxidation has been revealed qualitatively, few data are available regarding the chemical composition of intentionally oxidized samples. In the anodic oxidation process, PS layers are oxidized in a selective way. Only those PS regions where the current to flows are oxidized. The complete oxidation is not achieved, because electrical isolation of parts of the Si skeleton occurs, preventing further current flow [144]. In mesoporous samples of 65 % porosity, formed on a p^--type doped substrate, about 40 % of the Si remains unoxidized at the end of the process, corresponding to about a monolayer of oxide coating. In the case of thermal oxidation, a stabilizing pretreatment at 300 °C, prior to the high temperature oxidation, is necessary in order to avoid pore coalescence. The content of oxygen at the end of the process varies with the substrate, oxidation temperature and duration. In mesoporous material, formed on n^+ -type doped substrates and oxidized at 1050 °, more than 90 % of the Si is oxidized within 30 sec. [145]. However, heavily oxidized material is still susceptible to atmospheric "aging" and contamination, simply because the oxide matrix is still porous. Indeed the water content of oxidized PS depends on the ambient humidity. Some other kinds of chemical oxidation with hydrogen peroxide, nitric acid [146] or boiling water [147] have been also reported.

5. Surface chemistry

There are many and different capping layers that can be deposited onto the outer surface of PS. The deposition and the growth of metal and metal silicide layers is important for producing structures like barrier layers, buried contacts and Schottky devices. Thermally evaporated Al capping layers deposited onto PS are effective for the reduction of the aging, and in reducing C and O adsorption. Films sputtered with Al are reported to be more effective than the thermally evaporated ones in minimizing the ambient aging effects. The main drawback is that layers with sufficient thickness to prevent aging would also prevent transmission of visible light in the photoluminescence or electroluminescence processes. So transparent capping layers such as indium thin oxide (ITO) or Si oxide are more suited for

applications involving visible light. SiO$_2$ layers can be deposited onto microporous Si by Plasma Enhanced Chemical Vapor Deposition (PECVD), but it has been shown that they are effective in preventing aging only for medium porosity PS [148]. PECVD is also used to deposit thin layers of Si$_3$N$_4$ and SiC on photoluminescent PS, improving in this way its luminescence stability [149]. Other types of capping layers are deposited by molecular beam epitaxy (MBE), including, Si, SiGe, CoSi$_2$, GaAs. In most of these experiments it is clear that the quality of the deposited layer depends both on the porosity and the doping of the underlying PS, and the best results are achieved with highly doped substrates with porosity up to 50 %.

A possible alternative to metal and dielectric capping is offered by the organic derivatisation. The reason is that this process is expected to stop at the first monolayer, and allows possible applications for sensors. In any case the tendency of Si, is to irreversibly form Si-O bonds making oxidation a strong competitive reaction. To substitute H on the inner PS surface, various chemical groups, have been used, including -CH$_2$CH$_3$ [150], -OCH$_3$ [151], triethylsiloxy and 3-thiophene methoxy [152] groups and many others [153,154]. However, the organic derivatisation quenches partially the luminescence [152,155].

D. Optical properties

1. Porous silicon bandgap

In bulk crystalline Si the term bandgap means the energy gap between the maximum of the valence band and the minimum of the conduction band, and its value can be extracted from a simple transmission spectrum. In PS, in contrast to bulk crystalline Si, exists a wide spread of bandgaps, as demonstrated by the large and inhomogeneous broadening of its visible photoluminescence band. The experimental measurements allow us to extract an average value, but the comparison is still meaningful, because the intra-sample bandgap variation is normally smaller than the inter-sample variations.

Different techniques can be used to obtain the experimental values of the PS bandgap [156]. The luminescence technique measures the recombination energy of carriers excited across the gap. The photoluminescence maxima are used for comparison, while the lineshapes of the luminescence display directly the intra-sample variation of the bandgap. Other techniques are correlated to the absorption across the gap; amongst them, transmission spectroscopy, photothermal deflection spectroscopy, photoluminescence excitation spectroscopy (PLE) and photoconductivity. It is worth to mention that the characteristics of PS diodes can also give estimates of the bandgap, but the values are critically sensitive to the validity of the model adopted. Electroluminescence measurements rely on the fact that the wavelength of the electroluminescence peak depends linearly on the applied bias. The difference between the positive and the negative bias that was required in order to obtain the same peak wavelength, gives an estimate of the PS bandgap. X-ray methods can also be employed. XAFS measures the energy required to eject electrons from PS, from which the bandgap value can be deduced. However, this technique is surface sensitive, and leads to a systematic error due to charge effects.

The photoluminescence peak positions can vary from the near infrared, close to the value of the bulk Si gap, to the blue, with a spread of about 2.0 eV. Normally the PL peaks lie about 0.2 eV below the values of the bandgap as estimated by other methods.

2. The refractive index

For any application of a material in optics or opto-electronics it is essential to know its refractive index. A very simple method to evaluate the refractive index for a film-like material is to measure the interference fringes, due to multiple reflections, in order to obtain the optical thickness (see Fig. 26) [2]. The position of the interference maxima satisfies the following equation

$$2nd\left(\frac{1}{\lambda_r} - \frac{1}{\lambda_{r+1}}\right) = 0 \qquad (10)$$

31

where n is the refractive index, d the layer thickness and λ_r the wavelength of the r-th reflectance maxima. If the layer thickness is known in an independent way, the refractive index is simply the ratio between the optical path nd and the layer thickness. This method can only be applied if the interference fringes are visible, and if the layer is thin. If the material possesses a large dispersion, other methods should be employed. A more complete evaluation requires simulation of experimental spectra. Usually reflectance or transmittance spectra are simulated using a dielectric function models whose parameters, including the layer thickness, are adjusted to fit the measured data [157]. Since reliable models are available, this method is usually successfull and permits to design the final structure in order to obtain the desired dielectric properties. The square root of the dielectric function resulting from the fit is the refractive index of the PS layer . The simulation approach requires sharp interfaces, and the sharpness depends often on the type and the quality of the substrate. Usually the required sharpness is achieved more easily with p-type substrates.

The refractive index of PS is expected to be lower than that of bulk Si, and decreases with increasing porosity, because PS is basically a mixture of air and Si. However, the averaging of the dielectric functions of the individual components is not trivial, but depends on the microtopology of the material. The application of different effective medium theory leads to different formulas [158–160]. For example, the widely used Bruggeman [159] formula leads to the following symmetric expression

$$f\frac{\epsilon - \epsilon_{eff}}{\epsilon + 2\epsilon_{eff}} + (1 - f)\frac{\epsilon_M - \epsilon_{eff}}{\epsilon_M + 2\epsilon_{eff}} = 0 \tag{11}$$

where f describes the volumetric fraction, ϵ and ϵ_M are the dielectric functions of Si and the embedding medium (air) and ϵ_{eff} is the effective dielectric function for PS. However, at least for microporous Si, the pore wall material cannot be considered as bulk Si, and different optical constants should be used.

The experimental refractive index as a function of porosity and current density for two different substrate doping levels is reported in Fig. 27 [161]. It is worth to notice that:

- as the current density is increased, i.e. as the porosity is increased, the refractive index

of the PS layer tends to that of air, in agreement with the simple arguments given above;

- for the same porosity the same refractive index is found. This shows that the Eq. 11 is a good approximation;

- large variations in the refractive index are possible by varying the current density, i. e. the porosity;

- PS formed on heavily doped substrates shows larger refractive index variations than PS formed in lightly doped substrates.

The refractive index is also sensitive to the aging or treatments the PS samples have suffered. In particular, it decreases during oxidation, because of the lower refractive index of Si oxide compared to that of Si. Thus, for application and for device design, it is important to know how the refractive index changes with time, or to avoid oxidation.

E. Luminescence in porous silicon

PS based structures luminesce efficiently in the near infrared (0.8 eV), in the whole visible range and in the near UV [162](Fig. 28). This broad range of emission energies arises from a number of clearly distinct luminescent bands. We can characterize the PS luminescence basically with three different bands:

- the blue band, centered around 2.3 to 2.6 eV (F-band)

- the visible band, centered between 1.4 and 2.2 eV, with a FWHM of $\simeq 0.3$ eV (S-band)

- the IR band, centered typically at 0.8 eV (IR-band)

We follow for the PS luminescence bands, the nomenclature listed in Tab. IV [1].

The properties of the "S-band" have been studied up to now and the S-band has certainly the most technological relevance, since it can be electrically excited. Its main spectral features are summarized in Tab. V.

The S-band can be tuned from close to the bulk silicon bandgap, through the whole visible range. In Fig. 29 the room temperature luminescence spectra of PS samples with different porosities, are shown [163]. It is worth to note that, while the PL efficiency is high under blue or UV excitation, in the range from red to yellow, the emission is rather low [163]. The *S*-band large spectral width is due to the inhomogeneous broadening, and its spectral position depends on the porosity. It is important to note that not only the spectral position, but also the relative intensity of the *S*-band changes with the porosity (Fig. 30) [164]. It was found, that the *S*-band efficiency is not proportional to the inner surface area, but that there exists a "threshold" porosity that has to be exceeded in order to achieve an efficient luminescence [1].

Post-anodization chemical etching in HF, corresponding to a porosity increase, results in a strong rise in the PL efficiency and in a blue shift of the visible band [165]. The external quantum efficiency can be obtained with values higher than 0.1 %,from high porosity PS layers of all types. But the efficiency normally decreases in the order n^-, p^-, n^+, p^+.

2. F-band

The so-called F-band, due to its fast nanosecond decay time, has been subject of several recent studies [166,167]. Some spectral peculiarities of this band are reported in Table VI. This band is observed only in oxidized PS, and it is probably originated from contaminated or defective Si oxide [166].

The IR band presents itself very weak at room temperature and becomes much more stronger at low temperatures [168]. In Fig. 31 it is shown how its peak position scales with the porosity [2]. In addition its intensity seems to decrease in aged samples. The energy of the IR band follows the energy of the S band according to the 1/3 rule (see Fig. 32) [169]. The origin of the IR band seems to be related to dangling bonds.

4. Recombination dynamics

The analysis of the time decay of the visible band gives interesting information. The decay is non-exponential (see Fig. 33 [25]) and is fitted by a stretched exponential function: [170,171]

$$I_{PL}(t) = I_o \exp\left(-\frac{t}{\tau}\right)^{\beta}, \tag{12}$$

where $I_{PL}(t)$ is the luminescence intensity, τ is the luminescence lifetime and $\beta \leq 1$ is a dispersion exponent. This kind of decays is typical of disordered systems and results from a diffusive motion of the excited carriers. [172]

By least square fits of the experimental data, the dependence of τ and β, on a large variety of excitation and sample parameters, has been measured [17]. The temperature dependence of τ has been successfully fitted by the model of an exchange splitted exciton state confined in a quantum dot, [173] where τ is determined by the thermal balance of the occupation between the high-energy dipole-allowed singlet state and the low-energy dipole-prohibited triplet state [2].

The time resolved luminescence results are explained considering that the excitons, before the recombination process, move through the nanocrystals skeleton: the recombination is determined both by the on-site recombination process and by the exciton diffusion [172]. The exciton diffusion is modeled by the trap-controlled hopping mechanism which is based on the existence of both a dispersion of nanocrystal energies and of waiting probabilities for

hopping from one nanocrystal to another. In this way, the nanocrystals with a low hopping probability and energy, act as temporary traps limiting the diffusion [2]. The temperature has a very strong effect on the diffusion. It happens that at low temperatures the role of the temporary traps is very large and leads to a linear increase in β with the temperature, similarly to what happens when the diffusion is due to a multitrapping mechanism [170]. At high temperatures, on the other hand, the temporary traps are thermally emptied and the geometrical arrangement limits the diffusion. In this situation, the diffusion is due to the pure hopping mechanism.

Variations in the porosity, influence the recombination dynamics too. As long as the nanocrystals are isolated, the τ and β parameters are independent on the sample porosity and depend on the observation energy alone, i.e. on the single nanocrystal energy. When the nanocrystals are connected, as in low porosity samples, the role of diffusion increases and the τ and β parameters result to be porosity dependent.

5. Aging effects

Aging effects have an important contribution on the PS luminescence. First of all a blue-shift in the S-band arises from simply storing PS in ambient air at room temperature, as shown in Fig. 34 [143]. However the effect of aging on PS luminescence, seems to be contradictory. Even though blue-shifts are normally observed with aging, PL efficiencies drop in some cases [133] and rise in others [174]. However such effects can be explained in terms of both surface passivation phenomena and carrier confinement [1].

The anodic oxidation can dramatically raise the PL efficiency in medium porosity PS [175] giving an estimated external quantum efficiency (EQE) in the range 1% - 10%, while thermal oxidation at 400-700 °C usually leads to a strong loss of PL efficiency [176]. However, after oxidation at higher temperatures, PS is still luminescent [177]. The quenching of the emission at lower temperature is due to the poor electronic quality of the Si/SiO_2 interface, as evidenced by Electron Spin Resonance (ESR) spectroscopy [177]. It is worth to note that

a clear anticorrelation between the dangling bond density and the luminescence intensity has been measured (Fig. 35) [178], showing that the oxidation can improve the luminescence as a consequence of an increased passivation.

Another important aspect is that the PS luminescence undergoes a significant degradation under normal photoexcitation conditions. What seems is that photothermal, photochemical, photoelectric and photostructural effects are involved in this degradation. The photochemical effects, during illumination in an oxidizing ambient (air), result mainly in a photoenhanced oxidation, which decreases the PL efficiency [179]. This kind of PL degradation is irreversible and can be recovered only partially with an immersion in HF. The photochemical effects can be minimized by illuminating the material under HV atmosphere or in inert atmosphere. Since the PL output is dramatically quenched raising the temperature, it is possible that photothermal effects are important under strong illumination. Finally, there is also evidence of photostructural effects where light generates or removes competing nonradiative centers, affecting PL efficiency [176,180].

III. DIELECTRICS MULTILAYERS

It is well known that when a light beam is reflected by various dielectric interfaces, an effect of multiple interferences occurs. On this simple principle is based the functioning of the dielectric multilayers. A simple scheme of multiple interferences is shown in Fig. 36 [2]. Here a single film is compared with a stack of thin films (multilayer). At each interface between the two materials, with different refractive index, a reflection occurs. In the case of a single layer film the reflected beam is the result of the interference of the two beams reflected at the air-film and film-substrate interfaces. Instead in the case of the multilayer film, the reflected beam is the result of the interference of the multiple beams reflected at each of the different interfaces. By choosing, in an appropriate way, the thicknesses and the values of the refractive indexes of the various layers, it is possible to generate different reflectivity spectra. The final result is the possibility to realize constructive and destructive interferences at different wavelengths. In order to study the case of Bragg reflectors and Fabry-Perot filters, it is worth to see in details the interference in the case of a thin slab.

A. Thin slab

Let us consider first the simple case of two parallel, partially reflecting surfaces, as shown in Fig. 36. Let us define for a thin slab the following quantities: R the reflectance, T the transmittance, I_o the intensity of the primary ray, d the thin slab thickness, θ the angle between any internally reflected ray and the surface normal and n the refractive index of the slab material. We can write the phase difference between two successive reflected rays in the following way:

$$\delta = \frac{4\pi}{\lambda} nd \cos \theta \, , \tag{13}$$

where λ is the vacuum ($\simeq$air) wavelength. The total phase difference between two successive beams, taking into account that for one reflection the phase change δ_r, is equal to

$$\Delta = \delta + \delta_r \tag{14}$$

38

After some calculations we can express the total reflected (I_R) or transmitted intensity (I_T), that results from the multiple interference of the rays:

$$I_T = I_o \frac{T^2}{|1 - Re^{i\Delta}|^2} \quad (15)$$

$$= I_o \frac{T^2}{1 - R^2} \frac{1}{1 + F \sin^2 \frac{\Delta}{2}} \, , \quad (16)$$

The last term is known as the Airy function and an example of this function is shown in Fig. 37 [2]. The quantity

$$F = \frac{4R}{(1 - R)^2} \quad (17)$$

is called the coefficient of finesse and is a measure of the sharpness of the interference fringes.

The condition for a fringe maximum is $\Delta/2 = m\pi$ where m is an integer and is known as the order of interference. It is equal to the equivalent path difference, measured in wavelengths, between two successive beams.

It is possible to extend this formula to the case where the two surfaces of the thin slab are not identical [181].

In absence of absorption $I_R = I_o - I_T$. When absorption is present, instead, $I_R = I_o - (I_A + I_T)$, where I_A is defined as the absorbed intensity.

B. Bragg reflectors

Let us now generalize the case of multiple reflections from a thin slab to the case of a multilayer film [2]. In the following we will use the matrix approach in order to describe the interferences due to the multiple reflected and transmitted beams, that come from the different interfaces present in the structure.

For simplicity, we will consider first the simple case of a single dielectric layer of index n_1 and thickness d inserted between two infinite media with different indexes n_o and n_T. Let the incident light be normal to the surface, the amplitude of the electric field of the incident beam be E_o, that of the reflected beam E_R and that of the transmitted beam E_T. We can write all in a matrix form

$$\begin{bmatrix} 1 \\ n_o \end{bmatrix} + \begin{bmatrix} 1 \\ -n_o \end{bmatrix} \frac{E_R}{E_o} = \begin{bmatrix} \cos kd & \frac{-i}{n_1} \sin kd \\ -in_1 \sin kd & \cos kd \end{bmatrix} \begin{bmatrix} 1 \\ n_T \end{bmatrix} \frac{E_T}{E_o} , \tag{18}$$

where $k = 2\pi n_1/\lambda$. If we introduce the reflection and transmission coefficients, r and t, Eq. 18 is simplified to:

$$\begin{bmatrix} 1 \\ n_o \end{bmatrix} + \begin{bmatrix} 1 \\ -n_o \end{bmatrix} r = M \begin{bmatrix} 1 \\ n_T \end{bmatrix} t , \tag{19}$$

where M is a matrix known as the transfer matrix. This matrix relates the reflected and transmitted beams.

Let us consider now the case of N layers. Each layer with a refractive index n_i and thickness d_i. Using the transfer matrix of each layer M_i we can write the following:

$$\begin{bmatrix} 1 \\ n_o \end{bmatrix} + \begin{bmatrix} 1 \\ -n_o \end{bmatrix} r = M_1 M_2 \cdots M_N \begin{bmatrix} 1 \\ n_T \end{bmatrix} t \tag{20}$$

$$= M \begin{bmatrix} 1 \\ n_T \end{bmatrix} t . \tag{21}$$

By defining the elements of the the overall transfer matrix M

$$M = \begin{bmatrix} A & B \\ C & D \end{bmatrix} , \tag{22}$$

we can solve Eq. 20 for r and t in terms of the following components:

$$r = \frac{An_o + Bn_T n_o - C - Dn_T}{An_o + Bn_T n_o + C + Dn_T} , \tag{23}$$

$$t = \frac{2n_o}{An_o + Bn_T n_o + C + Dn_T} . \tag{24}$$

The reflectance R and transmittance T are then given by $R = |r|^2$ and $T = |t|^2$, respectively. If we want now to obtain a high reflectance multilayer film, we can use a stack of alternate layers of high index, n_H, and low index, n_L. The thickness of each layer has to be equal to 1/4 wavelength. In this case the transfer matrices will be all of the same form and the product of two adjacent ones will be

$$\begin{bmatrix} 0 & -i/n_L \\ -in_L & 0 \end{bmatrix} \begin{bmatrix} 0 & -i/n_H \\ -in_H & 0 \end{bmatrix} = \begin{bmatrix} -n_H/n_L & 0 \\ 0 & -n_L/n_H \end{bmatrix}. \tag{25}$$

If the stack consists of 2N layers then the transfer matrix of the complete multilayer film is

$$M = \begin{bmatrix} (-n_H/n_L)^N & 0 \\ 0 & (-n_L/n_H)^N \end{bmatrix}. \tag{26}$$

If we assume for simplicity that n_o and n_T are both unity, then

$$R = \left[\frac{(n_H/n_L)^{2N} - 1}{(n_H/n_L)^{2N} + 1} \right]^2. \tag{27}$$

For large N the reflectance will approach unity.

This particular stack of $\lambda/4$ layers is called dielectric Bragg mirror or reflector (DBR) and its particularity is to have a high reflectivity, in a given spectral region, centered on the wavelength λ. The reason of this is due to the fact that all the beams, which are reflected by the multiple interfaces, have the same phase when they reach the top interface. Thus they interfere constructively. For other wavelengths the interference is no longer constructive and the reflectivity consequently drops.

It is worth to emphasize the following considerations which follow directly from Eq. 27

1. keeping N fixed, the reflectivity increases as the ratio n_H/n_L increases.

2. keeping n_H/n_L fixed, R increases by increasing N.

Some examples of the reflectance spectra of various DBR obtained by varying respectively N or n_H/n_L, are shown in Fig. 38 and Fig. 39. In these simulations we have considered no absorption, $n_{air}=1$ and $n_T = n_{Si}=4.1$. The spectra are not symmetric around the central wavelength due to the fact that the symmetry is given when the scale is in wavenumber and not in wavelength. Summarizing we can conclude from these simulations that:

1. by increasing N, R increases;

2. by increasing N, the high reflectivity region, also called stop-band, enlarges;

3. by increasing N, the stop-band becomes sharper;

4. by increasing N, the value of R in the stop-band increases with respect to the value of R in the side-lobes;

5. by increasing n_H/n_L the stop-band enlarges and sharpens;

6. by increasing n_H/n_L the overall reflectance value increase, i. e. both in the stop-band and in the side-lobes.

C. Fabry-Perot interference filters

By using two parallel mirrors separated by a spacer, it is possible to construct a particular class of interferometers named Fabry-Perot interference filter (FP) [181]. These filters have a very narrow pass-band and are based on the multiple reflections from two parallel mirrors. It follows that we can apply Eq. 16 and the transmittance of the filter is given by the Airy function (Fig. 37). For $\lambda = mnd$, where n and d are the refractive index and thickness respectively, of the region between the two mirrors, maxima in the transmittance (FP resonances) are observed. The resolution of the filter is given by its finesse F (see Eq. 17). A relation between the width $\Delta\lambda$ of the FP resonance at λ with the FP finesse, exists:

$$\frac{\Delta\lambda}{\lambda} = mF \,, \tag{28}$$

where m is the order of the resonance.

Dielectric multilayers constitute a particular class of FP filters. Dielectric FP usually work at low interference order. The idea is to use two DBR separated by a spacer formed by a dielectric material with a different refractive index of the DBR. In this way the spacer should be λ or $\lambda/2$ thick if one wants to work at the second or at the first interference order (see Eq. 13). In Fig. 40 it is shown a scheme of a FP based on dielectric films [2].

Let H or L be the $\lambda/4$-thick layer of high or low refractive index; then a periodic repetition of HL layers forms the DBR. The structure of a FP could be HL$\cdots$HL-HH-LH$\cdots$LH or

HL$\cdots$ḢL-LL̇-HL$\cdots$HL, where the underlining emphasizes the spacer or central layer $2x\lambda/4$ thick [2].

Some simulations of the reflectance spectra of FP filters are reported in Fig. 41 and 42. Some considerations follow [2]:

1. To obtain a good finesse it is necessary to have DBRs with high reflectivity (large period number or high dielectric mismatch).

2. The finesse is increased by increasing the period number. However by increasing the reflectivity, the transmittance of the FP decreases. A trade-off is necessary between a high finesse and a high transmittance.

3. The transmittance peak is not zero as expected by the theory. This is due to the fact that the structure simulated is not symmetric but asymmetric (on one side there is the air, on the other there is the Si). In order to correct this problem one has to use two DBRs with different reflectivities.

IV. SEMICONDUCTOR MICROCAVITIES

The spontaneous emission rate $R_{sp}(\hbar\omega)$ of a semiconductor is given by the product of the electronic matrix element and the photon mode density; more precisely:

$$R_{sp}(\hbar\omega) = (2\pi/\hbar) \sum_{f,i} |\mathcal{H}_{if}|^2 G(\hbar\omega) P_i (1 - P_f) \delta(E_{fi} - \hbar\omega) \qquad (29)$$

where the sum is over all the initial (i) and (f) final states separated by an energy $\hbar\omega$; $|\mathcal{H}_{if}|^2$ describes the interaction hamiltonian between the initial and final electronic state, $G(\hbar\omega)$ is the photon mode density, and P_i and $(1 - P_f)$ are the probability that the initial state is occupied and the final state is empty, respectively. During the last years a great deal of research work has been performed to modify the emission rate, by reducing the dimensionality of the electronic system (see Fig. 43) [182]. Electrons have been confined in quantum wells, quantum wires and quantum dots. The electronic density of the states has

changed accordingly. As a result, the broad emission features of three dimensional electronic systems, which results from the coupling of two continua of electronic and photonic states, is narrowed, due to the change in the density of the states of the electronic systems. Linewidths as narrow as some μeV have been observed for recombinations in quantum dots.

A different approach proposes to act on the photon mode density (see Fig. 43) by enhancing or inhibiting it. This is an important part of the relatively new field named Cavity Quantum Electrodynamics [183,184]. By decreasing the volume available to the photon modes, i.e. by confining the photons into an optical (micro)cavity (i.e. a quasi-two-dimensional system), or into an optical fiber (one-dimensional systems) or into photon boxes (zero-dimensional systems), sharper and sharper emission features are obtained (see Fig. 43). It is worth to say here, which are the main proposed applications of such structures:

- microlasers (as for example Vertical Cavity Surface Emitting Lasers) [185]

- wavelength tunable Resonant Cavity Light Emitting Diodes (RCLEDs) [186]

- second harmonic generators with enhanced efficiencies [187]

- superradiant Light Emitting Diodes (LEDs) [187]

It is worth to say that photon confinement structures are achieved also via photonic band-gap materials. We will concentrate our attention here only onto microcavities; for an introduction to the former, the reader is referred to Ref. [188]. Light confinement in a planar microcavity is based on the amplitude build-up of the photon mode due to multiple in-phase reflections which occur on localized mirrors [185]. The allowed photon states correspond to the resonances of these Fabry-Perot (FP) like systems. In analogy with the electronic systems, one can consider allowed photon states (the resonances) for which light transmission through the FP is allowed, i. e. photon states exist in the cavity, and inhibited photon states (the wavelength region corresponding to the DBR stop-band) for which light transmission through the FP filter is not allowed and all the light is back-reflected. All this applies to normal-incidence light. For light propagating in the cavity plane, such an argument does not

apply and the photons are free to propagate into the plane. The situation in the intermediate region of incidence angle, is different: the Bragg reflectors behave as ideal mirrors (in the stop band wavelength region) only within a certain incidence-angle range. For a given Bragg reflector it can be defined a "Bragg angle" θ_{Bragg}, which depends on the refractive indexes and thicknesses of the layers composing the mirror, such that, when the angle of incidence θ_{inc} is

$$\theta_{inc} < \theta_{Bragg} \tag{30}$$

the reflectivity approaches the value of 1 and when

$$\theta_{inc} > \theta_{Bragg} \tag{31}$$

it rapidly drops (with weak oscillations) to zero. It has to be said that this picture depends also on the polarization of the incident light. The dependence of the reflectivity of a Bragg reflector on the incidence angle is visualized in Fig. 13 of Ref. [185].

A. Weak coupling mode

When the coupling between the photons and the electronic excitations is weak (for a quantitative description see [185]), it is possible to treat the "photonic" and "electronic" part of Eq. 29, as separate and independent systems.

Let us consider a planar Fabry-Perot cavity with mirror transmittivity T and reflectivity R; the mirrors are spaced d apart leading to a vertically propagating mode with wavelength $\lambda = nd$. The mode amplitude in the cavity region is 4/(1-R), while that of perpendicular non-resonant mode (at different λ) is suppressed by a factor (1-R) [189]. The same happens, when one considers modes at a given wavelength but at different angle ϕ, for which the resonant mode wavelength would be $\lambda_c(\cos\phi)^{-1}$. The same suppression factor (1-R) would be obtained for non resonant modes, i. e. at angles different from the normal. The unique feature of microcavities is therefore, to concentrate the field intensity into the resonant mode as much as it is suppressed in other modes, with a more or less constant lifetime.

The factor of merit describing the control of spontaneous emission into a desired mode, is called the spontaneous emission factor β:

$$\beta = \frac{\text{spontaneous emission in the desired mode}}{\text{spontaneous emission in all the modes}} \tag{32}$$

To bring β to unity, one has to deal with the recombination into the other competing modes (see Fig. 44) [189]:

- into leaky waveguide modes of the DBR: the Bragg mirrors are efficient up to a critical angle $\theta_{Bragg} = (n_2 - n_1)/n$, where n_1, n_2 and n are the refractive indices of the two materials and their average, respectively. Beyond θ_{Bragg}, the Bragg mirror acts as an homogeneous dielectric medium with average index n as already said above.

- into guided modes, which are particularly important when the spacer layer has a higher refractive index than the average of the DBR.

- into oblique modes, whenever the emission spectrum is broader than the cavity linewidth. Emissions into modes at wavelength different than the cavity wavelength, are redistributed into cones of monochromatic light. In this way, even if the emission spectrum is narrow, the β factor is reduced because of a not-perfect coupling into the cavity mode.

Multiple reflections in a microcavity, select an escape cone which is much smaller that the angle 2π of a Lambertian source. This builds up the light emission in a given direction, leading to directionality. Another useful effect is that of spectral narrowing due to the spectral width of the allowed mode.

B. Strong coupling mode

The modification of the spontaneous emission rate, due to the above mentioned weak coupling between photons and electronic excitations, is not the only effect of the photon confinement. In fact, if the coupling between the electronic excitation and the photon mode

is strong enough, a resonant transfer of excitation between the two states (Rabi oscillations) settles in and dominates on the weak coupling. A great deal of work, both experimental and theoretical, has been devoted to describe and realize the strong coupling case in particular for the possibility of exploiting it in novel, enhanced-performances, non-linear optical devices. However a review of this is far beyond the aim of the present paper. The interested reader is referred to Ref. [190].

V. POROUS SILICON MULTILAYERS

The ideas discussed up to now for the dielectric microcavities, can be applied also to porous silicon; in this way PSM are obtained.

When the wavelength of the incident light is much larger than the typical nano-crystal size, it is possible to use the effective medium approximation in modeling the dielectric response of PS. A problem is the choice of the appropriate effective medium, i.e. of the mean between the various components which form PS. A valid approximation for spherical particles, is the Maxwell-Garnett approximation, which yields to an effective dielectric constant ε_{eff} [157]

$$\frac{\varepsilon_{eff} - \varepsilon_M}{\varepsilon_{eff} + 2\varepsilon_M} = f\frac{\varepsilon - \varepsilon_M}{\varepsilon + 2\varepsilon_M} \; , \tag{33}$$

where f is a free parameter describing the volumetric fraction, ε is the dielectric function of the spherical particles (silicon) and ε_M is the dielectric function of the embedding medium (the air). An extension of this approximation is given by the symmetric expression of Bruggeman equation [157]

$$f\frac{\varepsilon - \varepsilon_{eff}}{\varepsilon + 2\varepsilon_{eff}} + (1 - f)\frac{\varepsilon_M - \varepsilon_{eff}}{\varepsilon_M + 2\varepsilon_{eff}} = 0 \; . \tag{34}$$

From Eq. 34 and by assuming that $\varepsilon_M \simeq 1$, $n_{eff}^2 \simeq \varepsilon_{eff}$, i.e. the PS film would have a negligible absorption coefficient (at the considered wavelength), one can obtain the volumetric fraction f

$$f = \frac{\left(1 - n_{eff}^2\right)\left(n^2 + n_{eff}^2\right)}{3n_{eff}^2\left(1 - n^2\right)} \, . \tag{35}$$

In Fig. 45 a comparison of the porosity deduced by a gravimetric method, with that deduced by this formula, where n is experimentally determined, is shown. The linear fit has a slope of 1.1 ± 0.1 and an intercept of 0 ± 5.

The main technique to measure the refractive index of PS, is the use of spectroscopical ellipsometry [191]. However for the multilayered samples, the etching parameter dependence of the refractive index has been widely deduced by the measurement of the reflectivity of the samples. One approach, mainly used by Theiss and coworkers [157], is based on the least square fit of the reflectance spectrum with a model of the dielectric function, such as that of Eq. 35. Another approach, used by us, relays on the measurements of the interference fringes from the multilayered PS structure under study. This method has the advantage of being fast and easy. In Fig. 46 it is shown the normal incidence reflectance spectrum of a p^+-type doped silicon wafers and the deduced refractive index, where

$$n_{Si} = \frac{1 + \sqrt{R}}{1 - \sqrt{R}} \, . \tag{36}$$

In Fig. 47 the reflectance spectrum of a 75 % porosity PS film, 6.8 μm thick, is reported. The spectrum is characterized by the multiple interference fringes caused by the air-PS and PS-Si interfaces. By assuming that the PS film has parallel surfaces and that the refractive index is a smooth function of the wavelength, it is possible to deduce from the wavelength position of adjacent reflectance maxima or minima the value of the refractive index: [181]

$$2nd\left(\frac{1}{\lambda_r} - \frac{1}{\lambda_{r+1}}\right) = 0 \, , \tag{37}$$

where d is the porous layer thickness and λ_r the wavelength of the r-th reflectance maximum/minimum. By solving for n,

$$n = \frac{1}{2d}\left(\frac{1}{\lambda_r} - \frac{1}{\lambda_{r+1}}\right)^{-1} \, . \tag{38}$$

An error of 5%, on the refractive index so determined, can be roughly estimated. This procedure has been followed for various porosities and the results are reported in Fig. 48.

It is observed that the n values are lower than those of Si and that increasing the porosity, n decreases; this is comprehensible, because when the porosity increases it means that the percentage of voids in the PS structure increases and the the total refractive index, which will have an intermediate value between Si and air, will approximate even more its value to that of air (roughly 1).

A. Producing porous silicon multilayers

Two main ways of producing PS multilayers have been proposed up to now [192]: by periodically varying the etching parameters, such as for example the current density or the light power on the surface of Si under etch, or by using periodically doped substrates and maintaining constant the various etching parameters. In the following we will discuss the first approach, because it is more easily accomplished and it has been the one employed by us [19,187,193–195].

This approach is based onto the following statements:

- the etching process is self-limited (once a porous layer is formed, the electro-chemical etching of this layer stops);

- the etching occurs mainly in correspondence of the pore tips;

- the porosity depends only on the current density once the other etching parameters are kept fixed;

- the refractive index of PS, n, depends on its porosity;

Hence, by varying the current density during the etch process, it is possible to vary the porosity in the etching direction only at the etch front (Fig. 49 [196]). In this way, the current versus time profile is transferred in the porosity versus depth profile, i.e. n, versus depth profile (see Fig. 50).

The choice of the substrate doping and of the HF concentration, has to be carefully made in order to obtain the maximum variations of the porosity, i.e. of n, within a given range

of current density. Various substrate dopings have been used and variations of porosities ranged between 25 to 75 % for 0.01 Ωcm, and between 55 and 75 % for 0.2 Ωcm [194]. For porosities higher than 75 % it was observed a "peeling off" of the porous silicon layer. In Fig. 51 the effective refractive index, measured by ellipsometry as a function of the current density for two substrate doping is shown [197]. Larger variations in n, for the heavily doped substrates, were measured. In Fig. 52 and 53, the porosity vs. current density and etch rate vs. current density are shown for p-type doped substrates (0.01 Ωcm) and for three different HF concentrations ([HF]): 10 %, 15 % and 20 % [19,198]. Some comments are worth to be done :

- the porosity is a linear function of the current density, for a given [HF], in a restricted interval of current densities;

- increasing the [HF] and for a fixed current density, the porosity of the resulting layer is decreased;

- the relatively larger porosity variation is obtained for [HF]=15 %, by varying the current. Indeed porosities between 42 and 83 % were obtained by increasing the current density between 1 and 200 mA/cm^2. For similar current variations, the porosity changed only between 71 and 87 % for [HF]=10 %, and between 45 and 70 % for [HF]=20 %;

- the etch rate is a linear function of the current densities;

- the etch rate slightly depends on [HF].

The refractive index and etching rate values obtained for a single layer, are modified in presence of a multi-layer structure. Some explanations of this have been proposed in the literature: current focusing and defocusing [199] or porosity gradients at the interface [194]. To solve this problem, n and the etch rate, V, of a given porosity film in presence of a multilayer structure, could be measured by growing Fabry-Perot filters and looking at

the angle dependence of the wavelength of the transmittance maximum λ_c, that is given by [181]:

$$\lambda_c = 2 n_c d_c \left[1 - \left(\frac{\sin \phi}{n_c} \right)^2 \right]^{1/2} , \qquad (39)$$

where n_c and d_c refer to the central layer, and ϕ is the angle with respect to the normal to the surface of the sample. From least square fits of the experimental data with Eq. 39, both $n_c \times d_c$ and n_c can be determined separately and, hence, by knowing the etching time, it is possible to obtain the V. Such an experiment has been performed and it was found that the n_c and V values are systematically lower than the values determined for a thick film of the same porosity, i.e. obtained with the same current [198]. For example for a 53 % porosity layer on a 0.01 Ωcm substrate, it was measured n=1.64 at 714 nm and V=0.018 μm/sec while for a thick film n=1.95 at 714 nm and V= 0.021 μm/sec. These results, i.e. lower n and V in multilayers than in thick monolayer samples, have been systematically observed. However the characterization of several different porosity films by using this method is very time consuming and what is important for the modeling of FP and DBR is the product $n_c \times d_c$. Consequently, one can use n_c as determined on thick samples and modify V, according to the results of FP resonance wavelength measurements at normal incidence, where $\lambda_c = 2 \times n_c \times d_c$. The results of such determination are given in table VII.

At a first glance, PS multilayers are different from PS single layers due to their bright and colourful appearance. In addition, quantitative reflectance measurements show very high values of the reflectance maxima and narrow FP resonances [198].

More detailed characterization of the interfaces have been carried out with Transmission Electron Microscopy (TEM). In Fig. 54 a TEM image of a PS multilayer is shown [194]. The low porosity layers appear darker in the image due to the high density of the material. The interfaces between layers of different porosity are sharp on a nanometric scale. Moreover, the lateral roughness on the scale of several hundred nanometers is very low for the top most interface and increases slowly with the depth. This roughness is expected to be due to the inhomogeneity in the substrate and accumulates more and more during the propagation of

the etching front [196]. Indeed it is absent in epitaxial layers which have a higher crystalline quality [200].

Gravimetric measurements on single layer and porosity multilayer are often in disagreement, revealing a lower mean porosity in the multilayer structures than in the single layer structures [194]. This is thought to be due to porosity gradients. The porosity gradient at the interface might be due to recharging effects of capacities in the etching cell [194]. In Fig. 55 the experimental diffraction pattern of a 10 period PS multilayer is showed [86]. As can be seen a number of satellite peaks are detected revealing high quality multilayer structures. No progressive broadening of the satellite peaks is observed which indicates a good lateral stability of the mean period. Some observed splitting on the large-angle side of the satellite peak reflects some slight variation in the depth of the multilayer period. The satellite intensity also decreases with higher satellite order due to graduated interfaces whose comes from the porosity gradient mentioned above.

It was demonstrated that a variation of the sample resistivity can lead to a porosity variations [201]. Hence, a periodic modulation in depth of the dopant concentration in a Si wafer causes a periodic variation in the porosity once PS has been etched. In Ref. [192,194,202] this kind of approach has been accomplished. By CVD, 10 and 5 periods of 75 nm (150nm) thick p-type doped silicon layers at levels of free carrier concentration of 1×10^{17} cm^{-3} (1×10^{19} cm^{-3}) were grown. The etching has been carried out in the dark with a constant current density of 50 mAcm^{-2}. Some very sharp interfaces were observed (see Fig. 56 [202]) with a three layers structure due to the anisotropy of the etch caused by the etching selectivity on the doping level [200].

B. Bragg reflectors

Some examples of reflectivity curves for PS-based distributed Bragg reflectors are reported in Figs. 57 and 58. The effect of the variation of λ_c, the central wavelength of the DBR, is shown in Fig. 57 [198]. The reflectance maximum increases from 0.8 to 0.95-0.97

when increasing λ. The best results are reached for DBR centered at long wavelengths (i.e. in the near infrared). This is due to an increased absorbance of the PS layers at shorter wavelength (i.e. lower than 550/600 nm), effect which was not taken into account in the first modelization of the structure. The width of the high reflectance region (namely stop-band region) is determined by the refractive index difference between the high refractive index (n_H) layer (H) and the low refractive index (n_L) layer (L). Higher is the difference and larger is the width. An example is also shown in Fig. 57 where the ratio at λ of the refractive indexes changes from 1.19 (d) to 1.27 (b) and to 1.52 (a). In agreement with the theory, also the value of the reflectance in the stop band increases as the refractive indexes ratio increases [181].

The number of periodic repetitions of the LH (where as usual L stays for low refractive index layer and H for high refractive index layer) stacks in the DBR should be optimized with respect to the beneficial effect of an increased reflectance, for a large number of repetitions, and the detrimental effects of a depth inhomogeneity in the porosity for the first layers due to the effect of a long residence in the electrolyte [193]. This is clearly shown in Fig. 58 where only the repetition number of periods is changed. The maximum reflectivity is increasing from 0.8 for 5 periods (a) to 0.93 for 8 periods (b), to 0.97 for 15 periods (c) to 0.95 for 30 periods (d). A good compromise is reached for a number of repetitions of about 15. Also the reflectance of the side-bands decreases increasing the number of periods in agreement with the theoretical expectation value [181].

In Fig. 59 the reflectance of several oxidized DBR over the visible range is shown [197]. No absorption effect is measured (in the sense that the reflectivity maximum is the same for all the layers). This is due to the use of a complete oxidation of all the PS layers, which diminishes the absorption in the visible. Oxidation is accomplished after a 5 min thermal processing (namely RTO or Rapid-Thermal-Oxidation) at 950° C. The stop-band is narrower and the reflectivity maxima are lower than in not-oxidized samples because of the lower refractive index of SiO_2 (the oxides that forms in the RTO process) with respect to that of Si which decreases the absolute value of the ratio n_H/n_L.

C. Random Bragg reflectors

Crystalline disorder modifies the band structure of the electronic systems. In particular, amorphous Si has a wider energy gap than crystalline Si. By considering the analogy between electronic states and photon modes, one can -for analogy- expect that a randomization of the DBR structure (in the sense of its internal periodical order) will modify its reflectance spectrum. Random Bragg reflectors have been obtained in Ref. [3] by keeping constant the thickness (d_L) and the porosity of the L layers and by changing the thicknesses (d_H^I) but not the porosity of the H layers. The various d_H^I were generated randomly such that their histogram tends for large numbers to a gaussian distribution centered around a mean value $\langle d_H \rangle$ and with a standard deviation σ. Clearly $\langle d_H \rangle \times n_H = d_L \times n_L = \lambda/4$

In Fig. 60, the effect of an increasing σ on the reflectance spectra of random DBR centered at the same $\lambda = 800$ nm is reported. For $\sigma = 0$, the typical reflectance of a DBR is observed. The stop-band is 200 nm wide and the maximum reflectivity is $\simeq 95$ %. The effect of increasing σ is to broaden the stop-band without a diminution of the absolute value of the reflectivity. For $\sigma = 30$ nm the stop-band starts at about 650 nm and extends to more than 900 nm, the upper limit of the detection of the experimental set-up used.

In Fig. 61, the influence on the reflectance spectra of the d_H^I distribution in the actual sequence used in forming the DBR is reported [3]. All the samples have the same layer sequence. The top panel reports the spectra when the layer thicknesses are randomly settled. The second and third panels refer to the case of an ordered sequence of the layer thicknesses: the second to the case of an increasing ordering (the thinnest layer is the first near to the air side) and the third to the decreasing ordering (the thickest one is the first on the air side). These three Bragg reflectors are centered at the same $\lambda = 570$ nm, i.e the gaussian distribution of the H thickness is centered at $\langle d_H \rangle = 63.8$ nm and with $\sigma = 21$ nm, and has the same random distribution. The principle of operation of a $\lambda/4$ stack is such that a period HL corresponds to $m \times \pi$ phase-difference between rays reflected by neighbour layers, where m is an integer. The presence of different thicknesses enlarges the λ values for

which constructive interference occurs (stop-band). This explains the effect of the ordering. However when a thin layer, which yields to a constructive interference condition for short wavelengths, occurs at the end of the sequence, i.e. some 10 μm away from the surface, most of the light of that wavelength has been already absorbed by the other layers. This explains why, in order to observe reflection at short wavelengths in random DBR, the thinnest layers has to be placed at the air side.

The last two reflectance spectra in Fig. 61 refer to the following HL ordering: the fourth panel refers to the following sequence air-HLHL...($\times$20)...HLHL-substrate, while the bottom panel to air-LHLH...($\times$20)...LHLH-substrate. The stop-band is almost equal in the two cases, while the reflectance maximum is higher when a high refractive index layer faces directly the air than when the low refractive index layer is used: 95 to 93 %. This could be explained by the larger refractive index mismatch at the air side in the first case than in the second.

Fig. 62 shows the effect of increasing the number of periods in the DBR [3]. Even with 10 random layers, i. e. 10 HL periods, a good disorder description is reached (compare with the reflectance of the periodic DBR shown in Fig. 60 top spectrum). Moreover by increasing the number of layers the random distribution better approximate a Gaussian (i.e. is "more random") and the stop-band broadens. The maximum number of periods used was 30 layers. The reflectance of the corresponding DBR is shown in the bottom panel of Fig. 62. A degradation of the characteristics of this DBR is observed with a lower reflectance maximum and the appearance of reflectance minima in the stop-band. This last effect has been already observed for "normal" Bragg reflectors and discussed before.

It is worth to observe that the properties of the random DBR are not very dependent on the actual distribution of the thicknesses used. In fact, as can be observed in the second and third panel in Fig. 62, the use of two different choices of random thicknesses does not change the reflectance spectrum. Only some minor differences can be observed and explained by the particular thicknesses used in the DBR growth. For example the DBR whose reflectivity is reported in the second panel, has a lower number of thin layers than the DBR whose

reflectivity is reported in the third panel. Hence, the reflectance of the first DBR shows a stop band which starts at longer wavelength than the one of the second DBR.

D. Fabry-Perot Filters

Some examples of PS-FP filters are reported in Fig. 63 [198]. These are constituted by a $\lambda/2$ thick central layer sandwiched between two equal DBR with 6 or 8 repetitions of the $\lambda/4$ thick LH stacks: the structure is the same as in the case of the microcavity. The only difference is the porosity of the central layer; in the PS-FP it is the same of one of the layers employed to grow the Bragg reflectors while in the PSM the central layer has a porosity (and then a refractive index) different from both the porosities of the alternated layers constituting the DBR. Decreasing the number of repetitions from 8 to 6 does not influence markedly the reflectance of the stop bands while it increases the transmittance in the FP mode (see table VIII).

The filtering effect of these FP filters on the emission band of PS has been demonstrated and is shown in Fig. 64 [198]. A comparison between the room-temperature photoluminescence spectra of a 5 μm thick 75 % porosity PS sample and those of samples constituted by a FP filter on top of a thick (few μm) 75 % porosity PS layer, has been performed. The wide emission band of PS is strongly narrowed by the action of the FP filter. In addition, by tuning the FP wavelength λ it is possible to select the emission wavelength of the structure. This is the basis for the subsequent work on the PSM.

E. Random-Fabry-Perot filters

In Fig. 65, the effects of the use of random DBR in the above described FP structure is shown [3]. These filters have the following sequence: air-LH...($\times$6)...LH-$\underline{S}$-HL...($\times$6)...HL-substrate, where $\underline{S}$ is the central layer of thickness λ. The distribution of the random layers in the two DBR is symmetric around the $\underline{S}$ layer. The various spectra

correspond to various levels of randomness governed by the standard deviation of the gaussian distribution σ of thicknesses already described. The top reflectance shows the typical characteristic shape of a FP filter. The effect of the use of random DBR is to slightly decrease the transmittivity at the wavelength of the FP mode which passes from 46 % to 44 % for the random FP, while the stop band increases from 184 to 192 nm in the random FP, but such small effects could be also attributed to uncontrolled variations in the production parameters.

In Fig. 66, the luminescence spectra of various random FP are reported [3]. By measuring the luminescence one measures principally the transmittivity of the FP filter [203]. The top panel in Fig. 66 is shown to demonstrate the relative insensitivity to the actual set of random numbers used for the random FP properties. The central panel shows the effect of the increasing of σ on the luminescence linewidth around the FP resonance, which is an indication of the finesse of the FP. The linewidth decreases significantly by increasing the degree of randomness into the DBR. In addition the baseline is also reduced and this fact points to a slightly large reflectance for the random DBR. The bottom panel compares different random FP obtained with increasing the number of the periods. It has been found that the linewidth is reduced from 25 nm for 4 periods down to 2 nm for 10 periods.

The record linewidth is shown in Fig. 67 [3]. A photoluminescence linewidth value as narrow as 2 nm can be measured. This should be compared to 130 nm, typical linewidth of luminescence band of PS of similar characteristics than those measured here. For this random FP a finesse as high as 200 is obtained. Note also the nearly complete absence of luminescence for wavelengths different than the resonant wavelength.

A different approach to the random FP filters is that one of the Rugate filters [197]. Rugate filters are obtained by a continuous variation of the refractive index with the depth and allow to obtain reflectance profile with very low sidebands. A sinusoidal profile of the refractive index is usually employed [204]. A careful characterization of the n vs. J relationship is clearly necessary. In this way it is then possible to modulate the refractive index value in depth in the way shown in Fig. 68(a). As a result, the reflectance shown in

Fig. 68(b) is obtained. As expected, the side bands are practically absent.

VI. POROUS SILICON MICROCAVITIES

A planar optical microcavity can be realized by using a FP structure surrounding the central PS layer. In this way an all PS microcavity (PSM) is obtained. The top and bottom DBR act as photon confiners while the central layer (also named the spacer) acts as the optically active medium. It is in this layer where the coupling of the excitonic transitions with the photon modes should be modified (inhibited or enhanced). It is worth to underline an important difference between III-V microcavities like those reviewed in [185] and PSM: the first have the emission line of the active layer in itself (without the cavity effects) that is narrower than the FP transmission peak while in the case of PSM the emission of "bulk" PS is much wider than the reflectivity FP dip. This point makes more interesting the PSM because they allow to test a new situation in the field of microcavities.

PSM are different for some fundamental aspects from similar optical microcavities realized with GaAs/AlGaAs multilayers [185]. In fact, in PSM

- the coupling between the photon and the exciton mode is weak mainly due to the very broad emission band of PS and to the fact that the DBRs do not confine perfectly the light but they are partially penetrated by the confined photon mode

- the emission takes place in the whole central layer

- the emission band of PS is wider than the stop band of the DBR, and

- the emission of the central PS layer and of the PS-based DBR overlap spectrally.

In the literature two different kinds of PSM have been reported. One is based on the use of PS to fabricate the whole PSM [187,205]. The other uses a mixed approach: the bottom mirror is a PS-DBR while the top mirror is a thin metal (as for example gold) layer [206]. In the following, we will review mainly the properties of all PS microcavities.

The Fig. 69 [199] shows the room-temperature PL spectra of a PSM with the resonance at λ_c (solid line), of a λ_c-thick PS 75% porosity reference layer (dotted line) and of a reference DBR composed by 12 periods of alternating 62% and 45% porosity layers (dashed line) [199]. The emission was collected around a the direction normal to the sample surface. The influence of the change in the photon mode density on the spontaneous emission spectrum can be appreciated by comparing the lineshape of the PSM with that of the reference PS. For $\lambda \simeq \lambda_c \simeq 750$ nm a sharp peak is observed which is 14-times more intense than the luminescence (this value can arrive up to 20) at the same λ_c, for the reference sample. For $\lambda \neq 750$ nm but within the stop-band of the DBR, the luminescence of the PSM is roughly the same as that of the reference mirror. For $\lambda \simeq 900$ nm a secondary peak is observed due to the escape of a leaky waveguide mode confined in the waveguide-like structure formed in the plane between the mirrors of the microcavity [207]. These leaky waveguide modes can be strongly enhanced by a suitable choice of the PSM parameters (see e.g. Fig. 64). The overall integrated emission intensity of the PSM is increased by a factor of 4 with respect to that of the reference. The microcavity has an important role in this former intensity increase but another beneficial effect is expected by the top Bragg reflector which acts as a protective layer for the active optical layer. A reduction of the surface recombination velocity and of the effect of atmosphere impregnation can be expected. In addition, by simply choosing the appropriate width of the PSM active layer and DBR it is possible to select the emission wavelength of the PSM taking advantage of the broad spectral emission of the PS active layer (see Fig. 64). For what concerns the PL of the DBR (dashed line), although it is centered on the same spectral region as the standard PS λ-thick layer (dotted line), it can not give rise to both the narrowing and enhancement observed for the PSM emission. The shape of the PL of the DBR is linked to the stop-band reflectivity spectrum that rules the reflectivity properties of the reflector itself [2].

An important aspect of the optical emission stands on the possibility of controlling the

radiation pattern and obtaining a strong angular confinement of the output emission. In the case of the semiconductor microcavities, this is a well-known result due to the anisotropic density of photon states controlling the emission radiative decay [185,208].

In addition, the emission at angles far from the normal, experiences a further decrease in the coupling between the excitons and the cavity mode due to the shift of the cavity-mode resonance wavelength [209].

This effect is observed in the dependence of the PL intensity as a function of the emission angle ϕ (see the definition in Fig. 70) [199]. These results are shown in Figs. 71 and 72. In Fig. 71, two main effects can be observed [2]:

- the shift of the resonance peak with ϕ (see Eq. 39).

- the decrease of its intensity.

This is well quantified in Fig. 72 where the ϕ-dependence of the resonance peak intensity is reported [199]. A very similar result is obtained if one plots the total PL intensity as a function of ϕ. As a result, the emission intensity of the PSM is concentrated in a cone of about 30 degrees around the normal. The effect observed in Fig. 72 is due to the anisotropic photon mode density due to the confinement into the microcavity.

In Fig. 73, the PL emission spectra at 30 K and at room temperature for both a λ (solid lines) and a $\lambda/2$ (dotted lines) microcavity are shown [203]. The inset shows the temperature dependence of the normalized integrated emission intensity of both microcavities and, as a reference, that corresponding to the PS λ-thick layer. A small red-shift (few meV) of the PL peak is observed as the temperature increases owing to variations in the refractive indexes and layer thickness. No significant dependence of the FWHM on the temperature can be revealed confirming that the linewidth is determined only by the microcavity finesse. The stronger emission of the λ-PSM is related to the larger active layer thickness although the normalized integrated emissions of the two microcavities become equal increasing the temperature, as the hopping-mediated and thermally activated non-radiative processes [17] compensate the thicker active layer of the λ-cavity.

Microcavity effects are also revealed by the temperature dependence of the integrated PL intensity (inset of Fig. 73). A sensibly different behaviour between PS and PSM is observed. In the reference sample, like in the usual PS samples [210], the integrated PL emission behaviour is explained with the help of concurrent measurements of the PL lifetime and it is thought to be the result of two opposite processes [173]: the thermally activated promotion of excitons from the low-energy dipole-prohibited exciton triplet state to the high-energy dipole-allowed exciton singlet state, which increases the PL intensity and dominates at low temperatures, and the thermally activated non-radiative recombination, which decreases the PL intensity and dominates at higher temperatures. These trends are strongly modified by the presence of the cavity embedding the PS. The temperature dependence of the PL intensity of PSM has been investigated in detail in [211] and will be presented in more detail in Sec. VI E, where a temptative explanation of the observed effects will be proposed.

The results presented so far have been obtained with PSM formed on heavily doped substrates. However, low doped substrates yield to PS with higher luminescence efficiency. Thus it is interesting to know whether the improvement in the spontaneous emission properties are found also on PSM formed on low doped substrates. This work has been performed in Ref. [205,212]. That characterization has shown that in the case of p^- substrates (6 to 9 Ω cm typically) the etching rate is in general slower (3 to 35 nm/s) and it is very hard to get low porosity values. Using a solution of 20% HF in water and ethanol it was possible to obtain porosities in the range 60 − 85 %, which correspond to refractive index values between 1.7 and 1.3 at 750 nm (see Fig. 27 [212]).

As already remarked previously, working with multilayers instead of single layers, has an important advantage on the mechanical stability. It is extremely difficult to obtain high porosity layers (the most luminescent) of considerable thickness. Alternating low and high porosity layers allows to produce thick multilayers making the whole structure more robust, while the emission efficiency is not reduced, and can be, on the contrary, furthermore improved by careful design of the cavity [2]. This is even more important for p^- doped substrates, where the highest porosity single layers do not have the necessary mechanical

stability to ássure the high optical quality required for reliable and precise measurements. In multilayer structures these highly porous layers are sandwiched between layers of lower porosity, and their optical properties turn out to be more homogeneous and reproducibile. Nevertheless, the drying process, which is a very important step for obtaining porosity layers, showed to be critical also for multilayers structures. For what concerns their performances, PSM have been obtained with linewidth of 6 nm [212], finesse up to 66, external quantum efficiency of about 15 % and luminescence enhancement of $\simeq$ 20 [205].

B. Aging effects in porous silicon microcavities

Aging effects in PSM are related to the changes in PS itself. They involve variations in the luminescence intensity and variations caused by changes in the refractive index. Both effects are closely related to oxidation.

For what concerns PS, the oxidation increases the luminescence quantum efficiency. The large increase in the emission intensity is accompanied by a blueshift of the maximum of the broad emission band. For this reason, it is interesting to know how this enhancement of the emission intensity depends on the time and to what extent it is preserved in the case of PSM.

In order to understand the role played by the single optical parameters in the time evolution of PSM, the variation of the refractive index has been investigated for some reference layers over a period of six months. These variations are reported in Fig. 27 [212]. It should be noted that for every value of the anodization current density (that is, for every value of the porosity) the value of the refractive index decreases with time. This is not so surprising, because after the partial oxidation, PS is no longer a mixture of air and silicon, but a mixture of air, silicon and silicon dioxide, and the refractive index of silicon dioxide, about 1.46 in the red region of the spectrum, is much lower than that of silicon. The oxidation process itself seems to be more efficient in the high porosity layers, because of the larger internal surface and the lower content of silicon. As a consequence, the relative variation of

the refractive index is larger for the higher porosity layers. All these properties of PS single layers are extremely important to understand the evolution of the properties of PSM optical properties with time.

The changes in the photoluminescence intensity and lineshape for a typical p^- PSM over a period of six months are reported in Fig. 74. It is worth to notice how the whole structure of the cavity is not degraded, but simply shifted towards the higher energies, while the emission intensity increases of about one order of magnitude. The conservation of the cavity structure is even more apparent if we compare the reflectivity spectrum of the freshly etched PSM with the spectrum measured after six months [212]. Both spectra are reported in Fig. 75. The central dip coincides with λ_c, and it undergoes to a relevant blue-shift. The maximum of the reflectivity is lowered only of a few points per cent, while the whole stop-band shifts of about 50 nm, retaining its own features. The observed blue-shift is caused by the refractive index changes in the PS layers of both the central cavity and the mirrors. As the value of n_c lowers with time, λ_c moves towards higher energies, as reported in Fig. 75, but maintains its central position within the stop-band of the PSM, because also the mirrors oxidize [212]. The stop-band of the mirrors shifts to higher energies because the refractive indexes of the PS layers decrease.

Since all the refractive indexes lower with time, approaching the value of 1, one can expect the stop-band to become narrower and narrower as the PSM ages. However, this fact has not been observed. As we have shown previously in Fig. 27, the lower the refractive index, the larger is the relative change with the aging.

Nevertheless, the whole process is not ideal, and the degradation in the quality of the PSM is then observed [212]. As can be seen in Fig. 74, the enhancement of the emission intensity is accompanied by a slow decrease of the ratio central wavelength luminescence/background emission, and by an increase of the intensity of the side bands. This slow degradation affects the $\Delta\lambda$ of the central peak, which enlarges slightly with time. In Fig. 76, we compare the photoluminescence of a freshly prepared and an aged PSM with that of a reference layer of the same thickness and porosity of the cavity layer, which aged in the

same way as the PSM. The relative enhancement in the emission remains roughly the same, while the whole increase of the photoluminescence intensity due to the aging is more than one order of magnitude, and occurs both for PS and PSM.

We performed also simulations in order to get some insight on the aging process mechanism. We found that while the blue-shift in the whole structure of the cavity is basically due to the variation of the refractive indexes, the degradation in the quality of the PSM is not due to the oxidation process itself, but to the fact that this process is not homogeneous in depth. A homogeneous oxidation does not degrade the cavity, but, on the contrary, improves its optical properties because of the difference in the refractive indexes increases with the oxidation. The slow degradation in the reflectance properties and the slight increase in $\Delta\lambda_c$ can be reproduced assuming a variation of refractive indexes in depth, as reported in Fig. 75 [212]. The layers which face the surface, oxidize before than the other layers. As observed for random PSM [3], the progressive oxidation is important to maintain the coherence between the multiple reflections at the various interfaces. This fact explains the relatively good performances of aged PSM. To confirm this idea we measured the cavity blue-shifts for PSM aged in the same way but with different number of periods in the mirrors. We found that after six months the relative blue-shift is 7.3 % with 6 periods, 7.1 % with 8 periods and 3.0 % with 10 periods. This values are always lower than those estimated using the values of refractive index for freshly etched and aged PS (10.5 %, see Fig. 75) [212]. Due to the very high specific internal surface of PS, the layers forming the microcavity undergo a process dependent on the time of storing in air atmosphere, which results in the formation of a native oxide layer on the inner pore surface. This in turn could change the refractive index of PS and, consequently, the reflectance spectrum of the PS multilayer.

A comparison between "as-prepared" and oxidized PS multilayers has been performed in Ref. [200]. FP filters were formed on 0.2 Ωcm p doped wafers. The oxidation was performed in dry O_2 at 300° C for different times.

A key role in the aging is finally played by the substrate resistivity. p^+ doped samples, as those shown in Fig. 63 [198], presented a shift of only some nm after one year aging.

To clarify the optical behaviour of the PSM, the reflectivity and absorption spectra were calculated in Ref. [203,213] using a transfer-matrix approach (see Section III B) and assuming the exciton quantum confinement in Si-nanocrystals [172]. The first step is the evaluation of the first order susceptibility given by:

$$\chi(\omega) = \int_0^\infty P(\omega_o)\overline{\chi}(\omega,\omega_o)d\omega_o \ , \tag{40}$$

where $P(\omega_o)$ is the distribution of oscillators (excitons) as a function of frequency. The susceptibility of a single exciton $\overline{\chi}(\omega,\omega_o)$, is given by:

$$\overline{\chi}(\omega,\omega_o) = \frac{f\omega_o^2}{\omega_o^2 - \omega^2 - i\Gamma\omega} \ , \tag{41}$$

where f is the oscillator strength and Γ the thermal broadening factor that is assumed to depend linearly on the temperature.

A gaussian size distribution for the Si-nanocrystals centered at $d_c = 34.6$ Å and having a width $\sigma_d = 1.3$ Å has been considered [172]. The emission energy E_i is then related to the corresponding size d_i through the power-law relation $E_i = E_c(d_c/d_i)^n$ with $n \approx 1.4$ [214], where E_c is the transition energy corresponding to a Si-nanocrystal of size d_c. Within these assumptions $P(\omega_o)$ is given by:

$$P(\omega_o) \propto \frac{1}{\sigma_d} \frac{1}{\omega_o^{1+1/n}} \exp[-((d_c^2/2\sigma_d^2)(\frac{\omega_c}{\omega_o})^{1/n} - 1)^2]. \tag{42}$$

It is centered at $\omega_c = E_c/\hbar$ and has a FWHM of 320 meV. The PS dielectric constant is then computed as $\epsilon = \epsilon_b + 4\pi\chi(\omega)$, where ϵ_b is the background dielectric constant of the layer.

The transfer matrix M for the whole PSM is then obtained by multiplying together the transfer matrices m of every single layer. For the j-th layer:

$$m_j = \begin{bmatrix} cos(\frac{\omega}{c}n_j l_j) & -\frac{i}{n_j}sin(\frac{\omega}{c}n_j l_j) \\ -in_j sin(\frac{\omega}{c}n_j l_j) & cos(\frac{\omega}{c}n_j l_j) \end{bmatrix} \ , \tag{43}$$

where $n_j = \sqrt{\epsilon}$, l_j is the width of the j-th layer and c is the velocity of light.

From this, the reflectivity $R = |r|^2$ and the transmittivity $T = n_{sub}|t|^2$ are calculated where n_{sub} is the index of refraction of the p doped silicon substrate and r and t can be calculated using:

$$r = \frac{M_{12} + n_{sub}M_{22} - M_{11} - n_{sub}M_{12}}{M_{21} + n_{sub}M_{22} + M_{11} + n_{sub}M_{12}} \quad , \quad t = \frac{2}{M_{11} + n_{sub}M_{12} + M_{21} + n_{sub}M_{22}} . \quad (44)$$

The absorption A is then calculated in the usual way as $A = 1\text{-}R\text{-}T$.

The results are shown in Fig. 77 [203]. The theoretical spectra exhibit the same behaviour as the experimental ones (Fig. 69 [199]). This result was expected in view of the nearly symmetric lineshapes of the PS luminescence spectra at low and room temperature. A broadening factor Γ for excitons pertaining to each single Si-nanocrystal is included in the linear susceptibility to take into account the scattering and the dephasing processes.

In Ref. [203], the detailed lineshape fitting procedure was not performed and the calculated spectra of Fig.77 have been obtained with $\Gamma = 30$ meV and $4\pi f = 1 \cdot 10^{-4}$. The Γ value is not critical and "reasonable" deviations from the reported values do not lead to strong modifications on the calculated spectra. The assumed value has been chosen to be of the order of the thermal energy. For the f value, it was found that the stronger oscillator strengths result in a saturation of the absorption at the cavity resonance yielding a calculated reflectance spectrum which deviates significantly from the experimental one.

D. Time resolved spectroscopy in porous silicon microcavities

To verify whether, the increase of the spontaneous emission intensity is reflected into a decrease of the time decay of the luminescence and then in an enhancement of the spontaneous emission rate, time resolved measurements have been carried out on PSM [215]. Some characteristics of the samples studied are reported in table IX. The evolution of the luminescence spectra with respect to the time delay from the excitation pulse is shown in Fig. 78 [2]. The following facts are observed:

- the peak at $\lambda_c = 730$ nm does not move as a function of the delay;

- the decay of the side-band luminescence is faster than that of the λ_c peak;

This last point is a surprising result. Due to the microcavity effect on the photon mode density $G(\hbar\omega)$, one would have expected a shortening of the decay at λ_c and not for $\lambda \neq \lambda_c$.

The time decay of the luminescence at λ_c is shown in Fig. 79 [2] where also the time decay of a reference PS sample at the same observation wavelength is reported for comparison. A faster decay for the PSM than for the PS is observed. The luminescence decays with a stretched exponential lineshape (Eq. 12) both for the PSM and the PS. A summary of the wavelength dependence of the τ and β parameters is given in Fig. 80. For the reference PS sample, an increasing τ and an almost constant β are observed as λ increases. On the contrary, a bell-shaped τ vs. λ relation centered on λ_c is observed for the PSM sample (see also table X). By comparing the absolute τ value at λ_c of the PSM with that of the reference PS sample a decrease by a factor 1.2 or 1.9 for the λ_c or $\lambda_c/2$ cavities, respectively, are measured. The τ values for $\lambda \neq \lambda_c$ could be compared with those measured for the mirror sample (table X, second row).

A strong dependence on the excitation power intensity (J_{exc}) has been observed. The time integrated data under pulsed excitation are reported in Fig. 81 where the luminescence spectra for three different J_{exc} values are reported. As J_{exc} increases, the peak at λ_c is enhanced and some luminescence appears from the background, due to the mirror emission. A saturation of the mirror absorption is observed, which leads to an increased direct excitation of excitons in the central layer. This feature will be rediscussed in Sec. VI E and at the light of the temperature dependent data, a qualitative model for this behaviour will be proposed.

The J_{exc} dependence of τ is reported in table XI. For $\lambda \neq \lambda_c$ the τ are almost independent on J_{exc}, while they increase at λ_c. This is due to the increased central layer emission. In fact at λ_c one can observe the emission of both the mirrors (fast decay) and of the central layer (slow decay). As the J_{exc} increases and the mirror emission is saturated, the central layer emission dominates and the decay is lengthened. A complementary information can be derived from the dependence on the observation angle ϕ, of τ and β as reported in Fig.

67

82. As soon as ϕ is increased, the photon confinement in the optical cavity weakens, and a lower exciton-photon coupling is observed. Since the coupling between the exciton and the photon weakens, due to the lower confinement of the photon modes, the luminescence decay time shortens and, eventually, becomes equal to those typical for the mirror emission. A very weak ϕ dependence is expected for the mirror luminescence. No ϕ dependence has been indeed observed for the luminescence decay at wavelengths longer or shorter than λ_c.

The theoretical predictions report that no change in the luminescence lifetimes should be expected for microcavities formed with DBR, [185]; the observed shortening can be explained by the investigation of the effects of varying the refractive index of the central layer (n_c) while keeping constant the parameters of the Bragg reflectors. In this way, the effect of the photon confinement by the optical cavity is separated from the bulk excitonic effect. A series of three PSM with 45%, 62% and 75% porosities of the central layer have been investigated together with the corresponding reference PS samples (table IX). A comparison of the respective reflectivity spectra is given in Fig. 83. The luminescence intensity of these samples is reported in Fig. 84 and compared with that of a reference DBR and of the reference PS samples. Note that the reference PS sample with a porosity of 45 % does not show any luminescence within the sensitivity of the experimental set-up used. By looking at Fig. 84 and at the tables XII and XIII, many comments are possible:

- the luminescence intensity of the PSM samples shows an enhancement for λ_c both with respect to the mirror luminescence and to the PS reference luminescence;

- this enhancement is dependent on n_c, it increases by increasing n_c;

- the overall luminescence intensity increases with increasing n for the reference PS samples, while it decreases with increasing n_c for the PSM samples;

The time resolved measurements are summarized in tables XII and XIII. Also for the τ some comments are worth to be done:

- the τ values at λ_c, increase as n_c decreases;

68

- the ratio of the τ value at λ_c for the PSM, with respect to that of the reference sample increases as n_c decreases; its value is always ≤ 1;

Two main experimental observations merit a detailed discussion: a) the shortening of τ for the PSM at λ_c with respect to the reference PS samples and as a function of n_c; b) the faster decay observed for $\lambda \neq \lambda_c$ than for λ_c in the PSM.

The theoretical treatment of the coupling of the electronic resonance with the optical mode inside a microcavity has been reviewed in Ref. [185] by using classical arguments. It has been shown that dielectric microcavities differ from ideal or metallic microcavities for the finite reflection angle where the coupling is effective and for the penetration of the optical mode into the distributed Bragg reflectors. The finite reflection angle is reversed on the fact that the spontaneous emission rate is modified only for the light emitted into such high reflectivity angles and it is virtually unmodified for all the other emission angles where the emission radiates into leaky waveguide modes. As a consequence, the planar microcavity does not modify the spontaneous emission rate by any appreciable amount, and the emission is simply redistributed in the available space. In addition, inside a Bragg mirror the reflections are distributed over most of the interfaces, the optical mode confined in the central layer penetrates into the Bragg mirrors and, hence, part of the energy is stored in the mirrors.

On the basis of this facts, the modified CW luminescence lineshapes in PSM are explained by the redistribution of the emission in the space available to the photon mode, while one would not expect any variation in the emission lifetime. The observed variations are then due to the change of the local dielectric environment caused by the finite penetration depth of the optical modes into the mirrors.

The spontaneous emission rate $R_{sp}(\hbar\omega)$ for a bulk material is given by Eq. 29 where the photon mode density $G(\hbar\omega)$ is

$$G(\hbar\omega) = \frac{n^3(\hbar\omega)^2}{\pi^2 c^3 \hbar^3},$$

(45)

and n is the refractive index of the material.

69

In Eq. 29 the electronic transitions couple with the optical mode which has an energy $\hbar\omega$ equal to the transition energy. In a microcavity the electronic transition occurs in the central layer; however the optical mode, to which the excitonic transition couples, is extending inside the DBR. Consequently the refractive index used into Eq. 45 is not that one of the central layer but an average of the refractive indexes of the layers where the optical mode extends.

An estimate of the penetration length (ℓ_p) of the photon mode into the DBR is given in Ref. [216]

$$\ell_p = \frac{\lambda_c}{4n_c} \frac{q}{1-p} \frac{\left(1 + a^2 p^{m-1}\right)\left(1 - p^m\right)}{\left(1 + q^2 a^2 p^{2m-2}\right)} \, , \tag{46}$$

where $q = n_c/n_L$, $p = n_L/n_H$, $a = n_H/n_{air}$ or $a = n_H/n_{Si}$, whether the top DBR or the bottom DBR is considered, n_{air} and n_{Si} are the refractive indices of air and silicon, respectively, and m is the number of stacks into the DBR.

The effective refractive index n_{DBR} of the DBR can be approximated by the spatial average between the high and the low refractive indexes, i. e. $n_{DBR} = (n_H \ell_H + n_L \ell_L)/(\ell_H + \ell_L)$ where ℓ_H and ℓ_L are the respective thicknesses of the various layers of the DBR.

Hence the effective refractive index, n_{eff} entering into Eq. 45 is approximated by the average over the spatial extent of the optical mode

$$n_{eff} = \frac{n_{DBR}\ell_p^{Si} + n_{DBR}\ell_p^{air} + \lambda_c/2}{\ell_p^{air} + \ell_p^{Si} + \lambda_c/(2n_c)} \, , \tag{47}$$

where ℓ_p^{air} and ℓ_p^{Si} are the penetration lengths on the air side and on the Si side, respectively. Table XIV reports the results of such a calculation. Let us note that:

- the ℓ_p for the two, one-year old samples are shorter than for the other three samples, because for the former the central layer is embedded between two high refractive index layers

- the penetration depths are longer on the air side than on the Si side

- the large dielectric mismatch between the average refractive index of the DBR and that of the central layer is greatly reduced if one considers n_{eff} instead of n_c

- for the second set of samples, due to the small thickness of the central layer with respect to the penetration depth of the optical mode into the DBR, n_{eff} has a weaker dependence on the central layer porosity than n_c.

If one could neglect the contribution of the non-radiative transitions, the measured luminescence decay times would be related to the radiative lifetime and, hence, should fit the n-dependence given by Eq. 45. Again this hypothesis will be better discussed in Sec. VI E. Figure 85 reports τ^{-1} as a function of n [215]. All the data for a representative set of PSM, summarized in table XII, are there reported. n_{DBR} and n_{eff} have been used for the mirror and PSM data. A power law fit to the data yields $1/\tau \propto n^{3.4}$, which is very similar to the cubic dependence predicted by Eq. 45.

One conclusion is now possible from this figure: the measured $1/\tau$ values show a dependence on the refractive index which explains most of the observed results. In particular:

- the luminescence decay is faster for the mirror than for the PSM due to the larger refractive index of the mirror than for the PSM;

- the reduced lifetimes observed in the PSM with respect to the reference PS samples are due to the different refractive indexes (n_c versus n_{eff})

- the dependence of the luminescence enhancement on n_c (see table XIII) is a consequence of the dependence of the luminescence intensity on n (Eq. 5). In fact $I_{PL} \propto 1/\tau \simeq n^3$.

E. Temperature dependence of porous silicon microcavities

In Fig. 86 the PL spectra of a PSM have been reported for various temperatures T [211]. As T increases to room temperature (RT), the lineshape remains unchanged, and the main variation is in the relative emission intensity from the cavity and the mirrors. In the figure, the various PL spectra are normalized to the mirror emission. Thus one observes an increased emission from the cavity for T up to 150 K, then for higher T the emission of

the cavity weakens with respect to the mirror emission. Other details on the temperature dependence of the emissions are reported in Fig. 87.

Fig 87(a) shows the peak intensity (I_{PL}) of the cavity resonance mode as a function of T. A bell-shaped curve is observed as with standard PS samples. [1] This behaviour has been already explained as due to the interplay of radiative and non radiative recombinations. At low T the PL is dominated by radiative recombinations, where the radiative lifetime is due to the thermal balance between occupation of the dipole-prohibited triplet state and the dipole-allowed high energy singlet state. As T increases the singlet population increases and the luminescence intensity increases. When T is high enough, fast non-radiative recombinations occur and the luminescence intensity decreases. This general trend is respected in Fig.87(a).

Fig. 87(b) reports the T dependence of the cavity peak position. As T decreases from RT down to 150 K, λ_c diminishes. In addition, decreasing T, λ_c remains constant within the experimental error bars. The decrease in λ_c reflects the temperature variation of n_c: $\lambda_c = n_c \times d$, where d is the cavity thickness. The FWHM of the emission peak ($\Delta\lambda$) is given in Fig 87(c). The nearly constance of $\Delta\lambda$ vs. T indicates that the linewidth of the cavity mode is determined only by the microcavity structure and not by the excitonic thermalization for all the T-range here investigated.

It is of interest to know how the enhancement of the emission intensity (I_{PL}) observed for PSM depends on T. In Fig. 88, it is reported the emission intensity, and the ratio (γ) of I_{PL} at λ_c for a PSM and for a reference PS sample as a function of T. For this sample, $\gamma \simeq 2$ at room temperature. γ is almost independent on T as long as T>100K , while it increases strongly at lower temperatures. The inset shows the T dependence of I_{PL} at λ_c for the PSM and the reference PS sample. A bell-shaped I_{PL} profile is measured for both the samples but the I_{PL} maximum occurs at lower T for PSM than for PS. The T dependence of τ is reported in Fig. 89 for PSM and PS at λ_c . The same trend as that observed for the usual PS samples is observed [172]. For what concerns β (not shown in the figure), it is constant from 300 K down to 100 K, and then decreases as T is decreased. Both these trends have been already explained: for τ, by introducing a two levels system (singlet and

triplet excitons) and by assuming the exciton thermalization between them [173], for β by assuming a dispersive diffusion of excitons in a disordered Si-nanocrystals arrangement and by introducing the trap-controlled hopping of excitons [172].

The τ vs. T dependence can be described by the temperature dependence of the occupation of the singlet and triplet levels [173]:

$$\tau_{\text{rad}}(T) = \tau_{\text{trip}} \left[\frac{1 + (1/3) \exp(-\Delta E_x / k_B T)}{1 + (1/3)(\tau_{\text{trip}} / \tau_{\text{sing}}) \exp(-\Delta E_x / k_B T)} \right], \tag{48}$$

where τ_{trip} is the triplet lifetime, τ_{sing} the singlet lifetime and ΔE_x the singlet-triplet energy splitting. A fit of the experimental data for T< 150 K (see Fig. 89) yields the parameters reported in the Table XV. ΔE_x is essentially unchanged by the cavity structure while the singlet and triplet lifetimes show different values in PSM and PS. In the last column of the table, the data for $\lambda \neq \lambda_c$, i.e. representative of the mirror emission, are reported.

The inset of Fig. 89 shows the ratio of the PSM and PS lifetime at λ_c. Its value is lower than one (i.e. the lifetime of PSM is shorter than that of PS within the error bars) down to 40 K where it starts to grow. This is the temperature region where the recombination from the triplet states dominates.

The variations of the PL spectra at room temperature for various excitation intensities (J_{exc}), is reported in Fig. 90. As J_{exc} increases, the cavity mode emerges from the background of the mirror luminescence and a well resolved peak is measured.

The J_{exc} dependence of I_{PL} is shown in Fig. 91 for various T.

$I_{\text{PL}} \propto J_{\text{exc}}^\alpha$ with $\alpha \leq 1$. α vs. T is shown in Fig. 92. An almost constant α is observed. Only at low T, α goes to the value of about 0.5. On the other hand, τ and β are roughly constant when J_{exc} is varied.

The present experimental data support the conclusions reached in Ref. [215], which are based on the theoretical work of Ref. [185]. In addition, the following points can be stated:

- The coupling of the singlet state with the photon mode reduces the singlet lifetime in the PSM. This contributes to the increase in the overall luminescence intensity

and to the fractional shortening of the time decay of the luminescence (which is also dependent on the local dielectric environment).

- The luminescence lifetime at low temperatures (here identified with τ_{tripl}), is due to the balance between the non-radiative and the radiative, but not dipole-allowed, recombinations (see Fig. 2 in Ref. [172]). The results for the different samples are due to sample-dependent properties rather than to the microcavity structures.

- It is mainly in the intermediate temperature range where the thermal population of the singlet state is important, that the two-levels internal structure of the excitons in PS plays a role. The different T of the maxima of I_{PL} for PSM and PS are explained by the lower τ_{sing} in PSM than in PS. In PSM samples with a very long τ_{tripl} as those reported in Ref. [203], I_{PL} increases monotonously even at low T. At room T, the lifetime is again governed by the balance of the radiative and non-radiative recombinations. However, as already observed in Ref. [217]:

$$W_{\text{tot}}(n) = W_{\text{nr}} + W_r \simeq W_{\text{nr}} + f(n)W_r^0 \qquad (49)$$

where W_{xxx} are the total (xxx=tot), non-radiative (xxx=nr) and radiative (xxx=r) recombination rates, respectively. $f(n)$ is a function which gives the dependence of the radiative recombination rate on the effective refractive index, already introduced in Eq. (45) and discussed in Ref. [215]. W_{nr} is independent on n.

Eq. (49) explains why the microcavity effects, i.e. the variation of W_r with n through $f(n)$, are observed even at room temperature where W_{nr} is large.

- The J_{exc} dependence of the PL spectra shown in Fig. 90 is due to the saturation of the mirror absorption as the excitation intensity is increased. As more excitons are directly photogenerated into the cavity layer due to the increased transparency of the mirror (result of the absorption saturation), the luminescence at the cavity wavelength increases with respect to that at different wavelengths.

- The power dependence of the PL intensity at λ_c and the temperature dependence of the α exponent are due to the saturation of the mirror emission at λ_c. In fact, the luminescence at λ_c is due to the sum of the mirror luminescence (I_{PL}^M) and the cavity emission (I_{PL}^C):

$$I_{PL} = I_{PL}^M + I_{PL}^C \; . \tag{50}$$

Even tough I_{PL}^C can have a linear dependence on J_{exc}, I_{PL} has a sublinear dependence due to the mirror contribution. In fact, the absorption saturation of the mirror luminescence can be modellized in the following way:

$$I_{PL}^M \propto (1 - T)J_{exc} \; , \tag{51}$$

where T is the transmission coefficient of the mirror, i.e. (1-T) is the absorbance in the mirror layers.

$$T \simeq \exp\left[-\chi(J_{exc})d_M\right] \; , \tag{52}$$

where $\chi(J_{exc})$ is the excitation intensity dependent absorption coefficient of the mirror layers (with a total thickness of d_M). In a simple model

$$\chi \simeq \frac{\chi^0}{(1 + J_{exc}/J_{exc}^S)} \; , \tag{53}$$

and the J_{exc}^S is the saturation intensity. As J_{exc} increases, T increases, (1-T) decreases and the contribution from the recombination in the mirror spatial region decreases, which causes an $\alpha < 1$. A schematic idea of this behaviour is shown in the inset of Fig. 92, where a power law fit of the resulting I_{PL}, yields an $\alpha \simeq 0.84$. As J_{exc}^S depends on the temperature and increases for low T, this causes a larger contribution of I_{PL}^M to I_{PL}, which in turn causes a decrease in α because most of the excitons are photo-excited in the mirror region, which exhibits the strongest absorption saturation.

- No variations in ΔE_x caused by the PSM are observed because a weak exciton-photon coupling is present in PSM.

F. Coupled porous silicon microcavities

Recently, coupled cavities made of III-V semiconductors have been grown and characterized. [218–221] These structures consist of two coupled planar Fabry-Perot microcavities, surrounded by external DBR : the coupling is achieved via a central Bragg mirror (see Fig. 93 [213]). The coupling of the degenerate cavity modes through the central DBR induced by the coherent optical field leads to an optical splitting of the eigenmodes [218,221]. Dual wavelength lasing has also been observed in vertical cavity surface emitting lasers (VCSELs) structures. [219,220] The coupled cavity structure adds another degree of freedom in the tailoring of spatially confined light-matter coupling; it may lead to interesting effects as for example the transfer of the excitation from one cavity to another.

In this Section we describe the growth of coupled PSM with good optical properties. The layer sequence used to form the coupled PSM is as follows: air–HL...($\times 8$)...HL–$\underline{S_1}$–LH...($\times 4.5$)...L–$\underline{S_2}$–LH...($\times 8$)...LH-substrate where S_1 and S_2 are the first and second cavity. The final structure is depicted in Fig. 93 and is composed by three DBR (top mirror DBR_1, central mirror DBR_2 and bottom mirror DBR_3) formed by $\lambda/4$ stacks and two $\lambda/2$ cavity regions, S_1 and S_2. In the balanced PSM, i.e. in a sample where S_1 and S_2 are equal, their thickness is $L_c = \lambda_c/(2n_c)$. The various samples are characterized by different values of the thicknesses of S_1 and S_2 as detailed in Table XVI.

In Figure 94, the reflectivity spectrum of the balanced coupled PSM is proposed. The characteristic high reflectivity region due to the stop-bands of the three DBRs extends from 650 to 850 nm. Within this wavelength (λ) region, two reflectivity resonances are observed at 739 and 766 nm due to the coupling between the optical modes confined in the first and second cavity. A maximum transmittivity of 0.44 and 0.27 is associated to the low and high λ resonance, respectively. Even though the two cavities are equal, a different transmittivity is observed, due probably to the residual absorption of the central DBR at these wavelengths.

In order to study the coupled PSM in a deeper way, a serie of samples with different mismatches between the two cavity layers has been produced and characterized. Figure 95

shows the photoluminescence spectra at room temperature for the various samples. Some information extracted from these spectra are summarized in Table XV.

The overall shape of the luminescence spectra is similar for all the samples and very different from that typical of PS. Instead of a wide emission band characteristic of PS, several peaks are observed corresponding to the reflectivity minima of the PSM structure (see, e.g., Fig. 94). At the wavelengths of the coupled cavity modes, two peaks are observed, whose intensities depend on the mismatch between the S_1 and S_2 cavities. The peculiar features of the PSM luminescence compared to that of PS are a consequence of the photon confinement in the cavity structure and have been discussed in length in preceding sections of this paper and in Refs. [2,203,222]

Let us here concentrate only on the novel phenomena introduced by the coupled cavity structure. For the balanced sample labeled "a" (central spectrum in Fig. 95), two narrow peaks are observed at 739 and 765 nm corresponding to the transmittivity maxima measured in the reflectivity spectrum shown in Fig. 94.

By varying the mismatch between S_1 and S_2, several observations are possible:

- the growth process is well controlled as similar spectra are observed for the various samples, so we can conclude that all the variations are due to the different etching parameters used;

- the peak intensities vary as a function of the ΔL_c (the thickness difference between S_1 and S_2). In particular, the low λ peak is stronger for sample labeled "c" and the high λ peak is strongest for the sample "e". In the balanced sample "a", an intensity difference between the emission of the two cavity modes is observed due to a residual absorption present in the DBR and to the wavelength dependence of the PS emission band (in the following we will refer to this fact as an asymmetry in the intensity);

- the spectral position does not change as a function of ΔL_c except for samples "c" and "e", where a peak is spectrally aligned with those measured for the other samples,

while the other peak is shifted to smaller (larger)wavelengths in the case of sample "c" (sample "e");

- the linewidth of the luminescence peaks is almost independent of ΔL_c and significantly smaller than that typical of PS [222].

The theoretical modeling of the experimental results is done by assuming the following dielectric constant $\epsilon(\omega) = \epsilon_\infty + 4\pi\chi(\omega)$ in each layer, where $\epsilon_\infty = n^2$ is the background dielectric constant, and $\chi(\omega)$ is a contribution arising from optical transitions close to the band gap. We assume for each PS layer a model of nano-crystals with dispersion of sizes, and assume the energies of spatially confined oscillators to be distributed according to a Gaussian function centered at ω_0:

$$P(\omega) = \frac{1}{\Delta\sqrt{\pi}} \exp(-\frac{(\omega - \omega_0)^2}{\Delta^2}). \tag{54}$$

The width Δ of the distribution corresponds to the width of the bulk PS photoluminescence [2]. Both ω_0 and Δ depend on the porosity, with a trend of increasing ω_0 for increasing porosity, probably due to a smaller size for the Si nano-crystals. However since the distribution of the PS photoluminescence is much larger than the energy range of interest (i.e. it extends well outside the stop band of the PSM structure) the same values for all PS layers are assumed. For the same reason, the results shown below do not depend on the precise form of the resonance frequency distribution: a different form, as assumed in Ref. [203] yields to similar results. The resonant susceptibility is then obtained by a convolution of the single-oscillator form with the frequency distribution:

$$\chi(\omega) = \int_{-\infty}^{\infty} P(x) \frac{\beta x^2}{x^2 - \omega^2 - 2i\gamma\omega} \, dx. \tag{55}$$

The susceptibility (55) can be expressed in terms of the complementary error function. Reflectivity and absorption spectra are then calculated by solving Maxwell equations by the usual transfer-matrix method [181,223].

The calculations have been performed with the experimental parameters as the input. The external (central) DBR have $N_1 = N_3 = 8$ ($N_2 = 4.5$) pairs, respectively. The pa-

rameters of the oscillator model are $\hbar\omega_0 = 1.65$ eV ($\lambda_0 = 750$ nm), $\Delta = 285$ meV, $\gamma = 15$ meV.

Useful analytical results for the double-microcavity configuration can be obtained by parameterizing the transfer matrix of the Bragg mirrors in terms of their amplitude reflection coefficients: this allows to obtain the transfer matrix of the whole structure, and to calculate the energies of the system eigenmodes, as the poles of the global transmission coefficient $t(\omega)$ (the procedure was first applied to single microcavities in Ref. [207]). For a structure with two identical cavities, the optically coupled Fabry-Perot modes can be classified in terms of their symmetric (S) and antisymmetric (A) states; their splitting at normal incidence is calculated as

$$\Delta_{\text{S-A}} = \frac{\hbar c\sqrt{1 - R_2}}{n_c L_{\text{eff}}}, \tag{56}$$

where $R_2 = 1 - 4(n_H/n_c)^2(n_L/n_H)^{2N_2+1}$ is the reflectivity of the central mirror, and $L_{\text{eff}} = L_c + L_{\text{DBR}}$ is an effective cavity length which includes the penetration depth of the electric field into the DBRs. Using the approximate formula $L_{\text{DBR}} = L_c n_L n_H/[n_c(n_H - n_L)]$, [207,223] we find $L_{\text{eff}} = 1.35$ μm and $\Delta_{\text{S-A}} = 54.6$ meV: this agrees with the experimental splitting of 50-55 meV shown in Fig. 95. This comparison shows that the coherence of the optical field is maintained over the whole thickness of the central DBR, and therefore that the PSM have a quality which enables to show coherent coupling effects of the kind first reported for III-V coupled microcavities [218].

The parameter β appearing into Eq. (55) is proportional to the oscillator strength of the optical transitions in the nanocrystals. As already discussed earlier in this review and in Ref. [203], a comparison is possible between the calculated absorption spectrum and the experimental PL spectrum in view of the nearly symmetric lineshapes of the PS luminescence spectra which is a signature that the thermal contribution to the occupation of the high energy states is not as important as in other semiconductor systems. When comparing with PL measurements, where only the lowest-lying states of each nanocrystal are probed, β has to be interpreted as the oscillator strength "at the band gap" for each nanocrystal in the

corresponding PS layer, averaged over the not-homogeneous size distribution. This oscillator strength is known to decrease with nanocrystal size [224], since it must go to zero in the limit of a bulk Si crystal with indirect gap. In Fig. 96, the calculated absorption for different values of the parameter β (which for simplicity is taken to be frequency-independent and the same in all the layers) is shown. When $\beta < 10^{-5}$ absorption is concentrated in the cavity peaks, while for $\beta > 10^{-4}$ most of the absorption takes place in the side-band of the mirrors. The experimental indication that the PL intensities in the cavity peaks and in the side-band are comparable (see Fig. 95) points to an optimal value of β between 10^{-5} and 10^{-4}. In the following, $\beta = 3 \times 10^{-5}$ is assumed.

The parameter β is related to the oscillator strength by

$$\beta = \frac{e^2}{m\omega_0^2} \frac{f}{V}, \tag{57}$$

where f/V is the oscillator strength per unit volume. Taking the volume of a unit cell, the oscillator strength per cell $f_{\text{cell}} \simeq 4 \times 10^{-5}$. This compares well with the values calculated by Delley and Steigmeier [224] for the larger nanocrystals. Also, with this value for the oscillator strength, a radiative decay rate $\Gamma = 2ne^2\omega f_{\text{cell}}/(3mc^2) \sim 2$ ms^{-1} is obtained, close to the values calculated in Ref. [214] for a band-gap of 1.6 eV. We may then conclude that the present PSM structures are characterized by nanocrystals with a small oscillator strength; this is consistent with the explanation of the visible PL band in terms of radiative recombination of electron-hole pairs (or excitons) at the band gap of Si nanocrystals, with a slow radiative lifetime in the msec. range.

In Fig. 96, the calculated absorption (a) and reflectivity (b) for the parameters of the five samples are shown. To notice that, when the refractive index is a real number, a cavity mismatch alone does not yield to a different intensity of luminescence peaks or of the reflectivity dips: on the other hand a cavity mismatch combined with a complex refractive index produces an appreciable asymmetry between the two peaks, which is similar to the observed one. In our case the imaginary part of the refractive index is provided by the resonance frequency distribution when a finite value of γ is considered: the precise value

80

of γ is uninfluent. Since the cavity S_1 (the outer one) gives the largest contribution to the reflectivity and the absorption spectra, when the outer cavity is thicker, the peak at higher wavelengths is more intense (samples "b" and "c"); on the other hand when the outer cavity S_1 is thinner (samples "d" and "e") the peak at lower wavelengths is more pronounced. Comparing with the experimental results shown in Fig. 95 we can see that the qualitative features with increasing cavity mismatch are well reproduced. In the calculations, the peak positions change very few with the cavity mismatch: the variations observed in Fig. 95 are due to slight deviations of sample parameters from the nominal ones.

The results of Fig. 96 show two discrepancies compared to the experimental ones in Fig. 95: the stop band is wider, and the cavity peaks are narrower. Thus it could be asked whether a different choice of the refractive indexes might lead to a better agreement with the experiment; in particular the stop band can be made narrower by choosing a smaller ratio of "high-to-low" refractive index in the DBR. In Fig. 97, the influence of a different refractive index ratio on the absorption spectra is shown. Although with this choice the width of the stop band agrees with the experimental one (not reported here), the peak separation increases due to a decrease of the reflectivity R_2 of the central DBR in Eq. (56), and the peak asymmetry in the presence of a cavity mismatch is reduced; the linewidth of the peaks also increases due to the decrease of the reflectivity of the external DBR. Thus a different choice of the refractive indexes would spoil the good agreement between measured and calculated optical splitting. We conclude that the narrower stop band and the broader peaks observed in the experiment do not originate from different values of the refractive indexes, but rather from disorder effects into the DBR [213].

VII. APPLICATIONS OF POROUS SILICON MULTILAYERS AND MICROCAVITIES

A. Waveguides

The possibility to vary the refractive index in depth gives immediately the idea of producing PS based waveguides [225,226]. This fact is important in view of the realization of an all Si based integrated circuit where the information are routed through waveguides in form of photons. As an example, a fully integrated optical circuit based on PS has been proposed by Lazarouk et al. [227].

A planar waveguide is composed of a high refractive index layer surrounded by lower refractive index cladding layers. In Ref. [225] both planar and strip PS waveguides have been formed on 0.1 Ωcm p-type doped silicon wafers by etching a three layers structure, where a core layer of 62 % porosity is sandwiched between two cladding layers of 75 % porosity. Light guidance has been demonstrated for 1.28 μm in as-prepared samples and for 0.63 μm in oxidized samples. Interface roughnesses in the range of 50-100 nm have been observed to concurr to the losses in the waveguide. In as-anodized samples losses between 10-20 dBcm^{-1} have been measured with multimode guidance for the planar waveguide and single mode behaviour for the stripe waveguide. The oxidation removes the absorption in the visible and consequently let the 0.63 μm light to be guided. In oxidized samples the losses were between 6.7-14 dB cm^{-1}. This has been attributed to roughness scattering at the interface between the cladding and the core layers.

An alternative structure has been proposed in Ref. [226] where a core PS region (1μm thick with a refractive index of 1.8 at 800 nm) is in between a bottom cladding PS layer (3 μm thick with n=1.5) and a thin top cladding layer of evaporated Al ($\simeq$35 nm thick). By surface excitation and looking at the edge, guiding of the light has been observed with polarization dependence. Transverse-Electrical (TE) modes are efficiently guided at 850 nm while Transverse-Magnetic (TM) are not.

B. Enhancement of weak absorption signals

It has been recently demonstrated the possibility to enhance the absorption intensity of species present in the porous silicon layer embedded by Bragg mirrors [228]. This is accomplished by tuning the Fabry-Perot maximum on the energy of the absorption transition one wants to enhance. For example an increase up to 14 times in the infrared absorption band of the Si-H vibration (2088 cm^{-1}) has been measured [228]. This demonstrates the potentiality of PSM to study the incorporation of species at the surface of PS (see Fig. 98). It is worth to mention also the recent proposal of the use of PSM to enhance the Raman intensity of the PS layer embedded in the cavity [228,229].

C. Optical non linearities

Another interesting application of PSM can be foreseen in the field of the non-linear optics. The narrow emission line and light confinement effect in the planar optical resonator can be exploited in several non-linear optical applications like for example second harmonic generation, optical bistability and all-optical switching. Fig. 99 [187] shows the reflectance spectrum of PSM in the resonance region for two different continuous wave pump intensities and in the inset the reflectance for a fixed λ as a function of the CW pump intensity [187,195]. Two effects were observed comparing low and high pump intensity results: 1) the resonance is shifted at low wavelength and 2) the reflectance is increased at a fixed λ. Both these facts are a result of the saturation of the absorption at high pump intensities and are observed at a much lower pump power than in single porosity PS samples [230]. The blue-shift of the reflectance dip is attributed to a lower effective refractive index value reflecting the saturated absorption. Thermal effects cannot explain these observation because they would yield an increased n_c and a red-shift of the resonance dip. The role of photochemical effects to cause these observations are still unclear.

It has been recently reported second harmonic generation in PSM structures too [231].

D. Resonant cavity light emitting diodes

The implementation of PSM in light emitting devices (LED) will realize some advantages with respect to conventional LED [232–234]:

i) spectral purity of the emission with a narrow emission band, which will improve both the color sharpness in flat-panel display applications and the transmission bandwidth for interconnections or data communications.

ii) improved directionality in the emission pattern which will improve the coupling efficiency between the source and the transmission line, and the power efficiency in flat-panel displays avoiding the loss of optical power along undesired lateral directions.

iii) high spontaneous emission intensity which will increase the internal/external quantum efficiency resulting in an improved yield of the device.

In the literature two examples of these so called resonant cavity light emitting diodes (RCLED) have been reported and some of these properties have been demonstrated [186,235]. However both RCLED structures were based on metal contact which produces an inefficient electrical injection [236].

In Ref. [186] by evaporating a thin Al layer (15 nm) on the top of a PSM sample a RCLED was realized. When forward biased, the diode showed a weak but measurable electroluminescence. The light intensity versus injected current characteristics (see Fig. 100) is almost linear for low currents and saturates at high current [187]. The RCLED yielded the same light intensity as a reference LED, formed by a λ_c-thick PS layer, but at current densities one order of magnitude lower or at a factor 8 lower electrical power (see the inset of Fig. 100). This was a consequence of a geometrical factor, i. e. better collection efficiency of the detection system when the RCLED is used due to the directional emission, and probably of the increased spontaneous emission intensity for the microcavity based LED. A further, unexpected, result was a reduced degradation of the electroluminescence with time for the RCLED with respect to the reference LED.

84

It is known that atmospheric impregnation causes a degradation of the emission properties of PS-LED [237]. Vacuum operation [238], or deposition of a protective cap-layer (e.g. alumina or polycrystalline silicon films) [239], or oxidation [240] have been used to avoid such problems. It has been also demonstrated that the use of a multilayer film on the top of the active layer can have beneficial effects in the stabilizing of the emission properties: the emission intensity of the reference LED decreased by more than an order of magnitude after 30 min, while that of the RCLED decreased by a factor of 4 after 120 min.

In Ref. [235] a slightly different structure of RCLED has been demonstrated (Fig. 101) [235]. An active layer is embedded between a bottom DBR and a top 12 nm thick Au layer which deserved both as top mirror to form the optical cavity (reflectivity of about 40 %) and as top electrode to inject the current. When the bias voltage was $\geq$40V a significant current was flowing through the device and the electroluminescence was observed both for forward and inverse biases. This is due to the large RCLED thicknesses caused by the formation of the DBR. The electroluminescence spectrum is shown in Fig. 102 in comparison with the PL spectrum of the same sample [235]. One can easily notice that the narrowing of the luminescence band is preserved also in the electroluminescence experiment. The spectral shape is independent on the bias voltage.

E. Optical sensor

Nowadays, online material and process control, rely heavily on optical methods due to their spectral sensitivity, contactless way of measure and velocity in data evaluation. A simple optical sensor that permits to do quantitative absorption spectroscopy has been demonstrated using PS-DBR [241]. The layout of the sensor is shown in Fig. 103 [242]. It exploits the narrow stop-band of the DBR to accomplish the necessary spectral decomposition. The light transmitted or reflected by the sample under investigation is impinging onto various DBR and back-reflected to the detector. The sensor output for a sample to be analyzed is the set of detector readings for each DBR. Several applications of this sensor

are reported in Ref. [242]: color recognition, thickness monitoring and analysis of infrared absorption bands. An example is given in Fig. 104, where the thickness of an Ag layer deposited onto a glass plate has been measured by measuring the transmittance of the layer with the PS-based optical sensor.

F. Color sensitive photodiode

Color sensitive Si-photodiodes have been fabricated by using PS interference filters integrated in the p^+ doped part of conventional Si photodiode based on p/n junction [243]. The proposed device structure is shown in Fig. 105 where it is evidenced the formation of the optical element (either a DBR or a FP) on the top [243]. Due to the transparency (at the right wavelengths) and the high resistivity of the PS multilayer, the photoelectrons are mainly generated in the bottom Si layer and not in the PS layer. Hence the PS layer acts simply as a passive element. The processing of the samples was very simple and it has the main advantage over the other approaches to be a cheap technology (compared to the cost of depositing by sputtering, multilayers of Si_3N_4, SiO_2 or TiO_2). A complication appeared for the formation of the PS multilayer structures, as the p/n diode has to be reverse biased in order to form PS in the p-type region. The structure has to be illuminated during the etching, which causes a variation both in the porosities and in the thicknesses of the layers. In turn this caused a deterioration of the reflectance quality of the DBR or FP structures so formed. However, preliminary demonstrators have been fabricated and the performance tested. In Fig. 106 the external quantum efficiency in short-circuit conditions of a diode with a DBR, is shown in comparison with a reference diode and with the reflectance of the DBR [243]. The spectral response of the p/n diode is modified with almost no signal in the DBR stop band region at 600 nm.

G. Metal-porous silicon microcavities

Fig. 107 shows the processing steps for metal-porous silicon microcavities [206,244]. A 0.4-0.6 Ωcm p-type doped substrate was employed. First, the active layer was formed by anodization with a current density of 200 mA cm^{-2} and a time duration of 8-10 s. The time duration was adjusted such that $nd = m\lambda_c$, where m is an integer. Then, a DBR was formed, which was made by 20 periods of PS layers with $n_H = 2.5$ and $n_L = 1.5$ (current densities 20 and 200 mA cm^{-2}, respectively). Finally, a thin Ag film ($\simeq$ 25 nm thick) was evaporated onto the top surface and used as a mirror and electrical contact. The reflectivity of the Ag film was higher than 90 % in the wavelength region of interest. The reflectivity of the bottom DBR had a value of about 0.9 in the stop-band [206].

This microcavity structure is, thus, different with respect to the PSM of the previous sections because the top DBR is substituted by the Ag mirror.

The luminescence spectra of some metal-porous silicon microcavities are reported in Fig. 108 [244]. A narrowing of the emission line down to 17 meV, i. e. $\Delta\lambda$= 7.7 nm, is obtained. The emission energy can be continuously tuned across the visible range by simply changing the thickness of the active PS layer (and accordingly of the layers composing the Bragg reflectors [244]. No enhancement in the emission intensity was detected for the metal-porous silicon microcavities, probably due to the low values for the reflectivity of the confining cavity. One could expect a stronger shortening of the time decays of the luminescence than for PSM, due to the better properties of the top metallic mirror with respect to the DBR.

By increasing the active layer thickness, a multimode behaviour in the waveguide-like structure is observed, and the emission linewidth is significantly decreased [206]. Side mode peaks become apparent due to the narrowing of the free spectral range as the cavity length is increased. The narrowest linewidth (6 meV i.e. $\Delta\lambda$= 2.7 nm) is measured for $nd = 10\lambda_c$.

VIII. CONCLUSIONS

The fascinating world of low dimensional Si structures has only now entered its infancy. It is our believe that low dimensional Si structures coupled with low dimensional photonic systems can play a major role in photonics, as we have underlined all along this review. However there are still many unfolded properties of these systems.

We are now starting to understand the physics of PS and to control its physical parameters in order to exploit its various properties. We join table XVII where many perspective applications of PS are indicated. In table XVIII a comparison of PS with other Si based light emitting systems is performed. As a result PS emerges as the most promising material to develop Si based light emitting diodes. The recent improvements in the engineering of the PS surface, the demonstration of a full integration of PS LED with both BJT or CMOS circuits, the use of microcavities to control the PS spontaneous emission are all recent results which point to an even brighter future for PS.

The mastering of the etch process to form PS layers of designed parameters, has allowed the formation of high quality dielectric multilayers with a competitive technique. VLSI compatibility, easy procedure and low cost of the experimental apparatus are all characteristics which render the anodic dissolution of Si very appealing, towards the realization of Si compatible dielectrics films. Optical devices (mirrors, filters, waveguides), optoelectronic devices (optical sensors, photodiodes, light emitting diodes) and microcavities have all been demonstrated, based on these structures.

In particular, for microcavities, both interesting fundamental physical properties and appealing device applications can be envisaged in the near future. The study of their physics is at the very beginning. The fundamental problem of a microcavity filled with a disordered array of silicon quantum dots still has to be theoretically tackled. Experimentally the luminescence and transport properties of the microcavities are beginning to be unfolded and more work should be performed. All the non-linear optical properties, such as the possibility of observation of super-radiance effects or of stimulated emission, have not yet

been addressed.

We think then that PS as a material basis for the optoelectronics for the near future is going to reach its own maturity, as the recent appearance of all porous silicon based optoelectronics devices demonstrates.

ACKNOWLEDGMENTS

REFERENCES

† Author to whom correspondence should be addressed. Email: VINEGONI@YAHOO.COM

[1] A.G. Cullis, L.T. Canham, and P.D.J. Calcott, J. Appl. Phys. **82**, 909 (1997).

[2] L. Pavesi, Riv. del Nuovo Cimento **10**, 1 (1997).

[3] L. Pavesi, and P. Dubos, Semicon. Science Technol. **12**, 570 (1997)

[4] A. Uhlir, Bell Syst. Tech. J. **35**, 333 (1956).

[5] L. Pavesi, Microel. J. **27**, 437 (1996).

[6] S. Setzu, G. Lerondel, R. Romestain, J. Appl. Phys. **84**, 3129 (1998).

[7] A. Halimaoui, in *Properties of porous silicon*, edited by L.T. Canham (IEE INSPEC, London, 1997) p. 12.

[8] R.L. Smith, and S.D. Collins, J. Appl. Phys. **71**, R1 (1992).

[9] L. Canham, New Scientist **23**, (April 1993).

[10] H. Foll, Appl. Phys. A **53**, 8 (1991).

[11] M.I.J. Beale, J.D. Benjamin, M.J. Uren, N.G. Chew, and A.G. Cullis, J. Cryst. Growth **73**, 622 (1985).

[12] M.J. Eddowes, J. Electroanal. Chem. **280**, 297 (1990).

[13] C. Pickering, M.I.J. Beale, D.J. Robbins, P.J. Pearson, and R. Greef, Phys. C **17**, 6535 (1984).

[14] V. Lehmann, and H. Foll, J. Electrochem. Soc. **137**, 653 (1990).

[15] V. Lehmann, and U. Gosele, Appl. Phys. Lett. **58**, 856 (1991).

[16] L. Pavesi, and V. Mulloni, J. Luminescence **80**, 43 1999.

[17] L. Pavési, J. Appl. Phys. **80**, 216 (1996).

[18] V. Lehmann Ref. [245] p.1.

[19] C. Mazzoleni, in Tesi di Laurea, Universitá di Trento, unpublished (1995).

[20] L.T. Canham, A.G. Cullis, G. Pickering, O.D. Dosser, T.I. Cox, and T.P. Lynch, Nature **368**, 133 (1994).

[21] G. Amato, and N. Brunetto, Mater. Lett. **26**, 295 (1996).

[22] O. Belmont, D. Bellet, and Y. Brechet, J. Appl. Phys. **79**, 7586 (1996).

[23] U. Gruning, and A. Yelon, Thin Solid Films **255**, 135 (1995).

[24] D. Bellet, in *Properties of porous silicon*, edited by L.T. Canham (IEE INSPEC, London, 1997) p. 38.

[25] L. Pavesi, and R. Guardini, Brazilian J. Phys. **26**, 151 (1996).

[26] D. Bellet, S. Billat, G. Dolino, M. Ligeon, and F. Muller, Solid State Comm. **86**, 51 (1993).

[27] J.M. Perez, J. Billabo, P. McNeill, J. Prasad, R. Cheek, J. Kelber, J.P. Stevens, and R. Glosser, Appl. Phys. Lett. **61**, 563 (1992).

[28] S. Schupper, S.L. Friedman, M.A. Marcus, D.L. Adler, Y.H. Xie, F.M. Ross, T.D. Harris, W.L. Brown, Y.J. Chabal, L.E. Brus, and P.H. Citrin, Phys. Rev. Lett. **72**, 2648 (1994).

[29] A.G. Cullis, and L.T. Canham, Nature **353**, 335 (1991).

[30] A. Borghesi, A. Sassella, B. Pivac, and L. Pavesi, Solid State Commun. **87**, 1 (1993).

[31] A. Borghesi, G. Guizzetti, A. Sassella, O. Bisi, and L. Pavesi, Solid State Commun. **89**, 615 (1994).

[32] L.T. Canham, and A.J. Groszek, J. Appl. Phys. **72**, 1558 (1992).

[33] M.S. Brandt, and M. Stutzmann, Appl. Phys. Lett. **63**, 2569 (1992).

[34] F. Koch, and V. Petrova-Koch in Ref. [246] p. 133; F. Koch, V. Petrova-Koch and T. Muschik, J. Lumin. **57**, 271 (1993).

[35] P. Buseck, J. Cowley, Le Roy Eyring, "High Resolution Transmission Electron Microscopy and Associated Techniques", Oxford Science Publications, 1992.

[36] Y.H. Xie, W.L. Wilson, F.M. Ross, J.A. Nucha, E.A. Fitzgerald, J.M. Macauley, and T.D. Harris, J. Appl. Phys. **71**, 2403 (1992).

[37] N. Noguchi, I. Suemune, M. Yamanishi, G.C. Hua, and N. Otsuka, Jpn. J. Appl. Phys. **31**, L490 (1992).

[38] A.G. Cullis, L.T. Canham, and O.D. Dosser, in "Light Emission from Silicon", edited by S.S. Iyer, R.T. Collins, and L.T. Canham (Materials Research Society, Pittsburgh, 1992), p. 7.

[39] A.G. Cullis, L.T. Canham, G.M. Williams, P.W. Smith, and O.D. Dosser, J. Appl. Phys. **75**, 493 (1994).

[40] S.F. Chuang, S.D. Collins, and R.L. Smith, Appl. Phys. Lett. **55**, 1540 (1989).

[41] R. Herino, A. Perio, K. Barla, and G. Bomchil, Mater. Lett. **2**, 519 (1984).

[42] G. Bomchil, A. Halimaoui, and R. Herino, Microelectronic Engineering **8**, 293 (1988).

[43] M.W. Cole, J.F. Harvey, R.A. Lux, D.W. Eckhart, and R. Tsu, Appl. Phys. Lett. **60**, 2800 (1992).

[44] K.H. Jung, S. Shih. D.L. Kwong, T. George, T.L. Lin, H.Y. Liu, and J. Zavada, J. Electrochem Soc. **139**, 3363 (1992).

[45] V. Lehmann, Adv. Mater. **4**, 762 (1992).

[46] V. Lehmann, B. Jobst, T. Muschik, A. Kux, and V. Petrova-Koch, Jpn. J. Appl. Phys. **32**, 2095 (1993).

[47] A. Nakajima, Y. Oshima, T. Itakura, and Y. Goto, Appl. Phys. Lett. **62**, 2631 (1993).

[48] O. Teschke, M.C. Goncalves, and F. Galembeck, Appl. Phys. Lett. **63**, 1348 (1993).

[49] O. Teschke, F. Alvarez, L. Tessler, and M.U. Kleinke, Appl. Phys. Lett. **63**, 1927 (1993).

[50] I. Berbezier, and A. Halimaoui, J. Appl. Phys. **74**, 5421 (1993).

[51] I. Berbezier, in Ref. [245], p. 207.

[52] A. Halimaoui, in Ref. [245], p. 33.

[53] A. Albu-Yaron, S. Bastide, D. Bouchet, N. Brun, C. Colliex, and C. Levy-Clement, J. Phys. I **4**, 1181 (1994).

[54] S. Gardelis, U. Bangert, A.J. Harvey. and B. Hamilton, J. Electrochem. Soc. **142**, 2094 (1995).

[55] A. Grosman, C. Ortega, Y.S. Wang, and M. Gandais, in "Structural and optical properties of porous silicon nanostructures", edited by G. Amato, C. Delerue, and H.-J. von Baerdeleben, Gordon and Breach Science Publisher Amsterdam (1997).

[56] J.P. Gonchond, A. Halimaoui, and K. Ogura, in "Microscopy of Semiconducting Materials", edited by A.G. Cullis and N.J. Long, IOP Publishing Ltd. Bristol (1991).

[57] G. Amato, N. Brunetto, and A. Parisini, Thin Solid Films **297**, 73 (1997).

[58] A. Bruska, E.V. Atrova, U. Falke, T. Raschke, Ch. Radehaus, and M. Hietschold, Thin Solid Films **297**, 79 (1997).

[59] J.M. Gomez-Rodriguez et al., Appl. Surf. Sci. **44**, 185 (1990).

[60] G.B. Amisola, R. Behrensmayer, J.M. Galliga, F.A. Otter, F. Namavar, and N.M.

Kalkoran , Appl. Phys. Lett. **61**, 2595 (1992).

[61] T. Yu et al., J. of Vac. Sci. and Technol. B **12**, 2437 (1994).

[62] C. Tsai et al., J. of Electr. Mater. **21**, 995 (1992).

[63] J.L. Coffer, S.C. Lilley, R.A. Martin, and L.A. Files-Sesler, J. Appl. Phys **74**, 2094 (1993).

[64] E. Ettedgui et al., Mater. Res. Soc. **283**, 173 (1993).

[65] H.J. Lee et al., J. Appl. Phys. **75**, 8060 (1994).

[66] F. Ruisz et al., J. of Vacuum Sci. and Technol. A **12**, 2565 (1994).

[67] P.M. Fauchet et al., SPIE Proceedings **2141**, 155 (1994).

[68] D. Schwall, F.A. Otter, J.M. Galligan, Philos. Mag. B **75**, 887 (1997).

[69] Ph. Dumas, M. Gu, C. Syrykh, J.K. Gimzewski, I. Makarenko, A. Halimaoui, and F. Salvan, Europhys. Lett. **23**, 197 (1993).

[70] A. Pavlov, and Y. Pavlova, Thin Solid Films **297**, 132 (1997).

[71] R. Laiho, and A. Pavlov, Phys. Rev. B **51**, R14774 (1995).

[72] R. Laiho, A. Pavlov, and Y. Pavlova, Thin Solid Films **297**, 138 (1997).

[73] E. zur Mühlen, and H. Niehus, Phys. Stat. Sol. (b) **190**, 21 (1995).

[74] O. Teschke, Appl. Phys. Lett. **68**, 2129 (1996).

[75] Y. Tao, R. Laiho, and L. Heikkilä, J. Vac. Sci. Technol. B **12**, 2437 (1994).

[76] Ph. Dumas, M. Gu, C. Syrykh, A. Halimaoui, F. Salvan, J.K. Gimzewski, and R.R. Schlitter, J. Vac. Sci. Technol. B **12**, 2064 (1994).

[77] Ph. Dumas, M. Gu, C. Syrykh, A. Halimaoui, F. Salvan, and J.K Gimzewski, J. Vac. Sci. Technol. B **12**, 2067 (1994).

[78] K. Ito, S. Ohyama, Y. Uehara, and S. Ushioda, Appl. Phys. Lett. **67**, 2536 (1995).

[79] V. Labunov, V. Bondarenko, L. Glinenko, A. Dorofeev, and L. Tabulina, Thin Solid Films 137, 123 (1986).

[80] V. Labunov, V. Bondarenko, V. E. Borisenko, and A. Dorofee, Phys. Stat. Sol. (a) **102**, 193 (1987).

[81] K. Barla, G. Bomchil, R. Herino, J.C. Pfister, and J. Baruchel, J. Cryst. Growth **68**, 721 (1984).

[82] K. Barla, R. Herino, G. Bomchil, J.C. Pfister, and A. Freund, J. Cryst. Growth **68**, 727 (1984).

[83] D. Bellet, and G. Dolino, Thin Solid Films **276**, 1 (1996).

[84] H. Sugiyama, and O. Nittono, Jpn. J. Appl. Phys. **28**, 12013 (1989).

[85] H. Sugiyama, and O. Nittono, J. Cryst. Growth **103**, 156 (1990).

[86] D. Buttard, D. Bellet, and G. Dolino, J. Appl. Phys. **79**, 8060 (1996).

[87] I.M. Young, M.I.J. Beale, and J.D. Benjamin, Appl. Phys. Lett. **46**, 1133 (1985).

[88] K.H. Kim, G. Bai, M.A. Nicolet, and A. Venezia, J. Appl. Phys. **69**, 2201 (1991).

[89] T. Itoh, H. Kiyama, T. Yasumatsu, H. Watanabe, and H. Hiraki, Physica B **170**, 535 (1991).

[90] V. Vezin, P. Goudeau, A. Naudon, A. Halimaoui, and G. Bomchil, J. Appl. Cryst. **24**, 581 (1991).

[91] A. Naudon. P. Goudeau, and V. Vezin, in Ref. [245], p. 255.

[92] B.K. Teo, and D.C. Joy, "EXAFS spectroscopy and related techniques" (Plenum Press, New York, 1981); B.K. Teo. "EXAFS: Basic principles and data analysis" (Springer Verlag, Berlin, Heidelberg, 1986).

[93] J. Stöhr "X-ray absorption. principles, applications, techniques of SEXAFS and XANES" edited by D.C. Koningsberger and R. Prins, Vol. 92, p.443 (John Wiley and Sons, New York 1988).

[94] M. De Crescenzi, M.N. Piancastelli, "Electron scattering and related spectroscopies" (World Scientific Singapore 1996).

[95] G. Dalba, P. Fornasini, M. Grazioli, R. Grisenti, Y. Soldo, F. Rocca, Nucl. Instr. and Meth. (b) **97**, 322 (1995).

[96] S. Schuppler, S.L. Friedman, M. A. Marcus, D.L. Adler, Y.H. Xie, F.M. Ross, T.D. Harris, W.L. Brown, Y.J. Chabal, L.E. Brus, and P.H. Citrin, Phys. Rev. Lett. **72**, 2648 (1994).

[97] S. Schuppler, S.L. Friedman, M.A. Marcus, D.L. Adler, Y.H. Xie, F.M. Ross, Y.J. Chabal, T.D. Harris, L.E. Brus, W.L. Brown, E.E. Chaban, P.F. Szjowski, S.B. Christman, and P.H. Citrin, Phys. Rev. **B52**, 4910 (1995).

[98] T. van Buuren, Y. Gao, T. Tiedje, J.R. Dhan, and B.M. Way, Appl. Phys. Lett. **60**, 3013 (1992).

[99] T. van Buren, T. Tiedje, S.N. Patitsas, and W. Weydanz, Phys. Rev. B **50**, 2719 (1994).

[100] J.R. Dahn, B.M. Way, E.W. Fuller, W.J. Weydanz, J.S. Tse, D.D. Klug, T. Van Buuren, and T. Tiedje, J. Appl. Phys. **75**, 1946 (1994).

[101] Qi Zhang, and S.C. Bayliss, J. Appl. Phys. **79**, 1351 (1996).

[102] S.C. Bayliss, D.A. Hunt, Qi Zhang, N. Danson, and A. Smith, Solid State Commun. **91**, 371 (1994).

[103] T.K. Sham, D.T. Jang, I. Coulthard, J.W. Lorimer, X.H. Feng, K.H. Tang, S.P. Frigo, R.A. Rosenberg, D.C. Houghton, and B. Bryskiewicz, Nature **363**, 331 (1993).

[104] S. Gardelis, U. Bangert, B. Hamilton, R.F. Pettifer, D.A. Hill, R. Keyse, and D. Teehan, Appl. Surf. Sci. **102**, 408 (1996).

[105] R.F. Pettifer, A. Glanfield, S. Gardelis, B. Hamilton, P. Dawson, A.D. Smith, Physica B **208/9**, 484 (1995).

[106] G. Dalba, N. Daldosso, D. Diop, P. Fornasini, R. Grisenti, and F. Rocca, J. Lumin. **80**, 103 (1999).

[107] G. Dalba, P. Fornasini. R. Grisenti, N. Daldosso, and F. Rocca, Appl. Phys. Lett. **74**, 1454 (1999).

[108] G. Dalba, N. Daldosso, P. Fornasini, R. Graziola, R. Grisenti, F. Rocca, J. Non-Cryst. Solids **232-234**, 232 (1998).

[109] W. Lang , in *Properties of porous silicon*, edited by L.T. Canham (IEE INSPEC, London, 1997) p. 138.

[110] G. Gesele, J. Linsmelier, V. Drach, J. Frike, and R. Arens-Fischer, J. Phys. : D **30**, 2911 (1997).

[111] D. Bellet, in *Properties of porous silicon*, edited by L.T. Canham (IEE INSPEC, London, 1997) p. 127.

[112] L.J. Gibson, and M.F. Ashby, in *Cellular solids: structure and properties*, edited by Pergamon Press, (New York, 1988).

[113] K. Barla, R. Herino, G. Bomchil, J.C. Pfister, and A. Freund, J. Cryst. Growth **68**, 727 (1984).

[114] T.H. Metzger et al., in *Properties of porous silicon*, edited by L.T. Canham (IEE INSPEC, London, 1997) p. 112.

[115] G. Dolino, G. Bellet, and C. Faivre, Phys. Rev. B **54**, 17919 (1996).

[116] H. Yoon, and M.S. Goorsky, Mat. Res. Soc. Symp. Proc. **378**, 893 (1995).

[117] T. Ito, T. Yasamatsu, H. Watabe, and A. Hirachi, Jpn. J. Appl. Phys. **29**, 1201 (1990).

[118] D. Buttard, D. Bellet, and G. Dolino, J. Appl. Phys. **79**, 8060 (1996).

[119] G. Dolino, and G. Bellet, in *Properties of porous silicon*, edited by L.T. Canham (IEE INSPEC, London, 1997) p. 118.

[120] S.P. Duttagupta, and M.P. Fauchet, in *Properties of porous silicon*, edited by L.T. Canham (IEE INSPEC, London, 1997) p. 132.

[121] G. Mariotto, F. Ziglio, and F.L. Freire Jr. , J. Non-Cryst. Solids **192/3**, 253 (1995).

[122] H. Richter, Z.P. Wang, and L. Ley, Solid State Commun.**39**, 625 (1981).

[123] I.H. Campbell, and M.P. Fauchet, Solid State Commun. **58**, 739 (1986).

[124] N. Daldosso, F. Rocca, G. Dalba, P. Fornasini, and R. Grisenti, J. Porous Materials (1998).

[125] R. Bomchil, R. Herino, K. Barla, and J.C. Pfister, J. Electrochem Soc. **130**, 1611 (1983).

[126] R. Herino, in Ref. [247] p.89.

[127] S. Braunauer, P.H. Emmett, and E. Teller, J. Am. Chem. Soc. **60**, 309 (1938).

[128] E.P. Barrett, L.G. Joyner, and P.P. Halenda, J. Am. Chem. Soc. **73**, 373 (1951).

[129] A. Halimaoui in Ref. [245] p. 50.

[130] A. Venkateswara, F. Ozanam, and J.N. Chazalviel, J. Electrochem. Soc. **138**, 153 (1991).

[131] A. Grosman, and C. Ortega, in Ref. [247] p. 145.

[132] N. Hadj Zoubir , M. Vergnat, T. Delatour, A. Burneau, and P. de Donato, Appl. Phys.

Lett. **65**, 82 (1994).

[133] L.T. Canham, M.R. Houlton, W.Y. Leong, C. Pickering, and J.M. Keen, J. Appl. Phys. **70**, 422 (1991).

[134] S. Banerjiee, K.L. Narasimhan, and A. Sardesai, Phys. Rev. B **49**, 2915 (1994).

[135] D. Petit, J.N. Chazalviel, F. Ozanam, and F. Devreux, Appl. Phys. Lett. **70**, 191 (1997).

[136] C. Ortega, J. Siejka, and G. Vizkelethy, Nucl. Instrum. Methods. **45**, 622 (1990).

[137] L. Calliari, M. Anderle, M. Ceschini, L. Pavesi, G. Mariotto, and O. Bisi, J. Lumin. **57**, 83 (1993); L. Pavesi, L. Calliari, E. Zanghellini, G. Mariotto, M. Anderle, and O. Bisi, in Ref. [245] p. 61.

[138] H.J. Von Bardeleben, D. Stivenard, A. Grosman, C. Ortega, and J. Siejka, Phys. Rev. B **47**, 10889 (1993).

[139] B. Pivac, B. Rakvin, and L. Pavesi, Appl. Phys. Lett. **65** 3260 (1994).

[140] R.F. Pettifer, A. Glanfield, S. Gardelis, B. Hamilton, P. Dawson, and A.D. Smith, Physica B **208/9**, 484 (1995).

[141] A. Loni, A.J. Simons, L.T. Canham, H.J. Philips, and L.G. Earwaker, J. Appl. Phys. **76**, 2825 (1994).

[142] L. Pavesi, G. Mariotto, O. Bisi, M. Anderle, and L. Calliari, in *Physical Concepts and Materials for Novel Optoelectronic Device Applications II* SPIE Vol. 1985 p. 632 (1993).

[143] L.T. Canham, in Ref. [248] p. 81.

[144] A. Bsiesy, A. Gaspard, R. Herino, M. Ligeon, F. Muller, and J.C. Oberlin, J. Electrochem. Soc. **138**, 3450 (1991).

[145] L.T. Canham in Ref. [247] p. 158 and references therein.

[146] A. Nakajima, T. Itakura, S. Watanabe, and N. Nakayama, Appl. Phys. Lett. **61**, 46 (1992).

[147] X.Y. Hou et al., Appl. Phys. Lett. **62**, 1097 (1992).

[148] T. Giaddui et al., J. Phys. D: Appl. Phys. **29**, 1580 (1996).

[149] S.P. Dattagupta, L. Tsybeskov, P.M. Fauchet, E. Ettedgui, and Y. Gao, Mater. Res. Soc. Symp. Proc. **358**, 381 (1995).

[150] A.C. Dillon, M.B. Robinson, M.Y. Han, and S.M. George, J. Electrochem. Soc **139**, 537 (1992).

[151] J.A. Glass, E.A. Wovchko, and J.T. Yates, Mat. Res. Soc. Symp. Proc. **358**, 537 (1995).

[152] E.J. Lee, J.S. Ha, and M.J. Sailor, Mat. Res. Soc. Symp. Proc. **358**, 387 (1995).

[153] N.Y. Kim, and P.E. Laibinis, J. Am. Chem. Soc. **119**, 2297 (1997).

[154] K.H. Li, C. Tsai, J.C. Campbell, M. Kovar, J.M. White, and J. Electron. Mater. **23**, 409 (1994).

[155] J.L. Coffer, S.C. Lilley, R.A. Martin, and L.A. Files-Sesler, J. Appl. Phys **74**, 2094 (1993).

[156] P.D.J. Calcott, in Ref. [247] p. 203 and references therein.

[157] W. Theiß, Festerkörperprobleme-Advances in Solid State Physics **33**, 149 (1994).

[158] J.C. Maxwell-Garnett, Philos. Trans. R. Soc. Lond. **203**, 385 (1904).

[159] D.A.G. Bruggeman, Ann. Phys. **24**, 636 (1925).

[160] H. Looyenga, Physica **31**, 401 (1965).

[161] L. Pavesi, and V. Mulloni, J. Lumin. (1999).

[162] P.M. Fauchet, L. Tsybeskov, S.P. Duttagupta, and K.D. Hirschman, Thin Solid Films **297**, 254 (1997).

[163] H. Mizuno, H. Koyama, N. Koshida, Appl. Phys. Lett., **69** 3779 (1996).

[164] P.M. Fauchet, J. von Behren, Phys. Stat. Solidi (b) **204**, R7 (1997).

[165] L.T. Canham, Appl. Phys. Lett. **57**, 1046 (1990).

[166] L. Tsybeskov, Y.V. Vandyshev, and P.M. Fauchet, Phys. Rev. B **49**, 7821 (1994).

[167] A. Kux, D. Kovalev, and F. Koch, Appl. Phys. Lett. **66**, 49 (1995); A. Kux, D. Kovalev, and F. Koch, Thin Solid Films **255**, 143 (1995).

[168] P.M. Fauchet, E. Ettedgui, A. Raisanen, L.J. Brillson, F. Seiferth, S.K. Kurinec, Y. Gao, C. Peng, and L. Tsybeskov, Mater. Res. Soc. Symp. Proc. **298**, 271 (1993).

[169] F. Koch, Mater. Res. Soc. Symp. Proc. **298**, 319 (1993).

[170] G. Pfister, and H. Scher, Adv. Phys. **27**, 747 (1978).

[171] H. Scher, M.F. Shlesinger, and J.T. Bendler, Physics Today **44**, 26 (January 1991).

[172] H. Eduardo Roman, and L. Pavesi, J. Phys: Cond. Matter **8**, 5161 (1996).

[173] P.D.J. Calcott, K.J. Nash, L.T. Canham, M.J. Kane, and T. Brumhead, J. Phys. Cond. Matter **5**, L91 (1993).

[174] T. Maruyama, and S. Ohtani, Appl. Phys. Lett. **65**, 1346 (1994).

[175] F. Muller, R. Herino, M. Ligeon, F. Gaspard, R. Romestein, J-C. Vial, and A. Bsiesy, J. Lumin. **57**, 283 (1993); I. Mihalcescu, F. Muller, R. Romestein, and J.-C. Vial, J. Lumin. **57**, 111 (1993).

[176] S. Shih, C. Tsai, H.K. Li, K.H. Jung, J.C. Campbell, and D.L. Kwong, Appl. Phys. Lett. **60**, 633 (1992).

[177] V. Petrova-Koch, T. Muschik, A. Kux, B.K. Meyer, F. Koch, and V. Lehmann, Appl. Phys. Lett. **61**, 943 (1992).

[178] H.J. Von Bardeleben, C. Ortega, A. Grosman, V. Morazzani, J. Siejka, and D. Stivenard, J. Lumin. **57**, 301 (1993).

[179] M.A. Tischler, R.T. Collins, J.H. Stathis, and J.C. Tsang, Appl. Phys. Lett. **60**, 639 (1992).

[180] R. Czaputa, R. Friztl, and A. Popitsch, Thin Solid Films **255**, 212 (1995).

[181] M. Born, and E. Wolf, *Principle of Optics*, (Pergamon, Oxford, 1980).

[182] C. Weisbuch, Proceedings of the 22th International Conference on the Physics of Semiconductors, ed. D.J. Lockwood (World Scientific Publishing Co, Singapore 1995) p. 1839.

[183] S. Haroche, and D. Kleppner, Physics Today, January 1989 p. 24.

[184] E.M. Purcell, Phys. Rev. B **69**, 681 (1946).

[185] G. Bjork, and Y. Yamamoto, in *Spontaneous Emission and Laser Oscillation in Microcavities*, ed. H. Yokoyama and K. Ujihara (CRC Press, London 1995), p. 189.

[186] L. Pavesi, R. Guardini, and C. Mazzoleni, Sol. State. Comm. **97**, 1051 (1996).

[187] L. Pavesi, C. Mazzoleni, R. Guardini, M. Cazzanelli, V. Pellegrini, and A. Tredicucci, Il Nuovo Cimento **18 D**, 1213 (1996).

[188] E. Yablonovitch, J. Opt. Soc. Am. **B 10**, 283 (1993).

[189] Y. Yamamoto, S. Machida, K. Igeta, and G. Björk, in *Coherence, Amplification and Quantum Effects in Semiconductor Lasers*, ed. by Y. Yamamoto (John Wiley and Sons, New York 1991) p. 561.

[190] V. Savona, C. Piermarocchi, A. Quattropani, P. Schwendimann, and F. Tassone, in

New aspects in Optical Properties of Nanostructures, special issue of Phase Transitions (1998).

[191] J.F. McGilp, Prog. in Surf. Sci. **49**, 1 (1995).

[192] St. Frohnhoff, M.G. Berger, M. Thonissen, C. Dieker, L. Vescan, H. Munder, and H. Luth, Thin Sol. Films **255**, 59 (1995).

[193] G. Vincent, Appl. Phys. Lett. **64**, 2367 (1994).

[194] M. G. Berger, C. Dieker, M. Thonissen, L. Vescan, H. Luth, H. Munder, W. Theiß, M. Wernke, and P. Grosse, J. Phys. D: Appl. Phys. **27**, 1333 (1994).

[195] M. Cazzanelli, Tesi di Laurea, Universitá degli Studi di Trento, unpublished (1996).

[196] S. Frohnhoff, and M. Berger, Adv. Mater. **12**, 963 (1994).

[197] M.G. Berger, R. Arens-Fisher, M. Thonissen, M. Kruger, S. Billat, H. Luth, S. Hilbrich, W. Theiss, and P. Grosse, Thin Sol. Films **297**, 237 (1997).

[198] C. Mazzoleni, and L. Pavesi, Appl. Phys. Lett. **67**, 2983 (1995).

[199] L. Pavesi, C. Mazzoleni, A. Tredicucci, and V. Pellegrini, Appl. Phys. Lett. **67**, 3280 (1995).

[200] M.G. Berger, M. Thonissen, R. Arens-Fisher, H. Munder, H. Lutz, M. Arntzen, and W. Theiß, Thin Solid Films **255**, 313 (1995).

[201] L. Pavesi, G. Giebel, F. Ziglio, G. Mariotto, F. Priolo, S.U. Campisano, and C. Spinella, Appl. Phys. Lett. **65**, 2182 (1994).

[202] M.G. Berger, R. Arens-Fisher, S. Frohnhoff, C. Dieker, K. Winz, H. Munder, H. Luth, M. Artzen, W. Theiss, Mat. Res. Soc. Symp. Proc. Vol. 358, 327 (1995).

[203] V. Pellegrini, A. Tredicucci, C. Mazzoleni, and L. Pavesi, Phys. Rev. B **52**, R14328 (1995).

[204] M. Thönissen, M.G. Berger, M. Kruger, W. Theiss, S. Hilbrich, R. Arens-Fisher, S. Billat, and H. Luth, Mat. Res. Soc. Symp. Proc. **45**, 643 (1997).

[205] G. Lerondel, P. Ferrand, and R. Romestain, Mat. Res. Soc. Symp. Proc. Vol. 452, 711 (1997).

[206] M. Araki, H. Koyama, and N. Koshida, Jpn. J. Appl. Phys. **35** 2B, 1041 (1996).

[207] V. Savona, L. C. Andreani, P. Schwendimann, and A. Quattropani, Solid State Commun. **93**, 733 (1995).

[208] Y. Yamamoto, S. Machida, and G. Björk, Surface Science **267**, 605 (1992).

[209] A. Tredicucci, Y. Chen, V. Pellegrini, and C. Deparis, Appl. Phys. Lett. **66**, 2388 (1995).

[210] J.C. Vial, A. Bsiesy, F. Gaspard, R. Herino, M. Ligeon, F. Muller, R. Romestain, and R.M. Macfarlane, Phys. Rev. B **45**, 14171 (1992).

[211] M. Cazzanelli, C. Vinegoni, and L. Pavesi, J. Appl. Phys. **85**, 1760 (1999).

[212] V. Mulloni, C. Mazzoleni, and L. Pavesi, unpublished.

[213] L. Pavesi, G. Panzarini, and L.C. Andreani, Phys. Rev. B **58**, 15794 (1998).

[214] C. Delerue, M. Lannoo, and G. Allan, J. of Lumin. **57**, 249 (1993).

[215] L. Pavesi, M. Cazzanelli, and O. Bisi, Mat. Res. Soc. Symp. Proc. Vol. 452, 717 (1997); M. Cazzanelli, and L. Pavesi, Phys. Rev. B **56** 15264 (1998).

[216] D.I. Babic and S.W. Corzine, IEEE J. Quantum Electr. **28**, 514 (1992).

[217] E. Snoeks, A. Lagendijk, and A. Polman, Phys. Rev. Lett. **74**, 2459 (1995).

[218] R.P. Stanley, R. Houdré, U. Oesterle, M. Ilegems, and C. Weisbuch, Appl. Phys. Lett. **65** 2093 (1994).

[219] P. Michler, M. Hilpert, and G. Reiner, Appl. Phs. lett. **70** 2073 (1997).

[220] P. Pellandini, R.P. Stanley, R. Houdré, U. Oesterle, M. Ilegems, and C. Weisbuch, Appl. Phys. Lett. **71** 864 (1997).

[221] A. Armitage *et al.* (unpublished).

[222] M. Cazzanelli, and L. Pavesi, Phys. Rev. B **56** 15264 (1997).

[223] H.A. McLeod, *Thin-Film Optical Filters*, 2nd ed. (Hilger, London, 1986).

[224] B. Delley, and E.F. Steigmeier, Phys. Rev. B **47**, 1397 (1993).

[225] A. Loni, L.T. Canham, M.G. Berger, R. Arens-Fischer, H. Munder, H. Luth, H.F. Arrand, and T.M. Benson, Thin Solid Films **276**, 143 (1996).

[226] M. Araki, H. Koyama, and N. Koshida, Appl. Phys. Lett. **68**, 2999 (1996).

[227] S. Lazarouk, P. Jaguiro, and V. Borisenko, Phys. Stat. Sol. (a) (to be published 1999).

[228] G. Mattei, A. Marucci, and V. A. Yakovlev, Mat. Sci & Eng. **B51**, 158 (1998).

[229] A. Fainstein, B. Jusserand, and V. Thierry-Mieg, Phys. Rev. Lett. **75**, 3764 (1995).

[230] V. Dneprovskii, A. Eev, N. Gushina, D. Okorokov, V. Panov, V. Karavanskii, A. Maslov, V. Sokolov, and E. Dovidenko, Phys. Stat. Sol. (b) **188**, 297 (1995).

[231] L.A. Golavan et al., JETP Letters, **69** 300 (1999).

[232] E.F. Schubert, Y.H. Wang, A.Y. Cho, L.W. Tu, and G.J. Zydzik, Appl. Phys. Lett. **60**, 921 (1992).

[233] E.F. Schubert, N.E.J. Hunt, M. Micovic, R.J. Malik, D.L. Sivco, A.Y. Cho, and G.J. Zydzik, Science **265**, 943 (1994).

[234] M. Selim Unlu, and S. Strite, J. Appl. Phys. **78**, 607 (1995).

[235] M. Araki, H. Koyama, and N. Koshida, Appl. Phys. Lett. **69**, 2956 (1996).

[236] W. Lang, P. Steiner, and F. Kozlowski, J. Lumin. **57**, 341 (1993).

[237] D. Zhang, Z. Li, W. Hu, and B. Cheng, Appl. Phys. Lett. **67**, 2431 (1995).

[238] A. Loni, A.J. Simmons, T.I. Cox, P.D.J. Calcott, and L.T. Canham, El. Lett. **31**, 1288 (1995).

[239] S. Lazarouk, P. Jaguiro, S. Katsouba, G. Masini, S. La Monica, G. Maiello, and A. Ferrari, Appl. Phys. Lett. **68**, 2108 (1996).

[240] K.D. Hirschmann, D. Tsybeskov, S.P. Duttagupta, P.M. Fauchet, Nature **384**, 338 (1996).

[241] S. Hilbrich, R. Arens-Fisher, L. Kupper, W. Theiss, M.G. Berger, M. Kurger, and M. Thonissen, Thin Solid Films **297**, 250 (1997).

[242] W. Theiß, R. Arens-Fisher, S. Hilbrich, D. Scheyen, M.G. Berger, M. Kruger, and M. Thonissen, Mat. Res. Soc. Symp. Proc. Vol. 452, 637 (1997).

[243] M. Kruger, M. Marso, M.G. Berger, M. Thonissen, S. Billat, R. Loo, W. Reetz, H. Luth, S. Hilbrich, R. Arens-Fischer, and P. Grosse, Thin Solid Films **297**, 241 (1997).

[244] M. Araki, H. Koyama, and N. Koshida, J. Appl. Phys. **80**, 4841 (1996).

[245] *Porous Silicon Science and Technology*, edited by J.C. Vial, and J. Derrien (Les Editions de Physique, Paris 1995).

[246] *Porous Silicon*, edited by Zhe Chuan Feng, and R. Tsu (World Scientific Publishing Co., New York 1995).

[247] *Properties of Porous Silicon*, ed by L. T. Canham (IEE INSPEC, The Institution of Electrical Engineers, London 1997).

[248] *Optical properties of low dimensional silicon structures*, edited by D.C. Benshael, L.T. Canham, and S. Ossicini, NATO ASI Series Vol. 244 (Kluwer Academic Publisher,

Dordrecht 1993).

FIGURES

FIG. 1. Schematic drawing of the electrochemical cell used for the preparation of porous silicon. Adapted from Ref. [5].

FIG. 2. Cross sectional view of a lateral anodization cell. The silicon wafer acts as the anode. Reprinted with permission after Ref. [7].

FIG. 3. Cross sectional view of a double tank anodization cell. The Si wafer is used to separate the two half-cells. Reprinted with permission after Ref. [7].

FIG. 4. Characteristic i-V curves for n- and p-type doped Si in aqueous HF. Reprinted with permission after Ref. [8].

FIG. 5. Dissolution mechanism proposed by V. Lehmann and U. Gösele [15]. Reprinted with permission after Ref. [16].

FIG. 6. Pore formation in PS. On the top is shown the initial stage, where the pores develop randomly on the Si surface. In the middle panel it is shown the self-regulating process. When the depletion zones around each pore overlap, the pore growth changes from an isotropic growth to a highly directional growth. On the bottom panel it is shown how the dissolution advances only at the pore tips. Reprinted with permission after Ref. [17].

FIG. 7. Depth profile of the hole, left after dissolution, of the PS layer formed on a 7 Ωcm substrate. The profile is taken on a diameter. The depths were determined by scanning electron microscopy measurements. Reprinted with permission after Ref. [2].

FIG. 8. Porosity as a function of the current densities for different HF concentrations. In the top panel, for lightly doped, and in the bottom panel for highly doped, p-type silicon substrate. Reprinted with permission after Ref. [2,19] and [7] respectively.

FIG. 9. Cross sectional SEM image of a typical cracking pattern. Reprinted with permission after Ref. [16].

108

FIG. 10. Stress-time evolution during the drying process of PS. Figure (a) and (b) refers respectively to two different cycles. Reprinted with permission after Ref. [23].

FIG. 11. Schematic phase diagram showing pressure-temperature paths used in supercritical drying. Reprinted with permission after Ref. [16].

FIG. 12. Ideal representation of a porous silicon layer. On the left part is shown the etched array of voids in silicon. On the right panel is shown an enlarged area of the PS laye, where the silicon nanocrystals are embedded in an amorphous matrix. Adapted from Ref. [25].

FIG. 13. Cross-sectional TEM images showing the basic differences in morphology among different types of samples. (a) p-type silicon (b) n-type silicon (c) p^+-type silicon (d) n^+-type silicon. Reprinted with permission after Ref. [8].

FIG. 14. On the top panel is reported the thermal conductivity λ_{PS} for PS layers of thickness of about 31 μm and for different porosities. On the bottom panel is reported the thermal conductivity λ_{PS} for PS layers with different substrate: p^+ (circles) and p^- (triangles) type doped silicon with PS porosity equal to 64%. Reprinted with permission after Ref. [110].

FIG. 15. Young modulus values of p^+-type PS samples reported as a function of the relative density. X-ray measurements (filled diamond), acoustic wave propagation (filled triangle), nanoindentation technique (filled square) and Brillouin spectroscopy (filled circle). Reprinted with permission after Ref. [111].

FIG. 16. Intensity distribution near the (004) Bragg reflection a p^+-type sample. Open circles represents the experimental data, which consist of two different contribution; the substrate peak (c-Si) and the expanded lattice of PS layer (por-Si). The solid line is the sum of the two contributions (dashed line). Reprinted with permission after Ref. [114].

FIG. 17. The variation of lattice mismatch vs. porosity of p^+-type PS layer, is reported in three different investigations. Reprinted with permission after Ref. [115].

FIG. 18. In the figure it is reported the hardness vs. the porosity for PS films. The p^+-type samples are represented by filled circles, and p^--type samples by filled square. The applied load corresponds to 0.49 N. The solid line represents the $H_0(1-P)^{2/3}$ term, where H_0 is the hardness of crystalline silicon (11.5 GPa). Reprinted with permission after Ref. [120].

FIG. 19. Schematic representation of a nitrogen adsorption isotherm at 77 K for a PS layer formed on heavily doped p-type substrate. Reprinted with permission after Ref. [126].

FIG. 20. Specific surface area as a function of the PS porosity. Data of PS with porosity of 51 % (dot) and 65 % (square). The layer thickness is equal to 1 μm. Reprinted with permission after Ref. [129].

FIG. 21. IR absorption spectrum at the temperature of 8 K for a free-standing p^+-type PS in the Si-H stretch mode. The thickness is 89 μm and the porosity 50%. The lines that corresponds to O_x-Si-H groups (around 2200-2250 cm^{-1}) are absent ; note the presence of Si-O-Si groups around 1065 cm^{-1}. The visible oscillations are interference fringes that originate at the PS/air interfaces. Adapted from Ref. [131].

FIG. 22. Room temperature EPR spectrum of a (100) 11 μm thick n^+-type PS sample. The magnetic field is in the (110) plane parallel to the [001] orientation. In the inset is show the EPR spectrum of the Pb centers. The large signal due to free carriers was subtracted. Adapted from Ref. [131].

FIG. 23. EPR samples irradiated by 10 Mrad γ rays from ^{60}Co source (A), annealed at 450 °C for 15 min. in N_2 before irradiation (B), exposed to molecular hydrogen at room temperature for 30 min. after annealing and irradiation (C). Reprinted with permission after Ref. [139].

FIG. 24. Auger spectrum of a freshly etched PS sample. In the inset is shown the comparison between an aged (dotted line) and a freshly etched (solid line) sample. Reprinted with permission after Ref. [142]

FIG. 25. Idealized schematic steps in the oxidation process of highly porous silicon. Reprinted with permission after Ref. [143].

FIG. 26. Normal-incidence reflectance spectrum of a 75 % porosity sample 6.8 μm thick. Reprinted with permission after Ref. [2].

FIG. 27. Refractive index as a function of current density and porosity for two different substrate doping levels. Adapted from Ref. [161].

FIG. 28. Room temperature photoluminescence and electroluminescence spectra for various PS structure which have been oxidized or implanted with some selected impurities. Reprinted with permission after Ref. [162].

FIG. 29. The red (R), green (G) and blue (B) photoluminescence spectra (PL) tuned by post-anodization illumination (dashed curve) and the corresponding excitation spectra (PLE). Adapted from Ref. [163].

FIG. 30. Plot of the photoluminescence peak wavelength and the intensity versus the sample porosity. The thick line is obtained from first-principle calculations. Reprinted with permission after Ref. [164].

FIG. 31. Room temperature luminescence spectra of PS samples with different porosities after six months aging. The excitation energy is 2.541 eV and the power density is 1.6 Wcm^{-2}. Reprinted with permission after Ref. [2].

FIG. 32. Plot of the energy position of the S band (named VIS) versus the energy position of the IR band as measured by various authors. The lines are theoretical calculation. Adapted from Ref. [169].

FIG. 33. Time decay of the luminescence of a 60% porosity sample at three temperatures and for an excitation energy of 2.541 eV and observation energy of 1.860 eV. The lines trough the data are least square fit with stretched exponential decays. Adapted from Ref. [25].

FIG. 34. PL spectra from a PS layer with 77% porosity and thickness 11.6 μm for different aging times. Reprinted with permission after Ref. [143].

FIG. 35. Dangling bond (P_b) concentration and luminescence intensity versus the annealing time at the temperature of 1000 °C in oxygen. Adapted from Ref. [178].

FIG. 36. On the left part of the figure it is shown the reflection and transmission of light by a single thin film. On the right in the case of a multilayer. Reprinted with permission after Ref. [2].

FIG. 37. Plot of the Airy function for three different values of the reflectivity R as a function of the phase angle Δ. Reprinted with permission after Ref. [2].

FIG. 38. Simulation of the reflectance spectra of DBR formed by a different number of periods. The high and low refractive indexes have the values 1.5 and 1.27, which correspond to typical PS porosities. Reprinted with permission after Ref. [2].

FIG. 39. Simulation of the reflectance spectra of DBR formed by a different ratio between the high and low refractive indices. Reprinted with permission after Ref. [2].

FIG. 40. Simple diagram of the structure of a FP formed by PS. Reprinted with permission after Ref. [2].

FIG. 41. Simulations of the reflectance spectra for various FP formed by a different number of periods in the DBR. Lower and higher refractive index value are respectively 1.27 and 1.5. The FP is symmetric. Reprinted with permission after Ref. [2].

FIG. 42. Simulation of the reflectance spectra for a FP formed by different ratio ratio between high and low refractive indexes of the DBR. The low refractive index value is 1.27 for all the curves. Instead the high refractive index value is 2.24 (full line), 1.86 (dashed line) and 1.5 (dotted line). The DBR are formed by 4 periods. Reprinted with permission after Ref. [2].

FIG. 43. In the figure it is reported a schematic diagram of the effects of quantization on the electronic density of states (left) and photon density mode (right). Reprinted with permission after Ref. [182].

FIG. 44. Outline of the various competing modes in a microcavity. Reprinted with permission after Ref. [2].

FIG. 45. Comparison of the porosity as deduced by gravimetric measurements with the one deduced by optical measurements. Reprinted with permission after Ref. [2].

FIG. 46. Normal incidence reflectance spectrum of a Si wafer (top) and the deduced refractive index (bottom). Reprinted with permission after Ref. [2].

FIG. 47. Normal incidencence reflectance spectrum of a 75% porosity sample with a thickness of 6.8 μm. The arrows indicate the fringe position and the refractive index value as deduced with Eq. 38. Reprinted with permission after Ref. [2].

FIG. 48. Plot of the refractive index versus the wavelength for different porosity samples obtained via Eq. 38. Reprinted with permission after Ref. [2].

FIG. 49. Schematic sketch of the formation principle of a PS multilayer structure. On the left it is shown the time dependence of the current density. On the right, the actual layer sequence. Adapted from Ref. [196].

FIG. 50. Diagram of a FP structure (left) and of the corresponding porosity and refractive index sequence respectively (right). Reprinted with permission after Ref. [2].

FIG. 51. Effective refractive index at 12000 cm^{-1} (a) and etch rate (b) plotted as a function of the anodization current density for two substrate doping levels. Reprinted with permission after Ref. [197].

FIG. 52. Porosity dependence on the current density for various volumetric HF concentrations ([HF]). The resistivity of the substrate is 0.01 Ω cm. Reprinted with permission after Ref. [2].

FIG. 53. Etch rate versus etch current density for various volumetric HF concentrations and for a substrate resistivity of 0.01 Ωcm. Reprinted with permission after Ref. [2].

FIG. 54. Transmission electron microscopy cross section of a PS multilayer formed on a p-type doped substrate (0.2 Ωcm). Layers I: 64 % porosity and 20 nm thickness; layers II: 84 % porosity and 200 nm thickness. Reprinted with permission after Ref. [194].

FIG. 55. Experimental and simulated $\theta - 2\theta$ diffraction patterns, plotted on a semi-logarithmic scale, around the (004) reflection of a PS multilayer composed of 10 periods of a 36 % porosity and 112 nm thickness layer and 60 % porosity and 73 nm thickness layer. (P) and (S) are the Bragg peaks of the PS multilayer and of the substrate respectively. Adapted from Ref. [86].

FIG. 56. Transmission electron microscopy cross-section of a porosity multilayer obtained on a periodically doped substrate. Reprinted with permission after Ref. [202].

FIG. 57. Normal incidence reflectance spectra of various DBR at room temperature. The panel (a) refers to a DBR centered at a wavelength $\lambda = 670$ nm and made by 15 repetitions of two layers of 62 and 75 % porosities, respectively. The panel (b) refers to a DBR centered at λ= 590 nm and made by 15 repetitions of 62/75 % porosity layers. Panel (c) refers to a DBR with the same structure as that of panel (b) but with a larger number of repetitions: 30. Panel (d) refers to a DBR centered at λ= 465 nm and made by 15 repetitions of 62/75 % porosity layers. Reprinted with permission after Ref. [198].

FIG. 58. Normal incidence reflectance spectra of various DBR at room temperature. The DBR differ only for the number of periods. All are centered at λ= 590 nm and made by different repetitions (5 (a), 8 (b), 15 (c), 30 (d)) of 62/75 % porosity layers. Reprinted with permission after Ref. [2].

FIG. 59. Reflectance spectra of various DBR whose after formation were thermal oxidized in dry O_2 at 950 ^{o}C for 5 min. Reprinted with permission after Ref. [197].

FIG. 60. Room temperature reflectance spectra of random DBR centered at λ=800 nm. The insets show the histogram of the times used to etch the various low porosity layers whose form the DBR. The different spectra correspond to different standard deviation σ of the gaussian distribution according to which the times are dispersed. Reprinted with permission after Ref. [3].

FIG. 61. Room temperature reflectance spectra of random DBR centered at λ=570 nm (first three spectra starting from the top) and at λ=800 nm (last two spectra). The insets show the histogram of the times used to etch the various low porosity layers. The first three spectra correspond to different ordering of the same layer distribution: random ordering (top spectrum), increasing thickness ordering (second spectrum) and decreasing thickness ordering (third spectrum). The other two spectra correspond to an increasing thickness sequence (which is different from the one used in the first three spectra) where the first layer on the air-side was a high refractive index layer (fourth spectrum) or a low refractive index layer (fifth spectrum). Reprinted with permission after Ref. [3].

FIG. 62. Room temperature reflectance spectra of random DBR centered at λ=800 nm for various number of random layer (i.e. periods) indicated. The insets show the histogram of the times used to etch the various low porosity layers. For the case of 20 layers, two different DBR with different random sequences are presented. Reprinted with permission after Ref. [3].

FIG: 63. Room temperature normal incidence reflectance spectra of various FP whose characteristics are reported in table VIII. All the FP have a symmetric structure made by two DBR separated by a $\lambda/2$ thick central layer of 75 % porosity. λ is the wavelength of the FP transmittance wavelength. Panel (a) refers to a FP with $\lambda = 533$ nm and with DBR formed by 8 repetitions of two $\lambda/4$ thick layers of 62 and 75 % porosities, respectively. Panel (b) refers to a FP with $\lambda = 629$ nm and with DBR formed by 8 repetitions of 62/75 % porosity $\lambda/4$ layers. Panel (c) refers to a FP with $\lambda = 731$ nm and with DBR formed by 6 repetitions of 62/75 % porosity $\lambda/4$ layers. Panel (d) refers to a FP with $\lambda = 782$ nm and with DBR formed by 6 repetitions of 62/75 % porosity $\lambda/4$ layers. Reprinted with permission after Ref. [198].

FIG. 64. Room temperature normal incidence photoluminescence spectra of PS samples. Panel (a) refers to a 5 μm thick 75 % porosity sample. Panel (b) refers to a sample constituted by a FP centered at 710 nm on top of a 5 μm thick 75 % porous layer. The FP finesse is 46. Panel (c) refers to a FP centered at 828 nm and with a finesse of 49 on top of a 2 μm thick 75 % porous layer. Panel (d) refers to a FP centered at 941 nm and with a finesse of 47 on top of a 2 μm thick 75 % porous layer. The arrows indicate the FP λ. All the FP have a same structure formed by two equal DBR separated by a $\lambda/2$ thick and 53 % porosity central layer. The DBR are made by 6 repetitions of two $\lambda/4$ thick layers of 53 % and 75 % porosities, respectively. The FP finesse has been determined by independent reflectance measurements. Reprinted with permission after Ref. [198] and Ref. [198].

FIG. 65. Room temperature reflectance of FP formed by using random DBR. The inset shows the histogram of the times used to etch the various low porosity layers in the two DBR. Reprinted with permission after Ref. [3].

FIG. 66. Room temperature luminescence spectra of various random FP. The top panel refers to two samples equal except for the actual random number sequence. The central panel shows the luminescence of the same three samples whose reflectance is shown in Fig. 65. The bottom panel shows the luminescence of three samples for increasing number of periods (N) in the DBR. The luminescence spectra are horizontally shifted by small amounts (less than 10 nm) in order to let coincide the wavelength of the maximum. The various luminescence spectra are normalized to their maximum and have the intensities whose are not comparable among them except for those of the top panel. Reprinted with permission after Ref. [3].

FIG. 67. Room temperature luminescence spectrum of a random FP. Reprinted with permission after Ref. [3].

FIG. 68. Depth profile of the refractive index (a) and the reflectance spectrum (b) of a Rugate filter formed on a p-type doped substrate. For comparison the reflectance spectrum of a DBR is shown. Reprinted with permission after Ref. [197].

FIG. 69. Room-temperature photoluminescence spectra of a λ-thick porous silicon microcavity PSM (solid line), of a λ-thick porous silicon reference layer (dotted line) and of a sample composed by 12 periods of $\lambda/4$-thick porous silicon layers with alternating porosities of 62% and 45% (dashed line). The PL spectra were collected along the axis normal to the sample surface. In order to compare the various PL lineshapes the emission of the Bragg reflector and of the reference sample has been multiplied by a factor of 10. Reprinted with permission after Ref. [199].

FIG. 70. Experimental arrangement for the collection of the PSM luminescence. Reprinted with permission after Ref. [2].

FIG. 71. Room-temperature luminescence spectra of the λ-thick PSM as a function of the observation angle. The sensitivity factors are reported. Reprinted with permission after Ref. [2].

FIG. 72. Room-temperature radiation pattern corresponding to the λ-thick PSM. The reported values were obtained normalizing the observed intensities to the corresponding excitation intensities and the photoluminescence intensities of the λ-thick porous silicon reference layer. Reprinted with permission after Ref. [199].

FIG. 73. Photoluminescence spectra of the λ (solid lines) and λ/2 (dotted lines) porous silicon microcavities at 30 K and at room temperature (the stronger emissions correspond to 30 K). The inset shows the temperature dependence of the photoluminescence integrated emission of the λ (dashed line) and λ/2 (dotted line) microcavities and of a reference PS λ-thick sample (solid line) normalized to the corresponding lowest temperature photoluminescence integrated spectra. Reprinted with permission after Ref. [203].

FIG. 74. Evolution of the photoluminescence spectrum over a period of six months for a p⁻ PSM with six periods for each mirror. The central peak slightly broadens, while the raise in intensity is more than one order of magnitude. The inset reports Δλ (filled square) and the central wavelength (open circle) as a function of time for the same PSM. Reprinted with permission after Ref. [212]

FIG. 75. Reflectivity spectra of the same PSM shown in Fig. 74. Solid line: freshly etched. Dashed line: six months old. The arrows indicate the cavity wavelength. The PSM spectrum maintains its original features, but shifts to higher energies. Reprinted with permission after Ref. [212]

FIG. 76. Photoluminescence spectra of a typical PSM with eight periods for each mirror and a reference PS layer. Right panel: freshly etched PSM. The FWHM of the central peak is 9 nm. Left panel: the same PSM after six months. The FWHM is 10 nm (gaussian fit). Reprinted with permission after Ref. [212]

FIG. 77. Calculated reflectivity spectra (upper panel) and absorption spectra (lower panel) for a λ porous silicon microcavity. It is also shown the calculated absorption spectra (dotted line) for a λ porous silicon layer without any reflectors. The best matching with the experimental results (Fig. 73) has been obtained with a broadening factor $\Gamma = 30$ meV and with an oscillator strength $4\pi f = 1 \cdot 10^{-4}$. Reprinted with permission after Ref. [203].

FIG. 78. Time resolved luminescence taken at room temperature for the $\lambda/2$ PSM. The time interval between the spectra is 25 μs. Each spectrum has been integrated for 25 μs. 0 μs coincides with the excitation laser pulse. The different spectra are vertically displaced for clarity. Reprinted with permission after Ref. [2]

FIG. 79. Room temperature time decay of the luminescence for the $\lambda/2$ PSM (dots) and the reference PS sample (line) at the PSM resonance wavelength. Reprinted with permission after Ref. [2].

FIG. 80. Wavelength dependence of the τ and β parameters extracted with a stretched exponential fit of the luminescence decays for the $\lambda/2$ PSM and the reference sample. Reprinted with permission after Ref. [2].

FIG. 81. In the figure it is plotted the room temperature time integrated luminescence spectra of the $\lambda/2$ PSM for different excitation powers (indicated on the left in units of I_0=500 W/cm^2). The spectra are vertically displaced for clarity. Reprinted with permission after Ref. [2].

FIG. 82. The observation angle (ϕ) dependence of the luminescence maximum wavelength (λ_c) and of the τ and β parameters for the $\lambda/2$ PSM. Φ is calculated with respect to the normal to the microcavity surface. The subscripts to the τ and β labels refer to the wavelength given in nm. Reprinted with permission after Ref. [2].

FIG. 83. Plot of the room temperature reflectance spectra of PSM with different porosities (labeled as PSM NN %) for the central layer. As a reference the reflectance of a DBR obtained by using the same etching parameters as those for the PSM mirrors is reported in the top panel. Reprinted with permission after Ref. [2].

FIG. 84. Plot of the room temperature luminescence spectra of PSM with different porosities (labeled as PSM NN %) for the central layer. For each PSM NN % spectrum (line) the corresponding spectrum for a porous layer of porosity NN % is reported as dotted line after multiplication by the factor indicated on the left. For a comparison the luminescence of a dielectric Bragg reflector obtained by using the same etching parameters as those for the PSM mirrors is reported in the top panel. The spectra are in relative units. Reprinted with permission after Ref. [2].

FIG. 85. Effective refractive index dependence of $1/\tau$. The various symbols refers respectively to: triangles reference samples, squares DBR, discs PSM. All the data correspond to the resonance wavelength of the PSM. See table XII. Adapted from Ref. [215].

FIG. 86. Photoluminescence as a function of temperature for sample A. The spectra have been shifted for clarity. The horizontal line is the baseline for each spectrum. The measurement temperatures are given on the right. Reprinted with permission after Ref. [211]

FIG. 87. Summary of the temperature dependence of some parameters extracted from the luminescence of sample A. The top panel reports the peak intensity of the cavity mode, the central panel the spectral position and the bottom panel the full width at half maximum. Reprinted with permission after Ref. [211]

FIG. 88. Comparison of the photoluminescence intensity ratio of a PSM (sample B) and of a reference PS sample as a function of the temperature, at the cavity emission wavelength. The inset shows the bare data for the reference PS sample (circles) and the PSM (triangles). Reprinted with permission after Ref. [211]

FIG. 89. Temperature dependence of the luminescence decay time at the wavelength of the cavity mode (λ_c) for the PS (empty squares) and the PSM sample (filled circles) as deduced from a stretched exponential fit of the experimental decays. The lines are fits with Eq. (4), which yields the parameters reported in Table I. The inset shows the ratio between the lifetimes of PSM (τ_{PSM}) and of PS (τ_{ps}). The horizontal line indicates the 2/3, which is the value theoretically expected for ideal microcavities. Reprinted with permission after Ref. [211]

FIG. 90. Incident intensity dependence of the luminescence spectrum of sample B. The various spectra have been normalized to their maximum. The temperature was 300 K. The excitation area was 3×10^{-4} cm^3. Reprinted with permission after Ref. [211]

FIG. 91. Incident intensity dependence of the photoluminescence peak intensity at the cavity mode for the various temperatures indicated on the figure. The intensity has been normalized to the maximum intensity used. Reprinted with permission after Ref. [211]

FIG. 92. Temperature dependence of the α exponent defined with the formula given in the figure, where I_{PL} is the cavity wavelength and J_{exc} the excitation intensity. The PSM sample B has been used. The inset shows the result of the simple model described in Sec. IV. The dashed line is the transmission coefficient T, the dotted line the luminescence from the mirror and the full line the total luminescence intensity. The squares refer to the result of a power law fit with $\alpha = 0.84$. Reprinted with permission after Ref. [211].

FIG. 93. Schematic sketch of the coupled microcavity structure. Adapted from Ref. [213].

FIG. 94. Reflectance spectrum of the balanced all-porous silicon-coupled microcavity (sample a). The arrows point to the cavity modes. Adapted from Ref. [213].

FIG. 95. Luminescence spectra of the coupled microcavities for the various thicknesses of the cavity layers indicated on the left. The spectra are in relative units. The dotted line in the central panel refers to a luminescence spectrum of a reference PS sample grown with the same etching parameters as the cavity layers. The spectrum has been normalized to its maximum and should be multiplied by a factor 0.09 to be reduced to the same relative units of the spectrum of the PSM. Adapted from Ref. [213].

FIG. 96. Absorption of a balanced coupled microcavity as a function of the parameter β. The structure is the same as that used experimentally in Fig. 94; parameters of the calculation are given in the text. Adapted from Ref. [213].

FIG. 97. (a) Absorption and (b) reflectivity spectra of the coupled microcavities for the same structures used in Fig. 95. Dotted curve in upper (lower) panel in (a): refractive indexes reduced (increased) by 5% (3%). The labels on the spectra refer to the name of the various samples. Adapted from Ref. [213].

FIG. 98. Enhancement of the absorption band of the Si-H vibration around 2088 cm^{-1} as a function of the frequency position of the microcavity mode. The black squares are the experimental data while the dotted line is a fitting curve. Adapted from Ref. [228]

FIG. 99. Normal incidence reflectivity spectra of a PSM for two different cw incident pump powers (at 514.5 nm). The dashed line is for 80 kW/cm^2, while the solid line is for no pump power. The inset shows the pump power dependence of the reflectivity at a fixed observation wavelength. Reprinted with permission after Ref. [187].

FIG. 100. Electroluminescence intensity vs. current (EL-I) curve of a RCLED. Both curves are measured for forward bias (top metal contact negative). The inset shows the EL-I data of the RCLED and of a standard metal/PS LED measured at a fixed voltage as a function of time. In the inset the time goes clock-wise. Reprinted with permission after Ref. [187].

FIG. 101. Schematic structure of the RCLED based on a metal/PS microcavity. Adapted from Ref. [235].

FIG. 102. Electroluminescence (EL) and photoluminescence (PL) spectra of the RCLED shown in Fig. 101. The luminescence of a reference PS is reported as a dashed line. Adapted from Ref. [235].

FIG. 103. Basic scheme of an optical sensor. Due to the difficulty in obtaining transmission filters a reflection design has been realized. Various PS DBR forms the filter wheel. Reprinted with permission after Ref. [242].

FIG. 104. Comparison of the true Ag layer thicknesses to the ones predicted by the PS based sensor. The Ag layer was formed by sputtering and was embedded between two AlN layers (25 nm each). Reprinted with permission after Ref. [242], [2].

FIG. 105. Device geometry of the Si photodiode with a PS multilayer stack in the p^+-type doped top layer of the p/n photodiode. The photocurrent flows through the crystalline Si as indicated. Adapted from Ref. [243].

FIG. 106. External quantum efficiency (full line) of the photodiode of Fig. 105 integrated with a DBR. This is compared with a reference diode without the FP (dotted line). The transmission through the DBR is estimated as 1-R and it is reported as the dashed line. Adapted from Ref. [243].

FIG. 107. Schematic structure and fabrication process of a metal-porous silicon microcavity. Adapted from Ref. [244].

FIG. 108. The narrowed luminescence emission of six metal-porous silicon microcavities (solid curves) compared with the luminescence of a reference PS layer (dashed curve). Adapted from Ref. [244].

TABLE I. Effect of anodization parameters on PS formation. Adapted from Ref. [16]

an increase of ... yields a	porosity	etching rate	critical current
HF concentration	decreases (see text)	decreases	increases
current density	increases	increases	-
anodization time	increases	almost constant	-
temperature	-	-	increases
wafer doping (p-type)	decreases	increases	increases
wafer doping (n-type)	increases	increases	-

TABLE II. Wavenumber positions and attributions of the absorption peaks observed in several PS samples. Adapted from Ref. [30,31].

Peak position (cm^{-1})	Attribution	Peak position (cm^{-1})	Attribution
3610	OH stretching in SiOH	1463	CH_3 asymm. deformation
3452	OH stretching in H_2O	1230	$SiCH_3$ bending
2958	CH stretching in CH_3	1056-1160	SiO stretching
2927	CH stretching in CH_2		in O-SiO and C-SiO
2856	CH stretching in CH	979	SiH bending in SI_2-H-SiH
2248	SiH stretching in O_3-SiH	948	SiH bending in Si_2-H-SiH
2197	SiH stretching in SiO_2-SiH	906	SiH_2 scissor
2136	SiH stretching in Si_2O-SiH	856	SiH_2 wagging
2116	SiH stretching in Si_2H-SiH	827	SiO bending in O-Si-O
2087	SiH stretching in Si_3-SiH	661	SiH wagging
1720	CO	624	SiH bending in Si_3SiH

TABLE III. Degradation mechanism of PS under different analysis techniques. Adapted from Ref. [145].

Excitation	Associated techniques	Degradation observed
Blue-UV photons	PL in air	Photo-oxidation
	Micro-Raman	Thermal annealing
X-rays	XPS	H-desorption
	XEOL	Amorphization
Electron beams	Auger	Hydrocarbon build-up
	CL, TEM	Sintering and SiC formation
Ion beams	Ion milling for TEM	Amorphization
	Ion beam analysis	H-desorption
		C and O adsorption

TABLE IV. PS luminescence bands. Adapted from Ref. [1].

Spectral range	Peak wavelength	Label	PL	EL
UV	~ 350 nm	UV band	Yes	No
blue-green	~ 470 nm	F band	Yes	No
blue-red	400-800 nm	S band	Yes	Yes
near IR	1100-1500 nm	IR band	Yes	No

TABLE V. Some spectral characteristics of the S-band. Adapted from Ref. [145].

Property	Typical values	Comments
peak wavelength	1100-400 nm	at 300K
PL efficiency	≥ 5 %	at 300K and for external quantum efficiency
FWHM	0.3 eV	at 300 K
		(8 meV in porous silicon microcavities)
PL decay times	$\simeq 10$ μs	strongly dependent on wavelengths
		temperature and aging condition
Polarisability ratio	P $\leq$0.2	
fine structure under	phonon replica at	heavily aged PS
resonant excitation	56 and 19 mev	energies typical of Si phonons

TABLE VI. Some spectral characteristics of the F-band. Adapted from Ref. [145].

Property	Typical values	Comments
peak wavelength	480 nm	UV excitation at 300 K
PL efficiency	≥ 0.1 %	UV excitation at 300 K
FWHM	0.4 eV	UV excitation at 300 K
PL decay times	1 ns	independent on wavelength and excitation conditions

TABLE VII. Porosity, P, current density, J, etch rate, and refractive index, n. P is measured by gravimetric techniques and n is given at 600 nm. Adapted from Ref. [2].

| P | J | etch rate | | n |
| | | thick sample | multilayer sample | |
%	mA/cm^2	μm/s	μm/s	
53	25.0	0.021	0.015	2.24
62	49.7	0.035	0.021	1.74
75	82.8	0.055	0.040	1.37

TABLE VIII. Parameters for the various Fabry-Perot filters shown in Fig. 63. λ is the FP wavelength, $\Delta\lambda$ the width of the transmittance peak and T_{max} its value. n_H/n_L is the ratio between the refractive indexes of the low and high porosity layers in the Bragg-reflectors whose number of repetitions is indicated in the last column. Adapted from Ref. [2]

| sample | λ | $\Delta\lambda$ | finesse | T_{max} | n_H/n_L | # repetition |
	(nm)	(nm)				
902	533	13	41	0.20	1.7	8
904	629	16	45	0.37	1.60	8
908	731	16	45	0.56	1.50	6
906	782	18	46	0.55	1.43	6

TABLE IX. Growth parameters and reflectivity data of the various PS microcavities. The name of the sample contains also information about the thickness of the central layer for the first two rows while refers to the porosity of the central layer, which was $\lambda/2$ thick, for the last three rows. The second column reports the sequences of the periodic stacking of high refractive index (H, 62% porosity) and low refractive index (L, 45% porosity) layers, C stands for the central layer. n_H, n_L and n_0 refer to the refractive index values for the high refractive index layer, the low refractive index layer and the central layer, respectively, measured on thick samples at λ (which is given in the next column and refers to the microcavity resonance). $\Delta\lambda$ is the measured FWHM of the microcavity transmission peak which has a maximum transmittance of T_{MAX}. R_{MAX} is the maximum reflectance of the microcavity. The column labeled Stop-Band reports the wavelength width of the high reflectivity region of the reflectance spectrum. The column age reports the age of the microcavities when the measurements have been performed. Adapted from Ref. [2].

Name	slabs order	n_H	n_L	n_c	λ (nm)	$\Delta\lambda$ (nm)	T_{MAX} (abs. un.)	R_{MAX} (abs. un.)	Stop- Band (nm)	age
PSM λ	LH×6+C+HL×6	2.45	1.53	1.28	731	17	$\simeq$0.40	$\simeq$0.95	$\simeq$200	1 year
PSM $\lambda/2$	LH×6+C+HL×6	2.45	1.53	1.28	730	14	$\simeq$0.45	$\simeq$0.95	$\simeq$200	1 year
PSM 75%	HL×6+C+LH×6	2.1	1.63	1.30	692	10	$\simeq$0.40	$\simeq$0.95	$\simeq$130	10 days
PSM 62%	HL×6.5+C+HL×6.5	2.42	1.52	1.52	741	9	$\simeq$0.60	$\simeq$0.95	$\simeq$150	10 days
PSM 45%	HL×6+C+LH×6	2.1	1.63	2.2	692	9	$\simeq$0.60	$\simeq$0.95	$\simeq$150	10 days

TABLE X. Some characteristics of the aged microcavities compared with a porous silicon layer (here named PS) obtained by using the same etching parameters as the microcavity central layer and with a dielectric Bragg reflectors (here named mirror) obtained by using the same etching parameters as the microcavity mirrors. I_{integ} refers to the spectrally integrated luminescence intensity, $I(\lambda_c)$ to the peak emission intensity at the wavelength of the microcavity resonance (λ_c= 730 nm), the τ and β to the parameters obtained from a least-square fitting with a stretched exponential lineshape for the luminescence decay at the wavelength indicated as subscripts (units of nm). Adapted from Ref. [2].

	I_{integ}	$I(\lambda_c)$	τ_{700} (μs)	β_{700}	τ_{730} (μs)	β_{730}	τ_{760} (μs)	β_{760}
PS	0.87	0.14	32.4±0.2	0.80±0.01	37.4±0.6	0.78±0.01	49.0±0.4	0.78±0.01
mirror	0.68	0.07	18.4±0.3	0.61±0.01	20.6±0.3	0.62±0.01	29.4±0.7	0.55±0.01
λ-cavity	0.97	0.97	10.9±0.4	0.54±0.01	30.9±0.7	0.69±0.01	24±1	0.44±0.01
λ/2-cavity	1	1	8.3±0.2	0.66±0.01	19.5±0.6	0.75±0.02	19.9±0.8	0.51±0.01

TABLE XI. Excitation power dependence of the luminescence decay of the λ/2-cavity. $I_0 \simeq$ 500 W/cm^2 is the excitation power intensity, τ and β refers to the parameters extracted from a stretched exponential fit of the luminescence decay at the wavelength indicated as subscripts (units of nm). Adapted from Ref. [2].

	τ_{700} (μs)	β_{700}	τ_{730} (μs)	β_{730}	τ_{760} (μs)	β_{760}
I_0	8.3±0.2	0.66±0.01	19.5±0.6	0.75±0.02	14.1±0.4	0.55±0.01
I_0/3	10.9±0.5	0.60±0.02	14.0±0.9	0.64±0.03	17.6±0.9	0.49±0.02
I_0/7	12±1	0.35±0.02	10±1	0.48±0.03	19±2	0.36±0.02

TABLE XII. Some characteristics of microcavities (here named PSM) with different central layer porosities (indicated as NN %) compared with porous silicon layers (named PS NN %) obtained by using the same etching parameters as the microcavity central layers and with dielectric Bragg reflectors (named mirror) obtained by using the same etching parameters as the microcavity mirrors. All the microcavities had the same etching parameters and the central layer porosity. I_{integ} refers to the spectrally integrated luminescence intensity, $I(\lambda_c)$ to the peak emission intensity at the wavelength of the microcavity resonance (λ_c), the τ and β to the parameters extracted from a stretched exponential fit of the luminescence decay at the wavelength indicated as subscripts (in units of nm or as *cavity* at λ_c). The τ and β at λ_c for the mirror are reported for the different λ_c of the various PSM. After Ref. [222].

	I_{integ}	$I(\lambda_c)$	τ_{cavity} (μs)	β_{cavity}	τ_{650} (μs)	β_{650}	τ_{750} (μs)	β_{750}
PS 45 %	-	-	-	-	-	-	-	-
PS 62 %	0.13	0.03	22±2	0.50±0.03	9.5±0.6	0.67±0.04	25±3	0.73±0.08
PS 75 %	0.26	0.08	20.2±0.5	0.72±0.01	9.6±0.3	0.62±0.01	28±2	0.69±0.03
mirror (45%)	0.84	0.23	7.5±0.3	0.47±0.01	5.2±0.3	0.52±0.02	11.8±0.5	0.48±0.01
(62%)		0.20	9.2±0.4	0.49±0.01				
(75%)		0.24	7.5±0.3	0.47±0.01				
PSM 45 %	1	0.81	9.8±0.1	0.62±0.01	3.4±0.1	0.54±0.01	8.4±0.1	0.43±.0.01
PSM 62 %	0.95	0.66	13.3±0.1	0.62±0.01	2.4±0.4	0.38±0.01	10.7±0.4	0.44±0.01
PSM 75 %	0.92	1	15.2±0.1	0.62±0.01	5.5±0.1	0.40±0.01	8.9±0.1	0.48±0.01

TABLE XIII. Ratio of the peak emission intensity $\frac{I^{PSM}(\lambda_c)}{I^{PS}(\lambda_c)}$ and luminescence decay time $\frac{\tau^{PSM}}{\tau^{PS}}$ of the porous silicon microcavities (PSM) versus the reference PS samples. After Ref. [222].

	n_c	$\frac{I^{PSM}(\lambda_c)}{I^{PS}(\lambda_c)}$	$\frac{\tau^{PSM}}{\tau^{PS}}$
PSM 45 %	2.2	∞	0
PSM 62 %	1.52	22	0.6
PSM 75 %	1.30	12.5	0.75

TABLE XIV. Optical mode extension into the DBR (with a medium refractive index n_{DBR}) and effective refractive index (n_{eff}) for various porous silicon microcavities (PSM). ℓ_p^{air} and ℓ_p^{Si} are the penetration lengths on the air and Silicon side, respectively. After Ref. [222].

	n_{DBR}	ℓ_p^{air} (nm)	ℓ_p^{Si} (nm)	n_{eff}
PSM λ	1.884	200	198	1.528
PSM $\lambda/2$	1.884	200	198	1.632
PSM 45%	1.835	559	459	1.872
PSM 62%	1.867	338	327	1.774
PSM 75%	1.835	511	469	1.721

TABLE XV. Results of the least square fitting of the temperature dependence of the luminescence lifetimes shown in Fig. 89 with Eq. 48. ΔE_x, τ_{trip} and τ_{sing} are the triplet-singlet splitting energy, the triplet lifetime and the singlet lifetime, respectively. After Ref. [222].

sample	ΔE_x	τ_{trip}	τ_{sing}
	(meV)	(ms)	(μs)
PS (at λ_c)	6 ± 0.4	2.6 ± 0.7	17 ± 1
PSM (at λ_c)	7 ± 0.3	5.9 ± 0.6	10 ±1
PSM (at λ= 695 nm)	7±0.6	1 ± 0.2	8±1

TABLE XVI. Thicknesses of the two cavity layers (S_1 and S_2) in units of $L_c = \lambda_c/(2n_c)$ of the various samples studied. The resonance wavelength λ_c in vacuum is 750 nm. λ_1, λ_2, $FWHM_1$ and $FWHM_2$ are the wavelengths and FWHM of the first (lower λ) and second (higher λ) cavity resonance, respectively. A_1/A_2 (L_1/L_2) is the ratio between the integrated (peak) emission intensities of the two resonances. After Ref. [222].

sample	S_1	S_2	λ_1	λ_2	$FWHM_1$	$FWHM_2$	A_1/A_2	L_1/L_2
			(nm)	(nm)	(nm)	(nm)		
c	$L_c + L_c/50$	$L_c - L_c/50$	701.4	729.4	5.2	5.5	0.1	0.11
b	$L_c + L_c/100$	$L_c - L_c/100$	734.6	760.5	8.9	8.1	0.42	0.4
a	L_c	L_c	738.9	764.9	4.7	5.7	0.6	0.71
d	$L_c - L_c/100$	$L_c + L_c/100$	733.9	763.0	6.2	6.8	0.96	1.1
e	$L_c - L_c/50$	$L_c + L_c/50$	757.9	784.7	7.4	11.4	0.97	1.5

TABLE XVII. Potential application areas of PS. Adapted from Ref. [1].

application area	role of PS	key property
optoelectronics	LED	efficient electroluminescence
	waveguide	tunability of refractive index
	field emitter	hot carrier emission
	optical memory	non-linear properties
micro-optics	Fabry-Perot filters	refractive index modulation
	photonic band-gap structures	regular macropore array
	all optical switching	highly non-linear properties
energy conversion	antireflection coatings	low refractive index
	photo-electrochemical cells	photocorrosion cells
environmental monitoring	gas sensing	ambient sensitive properties
microelectronics	micro-capacitor	high specific surface area
	insulator layer	high resistance
	low-k material	electrical properties
wafer technology	buffer layer in heteroepitaxy	variable lattice parameter
	SOI wafers	high etching selectivity
micromachinig	thick sacrificial layer	highly controllable etching parameters
biotechnology	tissue bonding	tunable chemical reactivity
	biosensor	enzyme immobilization

TABLE XVIII. Comparison between some properties of various Si based light emitting systems and of perspective applications. The presented data comes from a survey performed at the EMRS meeting (June 1998). * with PSM it can be as small as 4 meV.

material	starting date	LED efficiency (%)	modulation speed (MHz)	peak emission (μm)	spectral width (meV)	stability
PS	1990	>1	10	0.65-0.8	200*	$\geq$ weeks
SiGe	1974	-	11	1.32	100	good
Er:Si	1983	0.05	1	1.54	16	years
nano Si	1992	0.05	>10	0.4	200	hours
Silicides	1995	0.02	-	1.5	3.5	-
Multilayers	1995	0.01	-	0.5-0.8	200	hours (Si/CaF$_2$)
						weeks (Si/SiO$_2$)
displays		> 1	> 0.001	BGR	100 meV	10^3-10^5 hours
interconnects		>10	>100	any	-	>10^5